# Iron Loss Computation in a Synchronous Machine from a Static Field Solution

Md Masum Billah

**School of Electrical Engineering**

Thesis submitted for examination for the degree of Master of Science in Technology.

Espoo 24.02.2020

**Supervisor**

Prof. Anouar Belahcen

**Advisors**

Floran Martin, D.Sc.

Aswin Balasubramanian, M.Sc.

Aalto University
School of Electrical
Engineering

Aalto University
School of Electrical
Engineering

Aalto University, P.O. BOX 11000, 00076 AALTO
www.aalto.fi
Abstract of the master's thesis

**Author** Md Masum Billah

**Title** Iron Loss Computation in a Synchronous Machine from a Static Field Solution

**Degree programme** Automation and Electrical Engineering

**Major** Electrical Power and Energy Engineering **Code of major** ELEC3024

**Supervisor** Prof. Anouar Belahcen

**Advisors** Floran Martin, D.Sc., Aswin Balasubramanian, M.Sc.

**Date** 24.02.2020 **Number of pages** 85+1 **Language** English

**Abstract**

Owing to the increasing energy demand, a highly efficient synchronous machine can play a crucial role in energy saving by reducing energy consumption. An optimum machine design requires a good estimation of the power losses, particularly the iron loss due to the complexity involved with the accurate loss prediction. The prediction of iron loss in the synchronous machine has drawn massive attraction due to the extensive use in the power stations and other industrial applications. The conventional time-stepping method for iron loss calculation is computationally highly expensive and can be productive as long as the number of computations remains in a respectable range. However, the situation is different when an excessive number of computations are required, such as for machine optimization, which turns this method into unprofitable. The development of fast and computationally efficient static analysis in case of synchronous machine induce a thought of computing the iron loss using this method which can minimize the computation cost and substitute the time consuming traditional loss computation method. Based on this notion, an effective iron loss computation technique was developed from a single static field simulation which is much faster than the conventional time-stepping method and provide a fair accuracy. A two-dimensional Finite Element Method was used, and the model was integrated with the static FEM analysis program in the in-house software FCSMEK. The model was applied to a 12.5 MW salient pole synchronous machine, and the computational accuracy was validated with the conventional time-stepping simulation.

**Keywords** dynamic field solution, finite element method, iron losses, synchronous machine, static field solution

# Preface

This master's thesis has been accomplished in the Department of Automation and Electrical Engineering, Aalto University in between June 2019-February 2020. I would like to express my sincere gratitude to my supervisor Prof. Anouar Belahcen for trusting and giving me this excellent opportunity to conduct the thesis. I would also like to express my sincere appreciation to my first advisor Dr. Floran Martin. I would like to thank them for their valuable advice, patience guidance, encouragement and supervision. Having a busy schedule, Prof. Anouar Belahcen and Dr. Floran Martin continuously guided me every step of this thesis, and without their regular guidance it would be impossible to achieve the main objectives of this thesis.

I would like to thank my second advisor, Mr Aswin Balasubramanian, for his advice and supports. I want to express my sincere gratitude to Mr Osaruyi Osemwinyen, for supporting, guiding and listening to my every word. I want to thank Mr Ravi Sundaria for assisting me by providing the mesh plotting algorithm. I would like to also thanks Avaz Ruzibaev, Alireza Nemat Saberi, Brijesh Upadhaya, Saravignoban Sandirasegaram and other colleagues at Electromechanics group for creating an enjoyable work environment with the productive discussion that helped me a lot to do my thesis. Thanks to all of my friends here in Finland for making my daily life easy with their care and love.

Finally, my deepest love and gratitude to my parents for their endless support, encouragement and motivation throughout my studies.

Espoo, 24.02.2020

Md Masum Billah

# Contents

# Symbols and abbreviations

## Symbols

| | |
|---|---|
| $\boldsymbol{a}$ | nodal values of magnetic vector potential |
| $\boldsymbol{A}$ | magnetic vector potential |
| $A_z$ | magnetic vector potential in $z$-axis |
| $A$ | cross-sectional area |
| $\boldsymbol{B}$ | magnetic flux density |
| $B_x$ | $x$ components of flux density in Cartesian coordinate |
| $B_y$ | $y$ components of flux density in Cartesian coordinate |
| $B_\phi$ | $\phi$ components of flux density in cylindrical coordinate |
| $B_r$ | $r$ components of flux density in cylindrical coordinate |
| $\hat{B}$ | peak value of flux density |
| $C_f$ | skin friction coefficient for cylindrical rotor |
| $C_{ch}$ | hysteresis loss coefficient |
| $C_{ce}$ | eddy current loss coefficient |
| $C_{ex}$ | excess loss coefficient |
| $d$ | thickness |
| $d_{pole}$ | rotor pole depth |
| $D$ | loss difference in percentage |
| $\boldsymbol{D}$ | displacement field |
| $D_{in}$ | inner diameter |
| $\boldsymbol{E}$ | electric field |
| $f$ | supply frequency |
| $f$ | integration function |
| $F$ | bearing load |
| $\boldsymbol{F}$ | source term |
| $\boldsymbol{F}_{pm}$ | source term of permanent magnet |
| $\boldsymbol{H}$ | magnetic field strength |
| $\boldsymbol{i_s}$ | stator current |
| $I_{rms}$ | rms value of supply current |
| $\boldsymbol{J}$ | Jacobian matrix |
| $\boldsymbol{J}$ | total current density |
| $\boldsymbol{J}_M$ | magnetization current density |
| $k$ | number of phases |

| | |
|---|---|
| $k$ | step size |
| $k_r$ | eddy current factor |
| $K_s$ | skin friction coefficient for salient pole rotor |
| $l$ | length |
| $L_{ew}$ | end winding inductance |
| $m$ | number of integration points |
| $n$ | total number of nodes |
| $n$ | number of harmonic orders |
| $n_s$ | synchronous speed |
| $N$ | partition number |
| $N$ | shape functions |
| $\boldsymbol{M}$ | magnetization |
| $p$ | number of pole pairs |
| $P_t$ | total power loss |
| $P_{cu}$ | copper loss |
| $P_{fw}$ | friction and windage losses |
| $P_{stray}$ | stray load loss |
| $P_f$ | friction loss |
| $P_w$ | windage loss |
| $P_{fe}$ | iron loss |
| $P_{hys}$ | hysteresis loss |
| $P_{ed}$ | eddy current loss |
| $P_{ex}$ | excess loss |
| $P_r$ | rotational loss |
| $P$ | number of rotor poles |
| $P_\theta$ | rotor pole pitch |
| $Q_s$ | number of stator slots |
| $r$ | radial distance from rotor midpoint to node |
| $\boldsymbol{r}$ | residual vector |
| $r_{out}$ | outer radius |
| $\boldsymbol{R}$ | rotation matrix |
| $R_{dc}$ | DC resistance |
| $R_{ac}$ | AC resistance |
| $R_s$ | stator resistance |
| $\boldsymbol{S}$ | stiffness matrix |
| $t$ | time variable |
| $t_n$ | sample step size |

| | |
|---|---|
| $\Delta t$ | time interval or step |
| $T$ | temperature |
| $T$ | time period |
| $T_s$ | sampling time period |
| $u$ | local coordinate |
| $\boldsymbol{u_s}$ | stator voltage |
| $v$ | local coordinate |
| $V$ | volume |
| $w$ | weight functions |
| $W$ | number of turns |
| $x$ | $x$ axis in Cartesian coordinate |
| $y$ | $y$ axis in Cartesian coordinate |
| $z$ | $z$ axis in Cartesian or cylindrical coordinate |
| $Z$ | impedance |
| $\alpha$ | temperature coefficient of resistance |
| $\gamma$ | mass density |
| $\Gamma$ | boundary of the solution region |
| $\phi$ | angular coordinate in cylindrical system |
| $\phi_n$ | phase angle between $\boldsymbol{B}$ and $\boldsymbol{H}$ |
| $\mu_f$ | friction coefficient |
| $\mu$ | permeability of material |
| $\mu_o$ | permeability of vacuum |
| $\nu$ | reluctivity of material |
| $\rho$ | resistivity of material |
| $\rho_{20}$ | resistivity at $20^oC$ temperature |
| $\sigma$ | material conductivity |
| $\omega$ | angular frequency |
| $\Omega$ | two dimensional problem domain |
| $\theta$ | angular distance from rotor midpoint to node |
| $\theta_s$ | stator slot pitch |
| $\Psi$ | flux linkage |

## Operators

| | |
|---|---|
| T | superscript indicates the matrix or vector transposition |
| $\nabla.$ | divergence |
| $\nabla$ | gradient |
| $\nabla \times \mathbf{A}$ | curl |

| | |
|---|---|
| $\frac{\mathrm{d}}{\mathrm{d}t}$ | derivative with respect to variable $t$ |
| $\frac{\partial}{\partial t}$ | partial derivative with respect to variable $t$ |
| $\sum_i$ | sum over index $i$ |

## Abbreviations

| | |
|---|---|
| 1D | one-dimensional |
| 2D | two-dimensional |
| 3D | three-dimensional |
| AC | alternating current |
| BSRM | bearing less synchronous reluctance |
| DC | direct current |
| DPM | dynamic Preisach model |
| DHM | dynamic hysteresis model |
| FEM | finite element method |
| FE | finite element |
| FEA | finite element analysis |
| FT | Fourier transformation |
| MMF | magneto-motive force |
| MO | magnetic object |
| PM | permanent magnet |
| PMSM | permanent magnet synchronous machine |
| PDE | partial differential equations |
| RMF | rotating magnetic field |
| RMS | root mean square |
| RPM | revolution per minute |
| SyRM | synchronous reluctance machine |

## FCSMEK routines

| | |
|---|---|
| MESH | a finite element mesh generator program for electrical machines |
| SYDC | a static analysis program for the synchronous machine |
| CIMTD | a time-stepping analysis program for electrical machines |

# 1 Introduction

## 1.1 Background

Over 100 years, the synchronous machine is playing a leading role both as an energy conversion device in the electrical power generation and certain special applications. As the name suggests, a synchronous machine can run with constant speed regardless of the load characteristics. This unique feature of synchronous machine attracts the industry for the many applications where constant speed is required. From several hundred MVA to a few VA, synchronous machines are used in vast power generating stations to a small electric clock. With the increasing global electricity demand and innovating new industrial applications, it can be anticipated that the usage of the synchronous machine is even more popular in the future.

Like other rotating machines, power loss is a common issue in the synchronous machine. The extensive use of synchronous machines both as motor and generator makes the study of losses and efficiency very important. Losses in the electrical machine increase the temperature and degrade the machine performance by affecting the maximum output power. Besides, extreme temperature rising can lead to machine insulation failure, consequently, decrease the machine life expectancy (Rajamäki, 2019). Therefore, power loss and efficiency improvement are essential to reduce power consumption as well as minimize the operating cost. A detailed study of the different losses occurring in synchronous machines and their origin is compulsory to improve efficiency. The losses in the synchronous machine can be categorized broadly as mechanical and electrical losses. During rotation, the machine experiences mechanical losses as friction and windage. Furthermore, the electrical losses can be classified as resistive losses in windings and core losses in the iron core. Iron losses share a significant portion of all other losses in the synchronous machine. However, the reason for mechanical and resistive losses in the machine is well understood, and accurate models are readily available for loss estimation. Moreover, iron or core loss offers a more complex challenge for accurate loss estimation and efficiency improvement. The computation of iron loss components is challenging as the loss components largely depend on the material characteristics and the machine geometry. Iron loss in the machine mainly occurs in the stator yoke, stator teeth, and rotor yoke region. For high-speed machines, the severity of the iron loss components is even more (Krings, 2014).

The computation of iron loss entirely depends on the flux density profile in different sections of the magnetic material. During rotation, the profile of flux density changes in the various places of the magnetic material based on the rotor position. As the rotor position depends on time, therefore, the magnetic flux density is also varying with the time. Thus, the simulation of magnetic flux density distribution is usually done for each time step (Hudak et al., 2004). This time steeping transient analysis of the electrical machine is well known and widely used. However, the computation time is much higher for transient analysis; consequently, iron loss calculation. Therefore, an effective computation technique with less simulation time can substitute transient analysis to save a substantial amount of time.

During steady-state, the rotor of the synchronous machine rotates at the same angular frequency of the rotating magnetic field (RMF) in the air gap. As a result, all the fields in the synchronous machine can be considered as static fields in the rotor reference frame. This assumption offers a new scope of the field computation from a static solution. Furthermore, static calculation shortens the simulation time, which attracts the machine designer for the design and analysis of synchronous machines (Belahcen et al., 2016). The main objective of this thesis is to compute iron loss from a static field solution by taking the rotational aspect of magnetic flux density into account, which reduces the computation time without losing the accuracy.

## 1.2 Thesis Objectives

The principal objective of this thesis is to develop an iron loss computation technique from a static field solution. To achieve the primary goal, the following tasks are performed in a step by step. At first, a literature review is done about the design, construction, and operating principle of various synchronous machines, losses in electrical machines, iron loss models, and selecting a suitable loss model for the computation. Secondly, the 2D Finite Element Method (FEM), and the static field computation methodology using FEM was studied briefly. Thirdly, a 2D static field solution of the synchronous machine is extracted using the in-house FE software FCSMEK. Then, an algorithm is developed to compute the iron loss from the obtained static field solution. Finally, the iron loss is calculated from the dynamic field solution and compared with the iron loss computed from the static field solution for validation purpose.

## 1.3 Thesis Structure

The thesis is divided into five chapters. Chapter 1 deals with initializing the thesis scope by explaining the background and motivation of the thesis. Besides, the key objectives of this thesis are stated, and the structure of the thesis is described in this chapter. Chapter 2 presents the literature review of the theoretical background of synchronous machines, origin, structure, and computation of different losses in electrical machines, and the history, modelling, and various techniques of iron loss computation. Chapter 3 introduces the theoretical background of the FEM, the methodology of obtaining static field solution, the computation technique of iron loss from a static field solution, and the iron loss computation procedure by using time-stepping simulation. Chapter 4 contains the application of the developed loss model in a salient pole synchronous machine, the simulation results, and findings of the developed model are explained briefly. Moreover, a detailed comparison between simulation results using static field solution and dynamic field solution is carried out here. Chapter 5 highlights the concluding remarks of the conducted research work and the indication of future research perspectives related to this thesis.

# 2 Literature Review

Developing an iron loss calculation method in a synchronous machine requires a brief knowledge about the machine, different losses associated with the synchronous machine and an insightful view about the iron loss models. Section 2.1 discusses the design, structure and operating principle of the various synchronous machines. Section 2.2 deals with the origin, and construction of the different losses exists in the synchronous machine. The attention is mainly given to the iron loss, its components, and their independent loss model. Section 2.3 presents a holistic review of the iron loss models and the selection of a suitable model for iron loss computation.

## 2.1 Introduction to Synchronous Machine

The actual invention of the synchronous machine begun in the 1880s, but F.A. Haselwander (1887) is recognized for developing the current revolving function and built the first-ever three-phase synchronous generator (Neidhofer, 1992). His designed machine had a three-phase ring-shaped stationary armature coil and four salient poles with rotating internal pole magnet for producing the revolving magnetic field, which was the prototype of today's salient pole synchronous machine (Neidhofer, 1992). Even though few developments of the synchronous machines was done during that time, but they were not sufficient for catching the researcher's thought. However, an actual breakthrough occurred and drew worldwide attention when the synchronous machine was used in a hydroelectric power plant to transmit three-phase alternating current in 1891 (Brown, 1891). After that, a considerable effort was invested in the development of synchronous machines. Charles E. Brown (1901) invented first the cylindrical turbo rotor with a solid-iron body, which became the leading design for today's turbo generator and the high-speed synchronous machine (Neidhofer, 1992). By the end of the 19th century, the two basic construction of synchronous machines, i.e., salient pole and cylindrical rotor were in presence, and nowadays, the research works are mainly carried out on the development, optimization, and improvement of specific design and components (Neidhofer, 1992). It can be noticeable that without extensive research and development of direct energy conversion devices, the synchronous machine can be treated as a primary energy conversion device in the next century as well.

Like an induction machine, the stator of the synchronous machine contains a distributed three phases AC windings. However, the rotor construction is different as it can consist of a DC winding supplied with the direct current or a permanent magnet. It creates a significant difference with the asynchronous machine as the resultant current linkage component generated from the rotor field winding or a permanent magnet can work independently in steady-state conditions (Pyrhonen et al., 2013). On the other hand, in the asynchronous machine, the rotor current is induced by the changing or rotating stator magnetic field; consequently, slip occurs (Pyrhonen et al., 2013). As the stator and rotor are excited separately; therefore, the synchronous machine is often called a doubly excited machine. Thus, the flux produced in the air gap is the resultant flux generated by the stator and rotor current

separately. The flux in air gap changes due to the reaction of armature flux and the main pole flux, which affects the power factor of the synchronous machine. The compensation of armature reaction can not be possible automatically; rather, the field current needs to be adjusted for the compensation (Pyrhonen et al., 2013).

In steady-state, the revolving magnetic field produced by the stator windings and the field generated by the DC excited winding or a permanent magnet is locked in the air gap, which causes the rotor to synchronize with the stator rotating field. After synchronization, the rotor of the synchronous machine runs precisely at the same speed of the revolving magnetic field produced by the stator regardless of load variations as long as the supply frequency remains stable and the mechanical stability limit is not exceeded. The speed of the synchronous machine is directly proportional to the supply frequency and inversely proportional to the number of rotor poles. Thus, the speed of a synchronous machine can be determined as

$$n_s = \frac{60f}{p} \tag{1}$$

where $n_s$ stands for the synchronous speed of the machine, $f$ represents the supply frequency, and $p$ is the number of pole pairs. However, the major drawback of a synchronous machine is if the load torque becomes too high, the machine can be run out of synchronism and stalled. The fixed speed limitation of the synchronous machine caused by the supply frequency can be overcome through a synchronous machine speed control scheme. In this scheme, a variable frequency converter is used to provide a variety of synchronous speed profile (Hughes, 2006).

### 2.1.1 Separately Excited Synchronous Machine

In the case of separately excited synchronous machines, the excitation is provided from the external DC source through a pair of slip rings on the shaft. The structure of the rotor can be a salient pole or a non-salient pole, i.e., a cylindrical rotor, as shown in Figure 1. Because of the cylindrical rotor shape, the air gap remains uniform; therefore, the cylindrical rotor has distributed winding. On the other hand, the salient pole synchronous machine has concentrated winding with a non-uniform air gap. The cylindrical rotor is suitable for high-speed machine design such as turbo generator, i.e., 1500-3000 rpm; in contrast, the salient pole rotor is used for low-speed machine design, i.e., few hundreds rpm. When the rotor field current remains zero, the cylindrical rotor has little or no reluctance torque; therefore, the field current is essential to produce the torque for a cylindrical rotor. However, the salient pole rotor produces some reluctance torque even when the rotor field current remains zero. At no load, the torque required to overcome the friction is small enough; thus, the angular displacement between the field produced by the rotor winding and the rotating field of the stator winding is little or non-existent. As the load increases gradually, the rotor slows down immediately creates an angular displacement, i.e., load angle between the flux patterns before restoring to original speed, which is sufficient to produce the torque required for steady-state running. However, when the load changes frequently, the rotor starts to oscillate around its position due to the

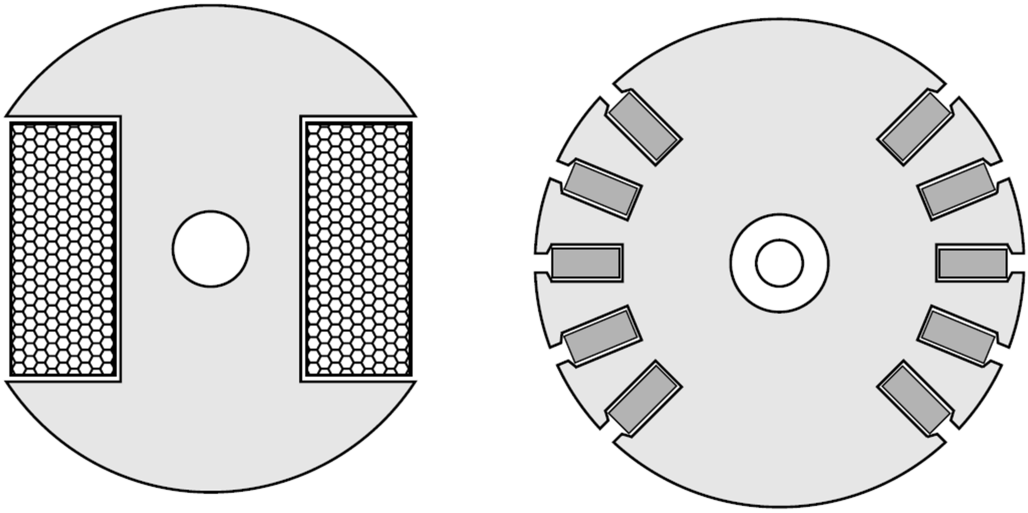

(a) (b)

Figure 1: Rotor construction of a separately excited synchronous machine: (a) Salient pole rotor; (b) Cylindrical rotor (Hughes, 2006).

high inertia before settling back to its original position, this phenomenon is known as hunting. The damping windings are often used in the rotor to prevent the hunting caused by the sudden load change. The separately excited synchronous machines are not a self-starting machine; thus, the machine can be run with a variable frequency supplier or started as an induction machine (Sen, 2007). In the transient state, the synchronous machine with damper windings acts in a very similar way as squirrel cage asynchronous machine does under slip (Pyrhonen et al., 2013). Thus, the damper winding is used to start the separately excited synchronous machine like an induction machine.

A separately excited synchronous machine can draw leading or lagging reactive current from the AC supply. With the exact excitation current provided by the rotor field winding, the machine does not draw any reactive current from the supply and operates at unity power factor. However, the situation changes when the rotor excitation current surplus the requirements, and the machine can draw leading reactive current from the AC supply to oppose the over magnetization caused by the excess rotor excitation current and operates at leading power factor. Moreover, the synchronous machine can also draw the lagging reactive current from the supply to compensate the magnetization caused by the less rotor excitation current and operates at lagging power factor. Thus, the power factor of the system can be controlled by changing the rotor field current in the synchronous machine (Sen, 2007). However, this unique feature is unavailable in permanent magnet assisted synchronous machine (PMSM) as the field produced by the permanent magnet (PM) remains fixed.

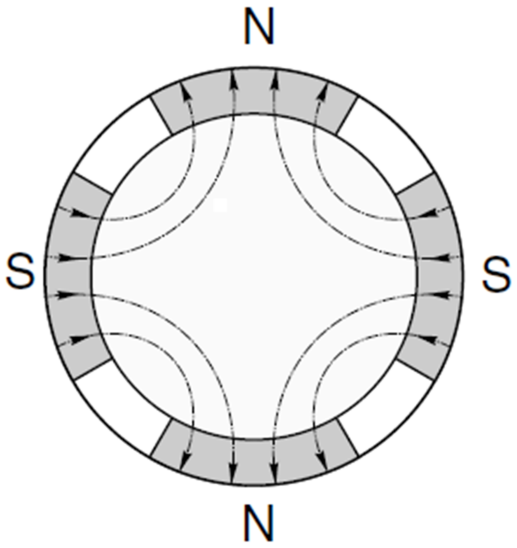


Figure 2: Rotor construction of a 4 poles radial flux PMSM (Hughes, 2006).

### 2.1.2 Permanent Magnet Synchronous Machine (PMSM)

Instead of having a field winding, the permanent magnet is used on the rotor to produce the necessary magnetic field required for the magnetization. The rotor construction of a PMSM is shown in Figure 2. Having a permanent magnet discarded the necessity of excitation current on the rotor as the magnetic field is produced naturally; thus, the more robust and reliable rotor construction can be possible. Moreover, the relatively low magnetizing inductance offered by the low permeability magnetic material significantly reduces the armature reaction compared to the separately excited synchronous machine (Pyrhonen et al., 2013). However, as the magnetic field generated by the permanent magnet remains constant, the rotor magnetic field can not be controlled according to the load variations. The requirements for a specific load can be fulfilled by choosing the shape and the position of the magnet. At full load, the efficiency and power factor of PMSM is better than the equivalent induction machine in steady-state condition (Hughes, 2006). Like a separately excited synchronous machine, PMSM is also not a self-starting machine. Due to the unavailability of damper windings, the PMSM can not start as an induction motor. Therefore, the permanent magnet synchronous machine can be started with a variable frequency supply.

### 2.1.3 Synchronous Reluctance Machine (SyRM)

The stator construction of the synchronous reluctance machine can be identified as a three-phase induction machine, and the rotor has a set of laminations shape tends to incline with the field produced by the stator winding. Unlike induction or

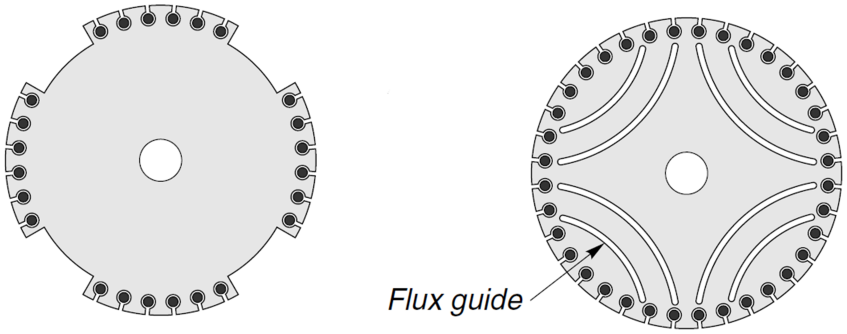


(a) (b)

Figure 3: Rotor construction of a synchronous reluctance machine: (a) Salient pole type; (b) Flux guided shape (Hughes, 2006).

other synchronous machines where the reaction torque is required, the operation of the reluctance machine entirely relies on the reluctance torque (Matsuo & Lipo, 1994). The alignment of stator and rotor saliency establishes the minimum reluctance path, and the rotor tendency to line up in minimum reluctance position produces the necessary torque. The flux can be inserted into the rotor based on the rotor construction. For instance, some periphery of the salient type rotor as depicted in Figure 3(a) cutaway to create a large air gap, i.e., high reluctance path, and force the flux to insert into the rotor through the remaining region where the reluctance becomes minimum. Alternately, the flux can be guided according to the specified path by removing some inside parts of the rotor as illustrated in Figure 3(b), and allow the flux to follow the desired path. The tendency of the rotor to align with the field by itself keeps the rotor in synchronism with the rotating filed established by the three-phase stator winding (Hughes, 2006). The recent growing interest makes the synchronous reluctance machine well attractive, and also showed that this machine could contest with an equivalent induction machine almost equally in many aspects such as efficiency, and output power (Hughes, 2006).

### 2.1.4 Hysteresis Synchronous Machine

While the hysteresis loss is considered as an unwanted phenomenon in the electrical machines, there is one particular motor so-called hysteresis motor where the hysteresis loss accounted for producing the required torque. The construction of a hysteresis motor is quite different from other motors, and without previous familiarity, one can be easily puzzled after dismantling it. The stator construction is similar to other synchronous machines that have single or three-phase winding, but the significant difference is noticeable in rotor construction as it merely contains a thin-walled cylinder as shown in Figure 4. The machine operation ultimately depends on the rotor sleeve properties, which is responsible for producing the magnetic hysteresis.

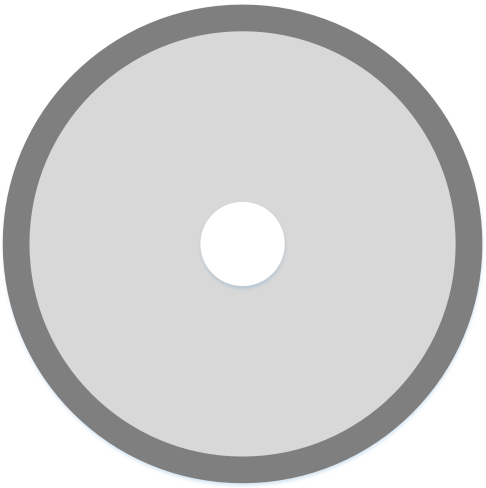

Figure 4: Rotor construction of a hysteresis synchronous machine.

Despite having the slip frequency, the tendency of the rotor to achieve the synchronous frequency settles exactly in the synchronous speed. The torque developed in the rotor is proportional to the hysteresis loop area (Soroush et al., 2009). Small torque ripple during steady-state suits the hysteresis motor for some specific applications where smooth torque is desirable over a wide range of frequencies. Like other synchronous machines, hunting around field frequency is a common issue in hysteresis motor. The hysteresis machine having a wider hysteresis loop area has a lower hunting effect compared to a machine that has a narrow loop area (Soroush et al., 2009). The hysteresis machine has not been studied much more probably because of the complex modelling of the hysteresis phenomena compared to the other synchronous machines.

## 2.2 Losses in Synchronous Machine

The highly efficient electrical machine can play a crucial role in energy saving by reducing energy consumption. The machine efficiency can be easily determined by calculating or measuring the total losses according to the standard procedure. The most convenient way of defining the losses of an electrical machine is classifying by the loss components based on their origin or structure. Like other electrical machines, the synchronous machine has similar types of losses. Either operating as a motor or a generator, the losses in the synchronous machine can be classified as illustrated in Figure 5.

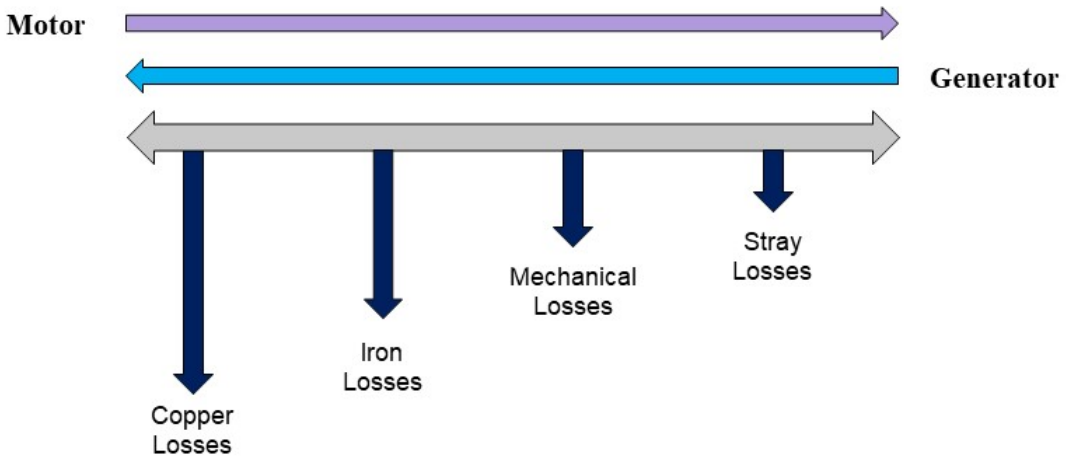


Figure 5: Losses in synchronous machine.

Thus, the total losses can be expressed as a sum of these individual loss components

$$P_t = P_{cu} + P_{fe} + P_{fw} + P_{stray} \tag{2}$$

where $P_t$ denotes the total losses, $P_{cu}$ is the copper or resistive losses, $P_{fe}$ is the iron losses, $P_{fw}$ is the friction and windage losses, and $P_{stray}$ is the stray losses. The percentage of loss components depends on the machine size and the speed profile. Usually, the resistive or copper losses caused in machine winding dominates the other loss components for relatively large size and slow speed machine. However, the situation changes for the high-speed machines where the major loss components become the mechanical losses due to friction and iron losses due to the rapid changing of magnetic fields (Krings, 2014). Rajamäki (2019) presented the percentage of loss components in a synchronous generator where the resistive losses caused in stator and rotor windings contributes a significant portion (50-60%) and iron loss occurred in the stator core, and rotor pole faces shares 20% of the total losses. Soualmi et al. (2012) studied the loss components focusing on resistive and PM eddy current loss in PMS machine at no load and full load condition with and without conductor segmentation effect. Even though the conductor segmentation reduced the resistive losses at both no load and full load conditions, the resistive losses still dominate the other loss components, and the contribution of iron loss varies from (20%-32%) based on different conditions. The mechanical losses caused by windage of moving

rotor and friction in the bearing of the machine also share a significant portion of total losses, but these losses can be often considered as constant losses for different operating conditions of the machine (Karmaker, 1992). The magnetic leakage and fringing flux of the rotating machines cause stray losses that contribute small losses. The iron losses are non-negligible contributors for any synchronous machine, and the primary goal of this thesis is iron loss computation. Thus, the iron losses are studied in extensive detail, whereas the other loss components are described shortly in the following section.

### 2.2.1 Resistive Losses

The resistive losses (also referred to as copper losses, ohmic losses, winding losses, etc.) are caused by the current flowing through the machine winding. The resistive losses can be found in the stator winding, rotor winding, and rotor bar. The resistive losses occur in the stator winding due to the supply current. The DC current is responsible for resistive losses in rotor winding, which is needed for magnetizing the rotor poles. Moreover, the pulsating flux in the air gap induces the current that causes the resistive losses in the rotor bar (Rajamäki, 2019). The resistive losses are often estimated based on the DC equivalent resistance value of the winding as follows

$$P_{cu} = kI_{rms}^2 R_{dc} \tag{3}$$

where $I$ is the RMS value of the winding current, $R$ is the equivalent DC resistance of one phase winding, and $k$ is the number of phases. The DC resistance of each phase winding can be determined as

$$R_{dc} = \frac{\rho l W}{A} \tag{4}$$

where $l$ is the length of the one turn of the phase coil, $A$ is the cross-sectional area of the conductor, $\rho$ is the resistivity of material, and $W$ is the number of turns of the phase coil. The resistivity of material significantly depends on the temperature; thus, rising temperature leads to an increase in the resistivity value. In general, copper wires are used in the winding of commercially available machines. The resistivity of copper changes with the temperature and can be estimated to any given temperature as

$$\rho = \rho_{20}[1 + \alpha(T - 20^oC)] \tag{5}$$

where $\rho_{20}$ is the resistivity at $20^oC$, $T$ is the temperature, and $\alpha$ is the temperature coefficients of the resistance. However, the alternating current generates additional resistive losses in the machine winding. The time-varying current leads to a time varying magnetic field, hence, induce an eddy current in the windings and other conductive areas. The induced eddy current causes two unwanted phenomena in the conductor of the machine winding. At first, The skin effect is generated inside the conductor by the induced eddy current, which forces the primary current to flow through the conductor skin. Secondly, the proximity effect caused by the longitudinal eddy current induced from the neighbouring conductor reinforces the primary current

to flow through the smaller area of the conductor (Islam, 2010). The ultimate result of these two phenomena is the uneven distribution of the current through the conductors, which increases the effective resistance of the conductor (Sadarangani, 2006). As a result, the actual resistive losses are higher than the losses calculated by using the DC resistance. The more accurate estimation of resistive losses can be achieved by using the AC resistance of the phase winding instead of DC resistance. Like DC resistance, the AC resistance is calculated in a similar way; however, a correction factor is introduced in the equation to evaluate the resistive losses more accurately (Pyrhonen et al., 2013).

$$R_{ac} = k_r \frac{\rho l W}{A} \tag{6}$$

where $k_r$ denotes the eddy current factor.

### 2.2.2 Mechanical Losses

In a rotating machine, a significant portion of the mechanical losses appears from the friction and windage loss. The friction loss mainly occurs in the machine's bearing, which depends on the bearing types, and the lubricants used in the machine. Moreover, the speed of the machine shaft and the amount of load on the machine bearings largely influences the friction loss (Pyrhonen et al., 2013). Usually, the manufacturers provide the necessary instructions to calculate the friction loss of the bearings. One of the bearing manufacturer (SKF, 1994) proposed a model to estimate the friction loss in the normal operating conditions

$$P_f = 0.5\omega\mu_f F D_{in} \tag{7}$$

where $\omega$ stands for the angular frequency of the shaft, $\mu_f$ is the friction coefficient, $F$ is the load on the bearing, and $D_{in}$ is the inner diameter of the bearing.
The windage loss mainly occurs in the machine air gap due to the friction between the surface of the rotor and the surrounding gas, e.g., air. The severity of windage loss becomes more for the high-speed machine. The shape of the rotor surface substantially influences the windage loss and becomes more severe for a rough rotor surface. Vrancik (1968) experimentally developed a model and investigated the windage loss of the machine

$$P_w = \pi C_f \gamma r_{out}^4 \omega^3 l \tag{8}$$

where $\gamma$ is the mass density of the gas or liquid, $C_f$ is the skin friction coefficient, $r_{rotor}$ is the outer rotor radius, $l$ is the cylinder length, and $\omega$ is the angular frequency. The proposed model had relatively good accuracy for the smooth cylindrical rotor but provided inaccurate results for the salient pole machine, i.e., round and rough rotor surface (Krings, 2014). Later, the initial model was simplified by (Vrancik, 1968) for the non-smooth salient pole machine with a new correction factor $K_s$, which provided a relatively good result.

$$K_s = 8.5\left(\frac{d_{pole}}{r_{out}}\right) + 2.2 \tag{9}$$

where $K_s$ is the skin friction coefficient for salient pole rotor, and $d_{pole}$ is the rotor pole depth. Saari (1998) divided the windage loss into two parts and presented two equations for calculating the windage loss in the machine. The windage loss occurs due to obstructing the drag torque of the rotor, and the windage loss caused by the rotor end surfaces are modelled separately. The total windage loss is computed as a summation of these two loss contributors.

Aside from friction and windage losses, the shaft-mounted fan used for ventilation purposes often mounted on the non-drive parts of the machine or driven by another motor increases the mechanical losses significantly (Pyrhonen et al., 2013). Schuisky (1960) proposed an experimental based model for ventilation loss together with the windage loss; however, the model is only valid for standard speed machines (Pyrhonen et al., 2013).

### 2.2.3 Stray Losses

Stray load losses, also known as abnormal losses, are often categorized as additional electromagnetic losses which can not be identified by the resistive, and the iron loss model. The fringing or leakage fluxes and the associated harmonics mainly contribute to stray losses in the synchronous machine. In rotating electrical machines, flux is needed to pass through the air gap to connect the stator and rotor electromagnetically. However, all the flux produced in the machine does not pass through the air gap for taking part in the energy conservation process and considered as leakage flux. Pyrhonen et al. (2013) classified that the leakage flux components occurs in different parts of a machine such as the slot winding, tooth tip, end winding, and rotor pole.

Moreover, the flux crossing through the air gap is subjected to the time and spatial harmonics, and only the fundamental flux component participates in the energy conversion. The time harmonics are introduced in the machine due to the non-sinusoidal time variations of the supply. On the other hand, the non-sinusoidal distribution of the winding, and the slotted nature of the machine leads to the spatial harmonic components. Besides, the uneven number of slots per pole causes the spatial harmonics that can generate the asymmetrical magneto-motive force (MMF), hence, increase the stray loss (Gray, 1926).

The identification and calculation of stray load losses are quite tricky as the model of these fluxes is challenging, and often requires 3D analysis (Karmaker, 1992). Brainard (1913) experimentally studied the causes of stray load losses in the synchronous machine and categorized them as the induced eddy current or the uneven distribution of the current in the armature conductors. In addition, the fluxes entering from the stator winding to other non-magnetic parts, e.g., end shields, and coil supports etc. cause eddy current and hysteresis loss. Moreover, the flux distribution changes in the iron core, which adds extra eddy current and hysteresis loss. Furthermore, the leakage flux occurs due to over excitation current under load condition in turbo-generator. Richardson (1945) carried out a qualitative investigation of stray load losses that occur in the end windings, stator core, and the rotor pole surfaces in the synchronous machine. Another qualitative study of stray load losses in the armature end region has been conducted by (Winchester, 1955).

Aston and Rao (1941) studied the stray load losses that occur in rotor pole faces experienced due to the local variation of flux density produced by the slotted nature of the synchronous machine. Aston and Rao (1941) also investigated the stray losses that occur due to the flux variation in the magnetic core by the reluctance pulsations. However, the stray losses arise in different parts of a synchronous machine. An extensive investigation of identifying the stray load loss sources and locations over the different parts of a synchronous machine has been done by (Karmaker, 1992).

Karmaker (1992) presented the stray load losses as a combination of individual magnetic losses occurring in various areas of a synchronous machine; for instance, the slot fringing flux originates a loss in the stator winding. Moreover, the axial fringing flux generated by the air ducts causes losses in the stator core, i.e., yoke and teeth. Besides that, losses occur in the rotor pole faces, damper windings, and end winding region. Also, the leakage flux causes a loss in the structural parts of a synchronous machine such as frame, fingers, etc. Furthermore, the losses are produced from the constructional sources such as core segment joints, and rotor eccentricity etc. The air gap flux harmonics are mainly responsible for the additional losses in the rotor pole faces and the damper windings. Moreover, the stray load losses occur in the end winding of the machine due to the leakage flux occurring from the current flowing through the end winding and can be estimated by computing the end winding leakage inductance (Pyrhonen et al., 2013).

### 2.2.4 Iron or Core Losses

Before discussing the iron loss computation method, a basic understanding of the properties of magnetic materials, and the origin of the iron loss in electrical machines are essential; thus, this section is dealing with the background, structure, and models of iron loss in electrical machines. The stator and rotor core of an electrical machine is made with the ferromagnetic materials; therefore, the most iron loss is experienced by these sectors. The iron loss can be divided into three components, such as hysteresis loss, eddy current loss, and excess loss. Therefore, the total iron loss can be computed as a sum of these three loss components as follows

$$P_{fe} = P_{hys} + P_{ed} + P_{ex} \tag{10}$$

where $P_{fe}$ denotes the total iron loss, $P_{hys}$ is the hysteresis loss, $P_{ed}$ is the eddy current loss and $P_{ex}$ is the excess loss. During changing the magnetic orientation, the magnetic domains consume power, which causes hysteresis loss. The classical eddy current loss occurs when the time-varying magnetic field induces a current in the iron sheet. The local microscopic eddy currents near the moving domain walls are responsible for causing excess loss (Boon & Robey, 1968; Rajamäki, 2019).

In the synchronous machine, the primary contribution of iron loss occurred by the stator core as the rotor, and the air gap field rotates with the synchronous speed. In reality, any presence of harmonic fields that may rotate without synchronism can produce the iron loss in the rotor parts, e.g., magnet, rotor core, and pole faces, etc. Thus, a negligible amount of iron loss compared to the stator core produced in the rotor parts of a synchronous machine. The severity of rotor iron loss becomes

more for the high-speed machine. However, the static analysis refers to the study of the synchronous machine based on the DC field solution; therefore, the flux density induced in rotor parts, mainly DC in nature. As a result, the complete iron loss is contributed by the stator core in the static analysis of a synchronous machine. Therefore, the entire focus of this thesis is to compute the iron loss produced in the stator core.

In this thesis, the iron loss is computed from the Fourier decomposition of flux density waveforms using the Jordan extension model in the post-processing stage. The separate models for three iron loss components are described briefly in this section to understand the loss phenomena comprehensively.

**Hysteresis Losses**

Magnetic materials usually consist of many grains with specific orientations. Each grain is big enough to hold several magnetic domains in which the magnetization is in a uniform direction. Under Curie temperature, the magnetization of the ferromagnetic material is spontaneously split into several small regions, and each region recognized as a magnetic domain, which is depicted in Figure 6. The domains are separated from one another by a specific boundary, and this boundary is called domain walls or Bloch walls. The magnetic moments of each atom inside a domain are uniformly distributed and aligned with one another in a particular direction based on their coupling forces. The magnetic domain structure is responsible for the magnetic behaviour of a ferromagnetic material.

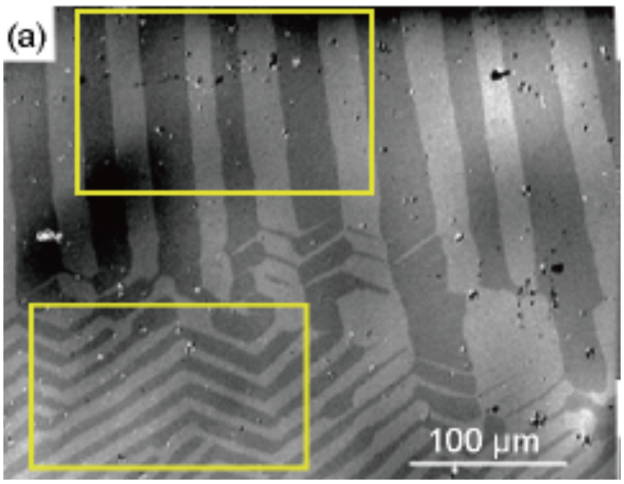


Figure 6: Magnetic domain structure of the FeSi alloy (Chen et al., 2017).

The magnetization process of a ferromagnetic material follows two key steps. One is domain wall motion in which the boundary between two magnetic domains moves, and the magnetization changes are localized in the domain boundary. Another one is magnetic domains can coherently rotate to the direction parallel to the external magnetic field. The size and direction of magnetic domains depend on the direction

of the applied field. When a magnetic field is applied, these two phenomena inside a ferromagnetic material occur simultaneously (Hubert & Schäfer, 2008; D. Jiles, 2015). However, the magnetization of each domain occurs in different directions in a non-magnetized sheet due to the unavailability of the external field; thus, the statistical sum of magnetic domain moments is zero (Krings, 2014). During the iron alloy manufacturing process, the addition of other non-magnetic materials to iron material introduces the imperfection in the form of impurity or dislocations elements. When the magnetic material contains impurities or defects around the domain walls, the movement of the domain wall is not continuous any more, and it does not follow the steadily increase of the applied field directions. Therefore, the movement of the domain wall is stopped where the impurities or imperfections occur and do not jump until the externally applied field becomes high enough. Thus, the magnetization changes inside a magnetic material are not a continuous process any more rather than the discrete process in time. As a consequence, the magnetic flux density also changes discontinuously even though the magnetic field strength changes continuously. Moreover, the direction of magnetization rotates discontinuously inside a magnetic domain, which is familiar as domain rotation (D. Jiles, 2015). These two mechanism leads to a phenomenon known as the Barkhausen effect, which is one of the main reasons of hysteresis loss in the magnetic material. The Barkhausen effect in the initial magnetization curve is illustrated in Figure 7. It is worth noticing that the impact of discontinuous domain wall motion contributes more in Barkhausen effect compare to the domain rotation. Besides the Barkhausen effect, another magnetic mechanism so-called magnetic anisotropy where the magnetic material has different properties in different directions is also responsible for increasing the hysteresis loss.

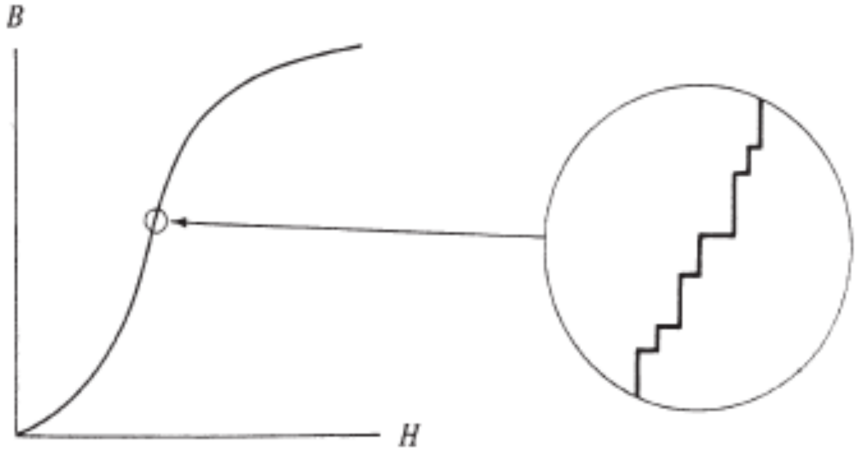


Figure 7: Barkhausen effect in the initial magnetization curve (D. Jiles, 2015).

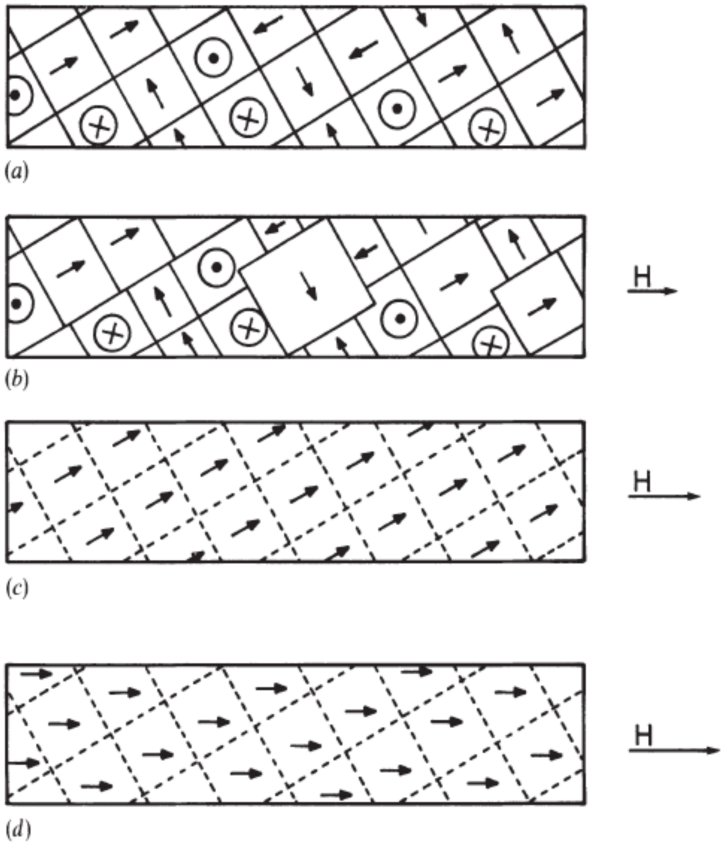


Figure 8: Domain process during the initial magnetization curve formation: (a) Demagnetization stage ; (b) Magnetization stage at low applied field ; (c) Magnetization stage at intermediate applied field ; (b) Magnetization stage at high applied field (D. Jiles, 2015).

Consider a ferromagnetic material that is fully demagnetized as shown in Figure 8(a), the magnetic domain has random directions, but the magnetic moments inside the domain have the same order even in the demagnetized state according to the domain theory (D. Jiles, 2015). The initial magnetization curve is formed when a magnetic field is applied to a demagnetized material. When a low external field is applied as illustrated in Figure 8(b), the domains having direction in favour of the applied field direction start to grow, as a consequence a reduction occurred to the size of the unfavourable domain position, which lines up in the opposite direction of the applied field. When the applied field goes to the intermediate stage as depicted in Figure 8(c), the domain rotation mechanism takes place. In this stage, the magnetic moment inside a domain which is not appropriately aligned to the direction of the applied field overcome the anisotropy energy and start to rotate from their magnetization position into one of the crystallographic easy axes close to the applied field direction (D. Jiles, 2015). If the applied field is increased further, the domains start to rotate coherently, as shown in Figure 8(d). Therefore, the magnetic moment of those domains who have slight angle variation in the previous stage starts

to follow the applied field direction gradually.

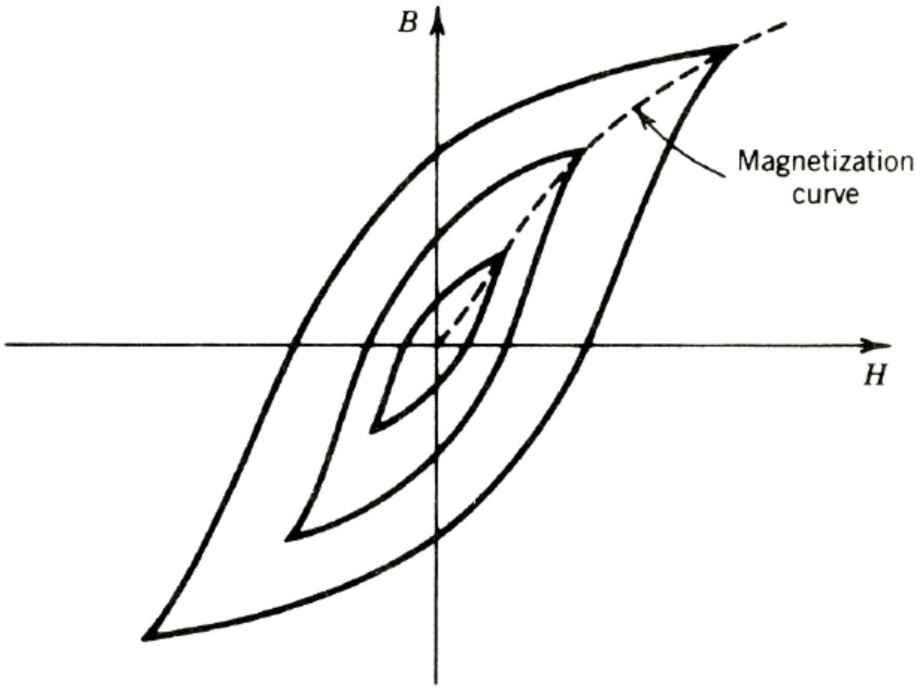


Figure 9: Hysteresis loop formation (Sen, 2007).

The term hysteresis mainly indicates the relationship between the magnetic flux density $\boldsymbol{B}$ and the magnetic field strength $\boldsymbol{H}$ characteristics in magnetic materials. Cycling between positive and negative applied external field directions forms a hysteresis loop as shown in Figure 9, in which the flux density $\boldsymbol{B}$ takes different values depending on increasing or decreasing the magnetic field strength $\boldsymbol{H}$ values. The energy absorbed by a magnetic material is not returned back to the system. In magnetic material, the relationship for the magnetic flux density $\boldsymbol{B}$ in terms of the field strength $\boldsymbol{H}$ and the magnetization $\mathbf{M}$ can be expressed as

$$\boldsymbol{B} = \mu_o(\boldsymbol{H} + \boldsymbol{M}) \tag{11}$$

where $\mu_o$ denotes the permeability of the vacuum. Increasing the magnetic field strength $\boldsymbol{H}$ leads to increase the magnetization $\boldsymbol{M}$ of the material, but after a certain point, the magnetization $\boldsymbol{M}$ remains constant even if the field strength $\boldsymbol{H}$ rises further. However, the flux density $\boldsymbol{B}$ continue to increase with the field strength $\boldsymbol{H}$ where the rate of change of flux density$\boldsymbol{B}$ with respect to $\boldsymbol{H}$ is the unity and known as saturation region. To reverse back the flux density $\boldsymbol{B}$ from the saturation level, the applied field $\boldsymbol{H}$ needs to decrease until the next saturation level of flux density $\boldsymbol{B}$. In an ideal case, when the applied field reaches zero, the flux density $\boldsymbol{B}$ should also be zero. In reality, when the field strength $\boldsymbol{H}$ is zero, there is still some flux density $\boldsymbol{B}$ presents in the material, which is known as residual magnetism. As a result, the flux density $\boldsymbol{B}$ does not reverse back in the same path rather than it

follows another way and forms a loop, which is known as the hysteresis loop. The power trapped in the core of the material is lost in the form of heat. The area of the hysteresis loop determines the amount of losses, and for a larger loop area indicates the more hysteresis loss.

Introducing the term hysteresis as a scalar is a common practice as it is the most studied branch among other hysteresis branches because of the simple and coherent structure. The static hysteresis model only relies on the alternating variation of the flux density and does not take the rotational aspects into account. Preisach (1935) introduced a static hysteresis model based on the physical aspects of the magnetization and recognized as the physical hysteresis model. However, the physical meaning of the Preisach model needs to be well understood; thus, the physical explanation of the Preisach model transformed into purely mathematical form by Krasnosel'skii and Pokrovskii (2012) that gives a numerical method to describe the hysteresis phenomena of any systems (Mayergoyz, 1986). Everett (1955) independently and extensively studied the hysteresis effect and introduced a function that is directly related to the Preisach distribution function. Mayergoyz (1986) extended the classical Preisach model with the Everett function, which eliminates the necessity of double integration. The traditional hysteresis model is not suitable where the field strength $\boldsymbol{H}$ calculated from the flux density $\boldsymbol{B}$ because of the high computation time required for iteration and the large memory needed for storing the data. Takahashi et al. (1999) developed a computationally efficient method to compute field strength $\boldsymbol{H}$ directly from the flux density $\boldsymbol{B}$ without iteration by inverting the distribution function.

Another most widely used static hysteresis model based on differential equations was developed by (D. Jiles & Atherton, 1983; D. C. Jiles & Atherton, 1984). The model setup the physical connection with the material and leading five parameters to identify. However, the identification of these parameters is quite challenging and often requires an optimization algorithm (Rasilo, 2012). An optimization technique is developed by Chwastek et al. (2006) to estimate the parameters required for the JA model. Although various hysteresis models have been developed, the classical Preisach and the Jiles-Atherton models are still preferable methods for use in FE analysis. The conventional Presiach method is recognized as a complex model with high accuracy; on the other hand, the Jiles-Atherton model is famous for simplicity and less computation time (E. A. Dlala, 2008).

In the rotating machine, the existence of rotating flux causes the local flux density $\boldsymbol{B}$ and field strength $\boldsymbol{H}$ loci to be rotational rather than one-directional alternating (Rasilo, 2012). Modelling a vector hysteresis model is a challenging task as the magnetization process significantly changes at different magnetization levels under rotational flux condition(L. Dupré & Melkebeek, 2003). L. R. Dupré et al. (1998) implemented the vector Preisach model in FE analysis both for scalar and vector potential formulation. They tested both models on the Transformer T joint to examine the effect of rotational flux on local $\boldsymbol{BH}$ loci. E. Dlala, Belahcen, and Arkkio (2010) improved the loss modelling property of Mayergoyz's vector hysteresis model by removing the phase difference between the moving circular magnetic flux density and the field strength and adding a new parameter in saturation.

Bergqvist (1996) proposed a general concept of vector hysteresis model from

the static JA by transforming the original differential equation to take the vector behaviour of magnetization with the vector applied field into account.

Aside from the static hysteresis model, a significant amount of efforts have been invested for extending the static model into the dynamic hysteresis model to understand the dynamic behaviour of the hysteresis loop. As the name suggests, the dynamic hysteresis model depends on the rate of change of the applied field and often called the rate-dependent model. The applied field rate affects the hysteresis loop through the eddy current and increases the loop size (Bertotti, 1998). As a result, the shape of the $\boldsymbol{BH}$ loop changes significantly, and many attempts have been made to extend the static classical Preisach or the Jiles-Atherton model to rate-dependent dynamic hysteresis model. Bertotti (1992) proposed a rate-dependent model of classical Preisach model by assuming a sinusoidal magnetization and showed that each fundamental loop in the Preisach model does not appear instantaneously rather than at a finite rate controlled by the rate of change of externally applied field. Moreover, the hysteresis loop also changes based on the increment of the magnetizing frequency. The dynamic hysteresis model is precisely involved with the Bertotti's loss separation theory (Bertotti, 1988). The existence of rate-dependent and rate-independent hysteresis loss phenomena in DPM leads to the excess loss term as $f^{1.5}$ of magnetization frequency presented in the loss separation model (Bertotti, 1988). Bernard et al. (2002) developed an inverse rate-dependent DHM by taking the flux density $\boldsymbol{B}$ as input and field strength $\boldsymbol{H}$ as output and implemented it in magnetic vector potential based FE simulation. A frequency-dependent hysteresis model was proposed by (D. Jiles, 1993). In his dynamic model, the domain wall movement is presented as a second-order differential equation, and the average value is taken to describe the whole material behaviour. The outcome leads to a differential equation that explains the displacement magnetization as the difference between the magnetization $\boldsymbol{M}$ at any given time $t$ and $\boldsymbol{M}$ when reached in DC magnetization curve

$$\delta \boldsymbol{M} = \boldsymbol{M}(t) - \boldsymbol{M}_o(\boldsymbol{H}) \tag{12}$$

It is noticeable that the $\boldsymbol{M}_o(\boldsymbol{H})$ is not time-dependent rather than path-dependent. The reviewed literature of the dynamic model in this section is mostly developed based on the static Preisach model or static JA model, as these two models are widely used.

### Eddy Current Losses

The eddy current in the iron core is induced due to the time-varying magnetic field present in the electrical machine. When the magnetic flux rapidly changes, a voltage is induced in the conducting magnetic material, which causes the eddy current flows through the magnetic material and leading to the dynamic iron loss. Bertotti (1985) explained the physical meaning of dynamic eddy current loss behaviour in ferromagnetic material. According to his explanation, the eddy current loss exists because of the local internal magnetic fields generated by the eddy current or other magnetic effects, i.e., magnetostatic or coercive, which counterparts the

applied external field and the competition between them raised when the magnetizing frequency becomes high. In the classical eddy current loss model, the distribution of magnetic flux density assumes to be uniformed in the material, as shown in Figure 10; however, the actual eddy current loss can be much higher than where the assumption made (Serpico et al., 2000).

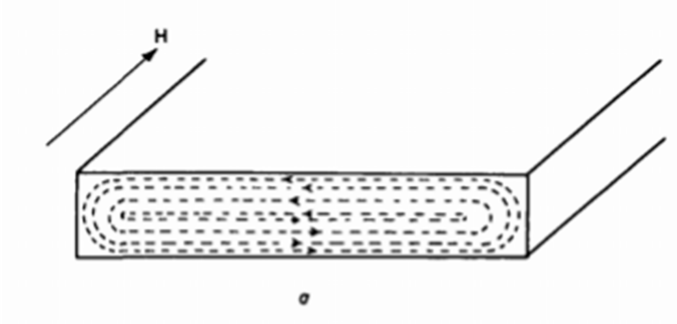


Figure 10: Uniform distribution of the classical eddy current in the electrical steel sheet thickness (Boon & Robey, 1968).

The approximate prediction of eddy current loss can be easily obtained by assuming that the permeability of the iron core does not vary with time and keep constant throughout the magnetization (Demerdash & Gillott, 1974). This assumption may provide the right prediction as long as the iron core remains in linear region in the magnetization curve. Moreover, the division of total iron loss into two components, such as hysteresis and eddy current loss is also debatable in the linear case. The hysteresis loss can be more dominant at low densities than the eddy current loss, and the division accuracy entirely depends on the questionable assumptions. Furthermore, the iron core often reaches the saturation region, and the permeability varies over a wide range, i.e., less or more with time. As the eddy current loss computed from the linear theory entirely depends on the permeability value; therefore, the prediction of eddy current loss from the linear approach may contain some quantitative meaning but not indicate any physical interpretation of this phenomenon (Agarwal, 1959).

Agarwal (1959) proposed the analytical eddy current loss model for solid and laminated iron based on the sinusoidal assumption of MMF wave. Practically, the MMF wave is non-sinusoidal due to the harmonics components in the rotating machine. It is clarified that the eddy current loss becomes more expensive for a solid iron core. Instead of using a solid iron core, the thin laminated iron core is used in the electrical machine to reduce the eddy current loss. The thickness of the stacked laminated steel sheet is much smaller than the transversal dimension. This geometry of the stacked laminated steel sheet provides the simplicity of assuming the magnetic field in two directions, and the eddy current loss can be modelled both analytically or numerically in one dimension (Labridis & Dokopoulos, 1989; Gyselinck et al., 1999; Bottauscio et al., 2000a). According to (Pippuri, 2010), 1D field assumption is studied by (Bottauscio, Chiampi, & Chiarabaglio, 2000b) and found that this approximation often overestimates the eddy current loss. The extension of the 1D eddy current loss model can be done by coupling with the 2D finite element model

(Rasilo, 2012; E. Dlala, Belahcen, & Arkkio, 2008). On the other hand, the 2D magnetic field problems can be approximated to the 1D eddy current loss model implemented in the post-processing stage (L. R. Dupré et al., 1998).

Several attempts have been made to include the eddy current loss directly in the FE solution; however, such approaches are not so obvious. Gyselinck et al. (1999) developed an eddy current loss model of lamination core and included directly in 1D and 2D FE solution. The coupling of 1D and 2D models is done through the nested iteration scheme by solving the non-linearity of these two model equations. Pippuri et al. (2010) explicitly studied the eddy current loss model inclusion in the 2D FE analysis coupled with 1D FE formulation. They pointed out that the iteration scheme for the 2D model often implemented incompletely as the field difference between the 1D and 2D models at the sheet boundary is often neglected frequently. It also clarified that the accomplishment of the coupling of the 1D and 2D models significantly depends on the estimation of field strength at the boundary of the sheet. The eddy current loss can not be studied explicitly such as the impact of skin and edge effect and the eddy current loss in small machine parts, e.g., teeth, tooth tips, bridges, etc., where the eddy current flows three-dimensionally by 1D or 2D models Handgruber et al. (2012). Thus, the computationally inefficient 3D analysis of eddy current loss (Dular et al., 1998) is often required to study explicitly. To reduce the computational time, a 2D coupled 3D model has proposed by Handgruber et al. (2012). A comparison between the extended version of Bertotti's loss segregation method and the proposed 3D eddy current loss model was conducted by Yamazaki and Fukushima (2010). The developed model computed iron loss using two terms, i.e., static hysteresis loss components and the eddy current loss components, where the excess loss is included in the dynamic eddy current loss by modifying the excess loss coefficient. The conventional three-term iron loss calculation method overestimates the eddy current loss competition for high skin effect and higher-order harmonics components.

**Excess Losses**

While the classical eddy current loss model is accounted for the homogeneous magnetization changes all over the material, the excess or anomalous loss is introduced due to the inhomogeneity of the magnetization process. Brailsford (1948) studied the unusual behaviour of eddy current loss in electrical sheet steel based on the assumption that the permeability can be dependent of the externally applied field but does not depend on the position in a material. According to his final remarks, the origin of anomalous loss can be primarily treated as a result of hysteresis effects but does not necessarily influence by the eddy current without proper justification.

Williams et al. (1950) investigated the eddy current loss in terms of domain configuration of the material. They observed that the discrete magnetization process occurs due to the domain wall motion, which makes the permeability of the material position-dependent. They pointed out that the anomalous loss introduced as a difference between the computed and measured magnetic loss can be adequately explained if the domain configuration of the material is taken into account. This

simple domain configuration concept is studied further by (Pry & Bean, 1958). Their study has been conducted so far by assuming a single infinitely thin domain wall and the uniform motion of the wall. However, the number of domain wall can be raised (Sun et al., 1971), and the motion of each and an individual wall can be non-uniformed if the magnetization process is dynamic (Shilling & Houze, 1974). The effect of the movement on walls having different finite width and the associated power loss has been studied by (Sun & Kramer, 1977). They clarified that the power loss becomes more when the wall width increases; on the other hand, the power density decreases and the motion does not have a significant impact on the wall width.

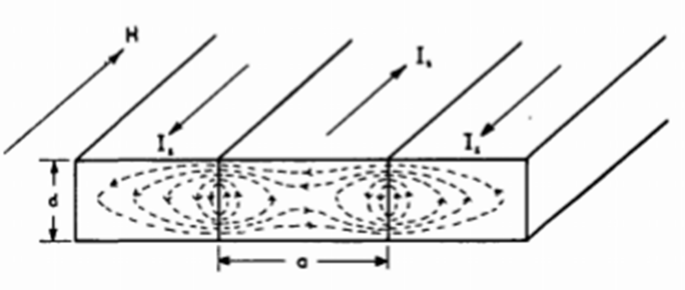


Figure 11: Domain wall motion effects on eddy current (Boon & Robey, 1968).

Shilling and Houze (1974) extensively studied the domain structure theory and the related power loss of grain-oriented materials and initiated a concept to separate the total iron loss into hysteresis, classical eddy current and excess loss components. However, the proper characterization of excess loss components was still absent for non-oriented material and the various conditions of domain structure, grain size and domain orientation etc. Owing to this loss separation concept, Bertotti (1985) proposed a simple method and a common framework to segregate the iron loss statistically, which can be reasonably applicable for any iron materials and various conditions of domain structures. He introduced the concept of a magnetic object (MO) which can represent a group of adjacent walls having strong correlation as a single object in terms of dynamic and structural properties. The allocation of active MO's during the magnetization process leads to a simple loss formulation, and it allows to express the relation between the excess loss and the dynamic structure in a single quantity. However, the model can account the excess losses due to the microscopic eddy current induced during domain wall motion as illustrated in Figure 11 and compensate for the skin effect as an excess loss (Belahcen et al., 2014). It is worth noticing that the excess loss is primary existed under the alternating flux variations but virtually zero under purely rotational flux variation (Belahcen et al., 2014).

In statistical loss segregation model, the excess losses were represented as a difference between the measured total iron losses and the losses computed from the first two terms (e,g. hysteresis and eddy current losses) of the loss segregation model with uniformity assumption (Overshott et al., 1968), however, in practically the contribution of excess or anomalous losses to the total iron losses can be less than

the losses predicts by Bertotti's model (Rasilo, 2012). Thus, the excess losses need to be modelled completely or partly even if the non-uniformity of flux density and eddy current in lamination thickness is estimated accurately (Mayergoyz & Serpico, 1999). The iron loss components are not entirely free from each other and have some internal dependency. (D. C. Jiles, 1994) showed that including the effects of excess loss components along with the classical eddy current loss components in the hysteresis model significantly increases the coercivity of the hysteresis curve, hence, increase the losses. The interdependence among the iron loss components in the laminated magnetic core has been explicitly studied by (E. Dlala, Belahcen, Pippuri, & Arkkio, 2010). They clarified that the eddy current significantly affects the hysteresis and the excess loss components in machine core and influence them to depend on the excitation frequency.

## 2.3 Overview of Iron Loss Models

In the previous section, the various models of iron loss components are studied separately. In this section, the analytical and numerical methods for iron loss calculation is reviewed, and the suitable loss model is chosen to compute the total iron loss from FE solution in the post-processing stage.

### 2.3.1 Alternating Flux Loss Models

Before the availability of numerical analysis tools, the researchers had developed analytical models to estimate the losses in electrical machines. The accuracy of developed analytical models was often compared with the experimental results. Steinmetz (1892) developed an iron loss model based on the measurement data

$$P_{fe} = \ C_{ce}\ f^{\alpha}\hat{B}^{\beta} \tag{13}$$

where $\hat{B}$ represents the peak flux density of the material, and $C_{ce}$, $\alpha$, and $\beta$ are three coefficients that can be estimated from the measurement data by fitting the loss model. The application of the Steinmetz model is limited to pure sinusoidal flux density waveforms. Moreover, the three iron loss components can not be separated in his model. The Steinmetz model was extended by Jordan (1924) for differentiating the iron loss components separately

$$P_{fe} = \ P_{hys} + \ P_{ed} = C_{ch}\ f\hat{B}^2 + \ C_{ce}\ f^2\hat{B}^2 \tag{14}$$

where $P_{hys}$, and $P_{ed}$ refers the hysteresis and eddy current loss, $C_{ch}$ and $C_{ed}$ denotes the hysteresis loss coefficient and the eddy current loss coefficient, respectively.

Jordan (1924) continued Steinmetz's model considering the hysteresis and eddy current losses; however, the excess loss component is still absent. In his model, hysteresis losses are presumed to be proportional to the hysteresis loop at low frequency, and the eddy current can be roughly estimated from Maxwell's equations (Krings & Soulard, 2010).

A new model including excess loss was presented by Bertotti et al. (1988) where the total losses are segregated statistically

$$P_{fe} = P_{hys} + P_{ed} + P_{ex} = C_{ch}\, f\hat{B}^2 + (\pi^2\sigma d^2\, f^2\hat{B}^2)/6 + C_{ex} f^{1.5}\hat{B}^{1.5} \tag{15}$$

where $P_{ex}$ is the excess loss components,$C_{ex}$ is the excess loss coefficient, $d$ is the thickness of the electrical steel sheet, and $\sigma$ is material conductivity. The benefit of this empirical approach is, it requires less computation process as a set of measurement data and knowing the material's flux density profile enough to estimate the iron losses (Rajamäki, 2019). Like (Steinmetz, 1892) and (Jordan, 1924) model, the flux density is also assumed purely sinusoidal in the statistical loss model. However, the flux density waveforms in electrical machines are often non-sinusoidal due to harmonic components, which leads to inaccuracy in loss calculation where the flux density is expected to be sinusoidal Albach et al. (1996).

Fiorillo and Novikov (1990) developed a model influenced by Bertotti et al. (1988) statistical loss segregation model to take the non-sinusoidal characteristics of the flux density into account. In the statistical loss segregation model, the excess losses were represented as a difference between the measured total iron losses and the losses computed from the first two terms, i.e., hysteresis and eddy current losses of the loss segregation model with uniformity assumption Overshott et al. (1968). In practice, the contribution of excess losses to the total iron losses can be less than the losses predicts by Bertotti's model. Thus, the excess losses need to be modelled completely or partly even if the non-uniformity of flux density and eddy current in lamination thickness is estimated accurately (Mayergoyz & Serpico, 1999). Moreover, the statistical loss segregation model has relatively good accuracy for low magnetizing frequencies and thin lamination thickness, where the skin effect is imperceptible. However, the situation may be different when the frequency is high, or the lamination is thick enough to exaggerate the skin effect, which affects the hysteresis and excess loss components (Belkasim, 2008). Besides, the flux density is assumed uniform along with the lamination thickness. In reality, the flux density is non-uniform inside the material that may affect the eddy current computation (Saitz, 2001). Kampen et al. (2012) compared several iron loss models and showed that the Steinmetz model and the statistical loss segregation models are fast, easy to implement and could be applicable for iron loss estimation roughly.

However, many researchers have developed the Steinmetz-Jordan model later and estimated iron losses using these empirical models conventionally (Arkkio & Niemenmaa, 1992; Ali et al., 1997). In this thesis, the empirical models based on the Jordan extension model presented on (Belahcen & Arkkio, 2008) is adopted for the iron loss computation.

$$P_{hys} = \int_V (\sum_{n=1}^{N} C_{ch}(n\omega_s)\hat{B}_n^2) dV \tag{16}$$

$$P_{ed} = \int_V (\sum_{n=1}^{N} C_{ce}(n\omega_s)^2\hat{B}_n^2) dV \tag{17}$$

where $P_{hys}$ and $P_{ed}$ represents the hysteresis and eddy current loss, respectively. $C_{ch}$ and $C_{ce}$ expresses the hysteresis and eddy current loss coefficients, $\omega_s$ stands for the angular frequency and $\hat{B}$ the peak flux density values at $n^{th}$ harmonic components. It is noticeable that the excess loss is included in the dynamic eddy current loss $P_{ed}$ model.

### 2.3.2 Rotational Flux Loss Models

In practice, the alternating and the rotating flux density components both exist in rotating machines. Baily (1896) studied the rotational and alternating hysteresis loss in both soft and hard magnetic material. Rotational hysteresis loss component is more dominant than the alternating hysteresis loss component up to a certain level before the flux density values reach to the saturation. Then, the rotational hysteresis loss drops rapidly and vanishes entirely; on the other hand, the alternating hysteresis loss becomes more presiding and continue rising with the increasing flux density values. The core of the rotating machine is subjected to a large degree of rotational flux. Even the losses caused by rotational flux components can suppress the losses due to the alternating flux components at high magnetization levels (Moses, 1992). As alternating flux density can be sinusoidal or non-sinusoidal, similarly, the rotational flux density can be purely rotational, i.e., circular or non-purely rotational, i.e., elliptical because of the harmonic components. Different methods for measuring the rotational core loss are reviewed by Guo et al. (2008). Enokizono et al. (1991), and Enokizono and Sievert (1989) proposed two models for calculating the rotational core loss based on measurement data of magnetic flux density $\boldsymbol{B}$ and the magnetic field strength $\boldsymbol{H}$ in electrical sheet steel

$$P_t = \frac{1}{\rho T}\int_0^T (H_x \frac{dB_x}{dt} + H_y \frac{dB_y}{dt})dt \tag{18}$$

$$P_r = \frac{\omega}{\rho T}\int_0^T (H_x B_y - H_y B_x)dt \tag{19}$$

where $\rho$ refers to the mass density, $\omega$ is the angular frequency, and $H_x$, $H_y$, $B_x$, $B_y$ stands for the magnetic field strength and magnetic flux density in $x$, and $y$ directions respectively. Equation 18 has good accuracy under any flux conditions, but Equation 19 gives inaccurate results for non-purely rotational flux conditions (Atallah & Howe, 1993). However, the loss Equations 18, and 19 are valid for any vector magnetic flux density $\boldsymbol{B}$, and the field strength $\boldsymbol{H}$ where the rotational flux loci is just one of the application of these loss expressions. The investigation of rotational core loss in electrical sheet steel is continued by (Fiorillo & Rietto, 1993; Kochmann, 1996; Zhu & Ramsden, 1998).

Belahcen et al. (2014) proposed a method based on loss separation theory where the hysteresis losses are segregated into the alternating and rotational losses. A detailed comparison of power loss in electrical sheet steel under alternating and rotating flux conditions are presented in (Sievert et al., 1996).

### 2.3.3 Harmonic Loss Models

The ferromagnetic parts of the stator and rotor are subjected to a highly distorted magnetic flux density. The effects of armature reaction and the main field, the slotted nature of the machine, and the highly distorted magnetic field appears from the permanent magnet causes the non-sinusoidal variations of the magnetic flux density waveforms and creates the time dependency. Thus, the flux density in the rotating machine is not a single frequency component any more and contains higher frequency components. The advancement of the computation device and numerical methods makes it possible to calculate the iron loss considering the harmonic components of the flux density. The excellent accuracy and the detail study opportunity influence the researchers to compute the iron loss based on the harmonics components. In the last few decades, researchers have developed and applied different harmonic loss computation techniques. Moses and Shirkoohi (1985) introduced an approach to calculate the total iron loss using the flux density values at different harmonics order

$$P_{fe} = \pi f \sum_{i=1}^{\infty} n \boldsymbol{B}_n \boldsymbol{H}_n \sin \phi_n \tag{20}$$

where $n$ is the harmonic orders, $f$ is the fundamental frequency, $\boldsymbol{B}_n$, and $\boldsymbol{H}_n$ represents the peak flux density at each harmonics components respectively, and $\phi_n$ is the phase angle between them. Moses and Shirkoohi (1985) highly recommended to use the phase angle $\phi_n$ as it has a considerable impact on loss estimation, and neglecting can lead to 30 % erroneous results. It can be noted that the Fourier decomposition of Equation 18 leads to Equation 20; thus, both loss expressions convey the same meaning mathematically. Equation 20 has the flexibility as no differentiation of the flux density $\boldsymbol{B}$, and the field strength $\boldsymbol{H}$ is required; however, the estimation of the phase shift is not necessarily more accurate. Therefore, Equations 18, and 20 holds the same degree of errors.

One of the most widely used methods for iron loss computation is the Fourier decomposition of the magnetic flux density at each finite element. This method offers a great deal to study each and individual harmonic loss components. In this method, the total iron loss can be calculated as the sum of all the higher harmonics contributions.

Yamazaki and Watari (2004) compared two methods of iron loss computation from the flux density harmonics. The comparison stands between the iron loss calculation from the Fourier decomposition of the flux density, and directly from the flux density waveforms without performing the Fourier Transform. Yamazaki claimed that the Fourier Transform based method could not decompose the hysteresis loss into harmonics components due to the non-linear characteristics and often overestimate hysteresis loss computation for a highly saturated machine. Nakata et al. (1970) implied that the hysteresis loss is fixed for a particular peak flux density in a given material for a given excitation frequency. Many authors (Faiz & Sharifian, 1994; Yamazaki, 2003; Hu et al., 2008) claimed that the hysteresis loss can not be computed as a sum of contributions of various harmonic components and does not follow the general decomposition. Thus, they preferred to calculate the eddy current loss from

the Fourier decomposition while the hysteresis loss can be determined directly from the flux density waveforms using the peak value. Such approaches are applicable where the minor hysteresis loops are neglected (Rupanagunta et al., 1991) or assumed the sinusoidal variation of the flux density waveforms. In practice, rotating machines are not free from minor hysteresis loops due to the flux density harmonics, which offers a significant challenge for core loss estimation (Alatawneh & Pillay, 2014). In fact, hysteresis losses are more related to the minor loops compared to the harmonics content of the flux density (Leonardi et al., 1996). Of course, it is not recommended to compute the hysteresis loss from the Fourier decomposition of the flux density waveforms. However, many authors (Hudak et al., 2004; Leonardi et al., 1996; Saitz, 2001; Ali et al., 1997; Arkkio & Niemenmaa, 1992) have been applied this method and achieved relatively good accuracy with the measurement results. In this thesis, both the eddy current and hysteresis loss are computed from the Fourier decomposition of the flux density waveforms.

## 2.4 Chapter Summary

The complexity involved in iron loss computation urges deep prior knowledge. With this notion, the basic construction and mechanism of various synchronous machines are highlighted in Section 2.1. Section 2.2 presented the types of electromagnetic and mechanical losses experienced by the synchronous machine during the operation. Besides, the sources of iron loss contributors and their individual loss models are studied with great interest in order to understand the concept of iron loss profoundly. Moreover, the comparison of different iron loss models in electrical machines, their application, limitations and flexibility are carried out in Section 2.3. The theory behind the Finite Element Method and application of obtaining the static and dynamic field solution and the iron loss computation using these solutions are discussed in the next chapter.

# 3 Research Methodology

In this chapter, the methodology of iron loss computation from the static field and the dynamic field solution in 2D Finite Element Method are described step by step. At first, a brief description of solving the boundary value problems through a standard FEM scheme and the iron loss implementation practice in FEM is presented in Section 3.1. An introduction to the 2D FEM software FCSMEK and the routines for analysing the synchronous machine is described in Section 3.2. Section 3.7 contains the procedure of obtaining a static field solution in FEM, and iron loss computation process using this field solution. Moreover, the method of dynamic field calculation and the iron loss computation process is also described in Section 3.8.

## 3.1 Finite Element Method

The human mind faces difficulty to catch the behaviour of a complex system in one operation. Therefore, subdividing a complex system into their components or elements and study each component's behaviour, and then reforming the whole system from those components is the smooth and efficient way of understanding the overall system behaviour. Moreover, the formulation of space and time-dependent problems are generally based on the partial differential equations (PDE). An analytical approach cannot solve these PDE problems due to extensive geometries and difficulties. Instead, different discretization methods are used to approximate these PDEs with numerical model equations. Thus, a numerical approach is required to solve these numerical model equations.

A finite element is a numerical method to solve PDE problems, which result from the field of engineering and mathematical physics. Developing two discretization schemes by Lord Rayleigh (1870) and W. Ritz (1909) on variational methods, and then B.G Galerkin's (1915) weighted residual methods initiated the theoretical background of finite element method (Leissa, 2005). Clough (1960) coined the term 'Finite Element' with the invention of classical displacement formula for plane strain triangles. At first, the development of the finite element method was limited in the structural mechanic's community serving for the aircraft industry and drawn the attention of the mathematicians much later. However, a significant breakthrough occurred in electro-magnetics when Winslow (1964) used a similar approach as a finite element method to solve the electromagnetic field problems. Later, Silvester (1969) advanced the method by forming high order polynomials triangular elements using simplex coordinates, and since then many researchers have developed and utilized the finite element method in the field of electro-magnetics.

Luomi (1993) explained that the energy conversion process of electrical machines depends on the interaction of the electromagnetic field in the air gap. Thus, the design and analysis of electrical devices are usually accomplished based on the complete solution or the approximation of the field. The complex geometry of the electrical machines and the time dependency of the field components offer a hard challenge for the accurate estimation of the magnetic field. Luomi (1993) also described different methods used for computing the electromagnetic field or solving the boundary value

problems. However, the advancement of modern computational tools has made the Finite Element Method (FEM) a great deal with the complicated issues, consequently, solving the field equation directly (Luomi, 1993).

Either using of variational or residual discretization method, the accuracy of solving partial differential function (PDEs) depends on selecting the approximation function for the entire problem domain. Furthermore, the chosen function also needs to satisfy the necessary boundary conditions, but the complex machine's geometry causes this task more difficult. Therefore, the basic idea of FEM is to divide a large complex problem domain into smaller areas or elements. At first, a suitable algebraic polynomial function can be chosen to approximate the solution within each element, and then the solution of each element can be assembled to represent the whole problem domain. As Bastos and Sadowski (2003) described, the implementation of the residual method is more comfortable as it can be formed directly from the physical equation that needs to be solved. Thus, the FEM is preferably modelled in electromagnetism based on the residual method over the variational method.

Analysis of electromagnetic problems mainly requires solving a bunch of Maxwell's electromagnetic equations with the necessary boundary conditions. Therefore, the solution of the electromagnetic field can be obtained simplifying and solving the differential form of Maxwell's equation subject to given boundary conditions through the Finite Element Method (FEM).

The differential form of Maxwell field equations can be presented as follows

$$\nabla.\boldsymbol{B} = 0 \tag{21}$$

$$\nabla \times \boldsymbol{E} = -\frac{\partial \boldsymbol{B}}{\partial t} \tag{22}$$

$$\nabla \times \boldsymbol{H} = \boldsymbol{J} + \frac{\partial \boldsymbol{D}}{\partial t} \tag{23}$$

In case of, quasi static ($\frac{\partial \boldsymbol{D}}{\partial t} = 0$) and static ($\frac{\partial \boldsymbol{B}}{\partial t} = 0$) problems, the above equations can be rewritten as following

$$\nabla.\boldsymbol{B} = 0 \tag{24}$$

$$\nabla \times \boldsymbol{E} = -\frac{\partial \boldsymbol{B}}{\partial t} = 0 \tag{25}$$

$$\nabla \times \boldsymbol{H} = \boldsymbol{J} \tag{26}$$

The material equations can be given as

$$\boldsymbol{B} = \mu \boldsymbol{H} \tag{27}$$

$$\boldsymbol{J} = \sigma \mathbf{E} \tag{28}$$

Usually, the above differential equations are formulated in terms of magnetic potential, and then the solution is achieved through the space discretization or subdivision of

the problem domain. Besides, the existing time-dependent term in the equations demands time discretization. However, the non-existence of time-dependent term in the static case leads to omitting the time discretization. Moreover, the non-linear properties of the core material should be taken into account and solved by using the Newton-Raphson method.

The solution of the three-dimensional field is still tedious and requires lots of tasks. On the other hand, the solution becomes much easier if the problem domain is simplified to the two-dimensional model where the machine geometry and material equations are independent of coordinate parallel to the machine shaft, i.e., z-coordinate (Arkkio, 1987). Therefore, the field solution is assumed to be two dimensional. The fundamentals of FEM for solving 2D field equations in radial flux machines is discussed in the following section.

### 3.1.1 Magnetic Vector Potential

In electromagnetism, the magnetic field solution is often computed by introducing magnetic potential in the field equation. The term 'magnetic potential' refers to either the magnetic scaler potential or the magnetic vector potential. Unlike vector potential, the scalar potential has limited usage as scaler potential can only apply for an irrational magnetic field, i.e., no free current density present in the solution region. On the other hand, the magnetic vector potential is used to take the rotational aspect of the magnetic field. Moreover, the magnetic vector potential reduces the vector problems into a scaler problem. The application of magnetic vector potential is indispensable in three-dimensional cases. However, the magnetic vector potential is also widely used to solve the magnetic field equations in two-dimensional cases (Luomi, 1993).
Magnetic vector potential $\boldsymbol{A}$ can be defined as

$$\boldsymbol{B} = \nabla \times \boldsymbol{A} \tag{29}$$

The current density $\boldsymbol{J}$ can be expressed in terms of vector potential $\boldsymbol{A}$ by substituting Equation 29 in Equation 26, and placing reluctivity $\nu = 1/\mu$ as following

$$\nabla \times (\nu \nabla \times \boldsymbol{A}) = \boldsymbol{J} \tag{30}$$

It is worth noticing that Equation 30 satisfy all magneto-static problems. In the two-dimensional case, Equation 30 can be formulated as

$$\nabla.(\nu \nabla \times \boldsymbol{A}) = -\boldsymbol{J} \tag{31}$$

This is called div-grad equation or Poisson's equation, i.e., the material reluctivity $\nu$ constant. In the two dimensional cases, the partial differential Equation 30 of the magnetic vector potential $\boldsymbol{A}$ can be written as

$$-[\frac{\partial}{\partial x}(\nu \frac{\partial A_z}{\partial x}) + \frac{\partial}{\partial y}(\nu \frac{\partial A_z}{\partial y})] = \boldsymbol{J} \tag{32}$$

It can be noted that the magnetic vector potential $\boldsymbol{A}$ lies only in the $z$ direction which can be represented by a unit vector $e_z$ and remains constant in the direction

of flux density. The magnetic vector potential $\boldsymbol{A}$ for each nodal indices are solved by choosing a suitable algebraic polynomial, which is discussed briefly in the following section.

### 3.1.2 Space Discretization or Domain Subdivision

In FEM, the problem domain is divided into the small non-overlapping area called elements. The dividing process is often familiar as meshing, and the elements of the entire problem domain are known as mesh. The corners of each element are known as nodes, and one node can belong to several elements. In general, a shape function is assigned over each element to find out the best possible solution for the unknown vector potentials. The solution accuracy depends on the order of the shape functions. Moreover, different types of element shapes are used based on the analysis interest. For instance, in the 2D case, triangular element shapes are chosen quite often; on the other hand, tetrahedral or hexahedral shapes are used for 3D analysis. The first order, second order or third order triangular elements as shown in Figure 12 are used in the 2D analysis. The nodes of each triangular element are numbered in an anticlockwise direction. Usually, higher-order polynomial functions approximate the solution more accurately but increase the computation time. Thus, the selection of polynomial or shape function is made by treading off between computation time and accuracy (Bikram Shah, 2013).

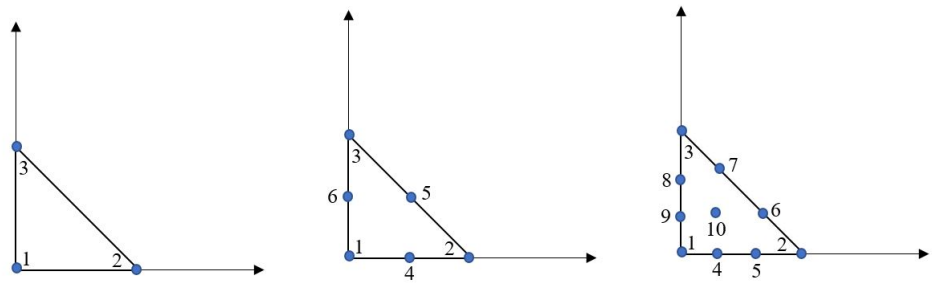


(a) (b) (c)

Figure 12: Different orders of a triangular element: (a) First order triangular element ; (b) Second order triangular element; (c) Third order triangular element.

At first, the elements are generated in the local coordinate system $(\xi, \eta)$ for simplicity and then transform to the global coordinate system $(x, y)$ through a unique transfer system, as shown in Figure 13.

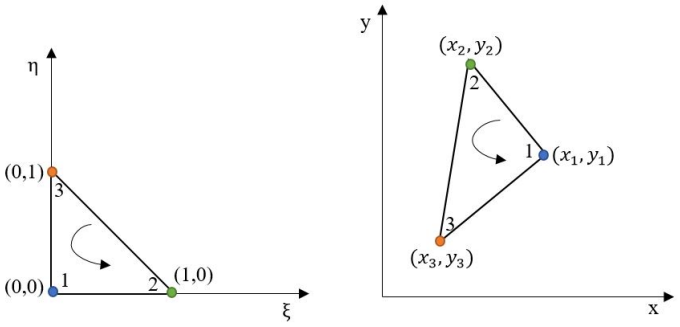


(a) (b)

Figure 13: Element coordinate transformation: (a) Element in local $(\xi, \eta)$ coordinate ; (b) Element in global $(x, y)$ coordinate.

The global shape function has non zero value only those elements that share its nodal point and zero for other elements as depicted in Figure 14.

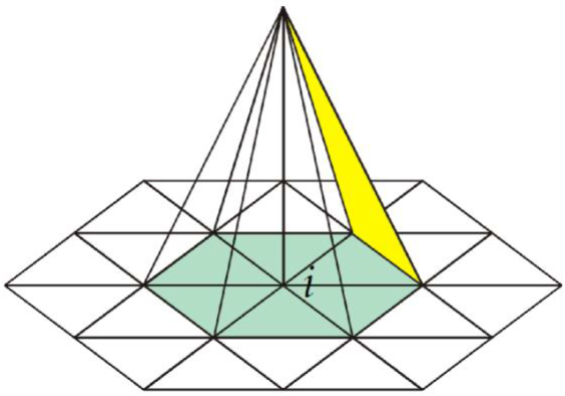


Figure 14: Elements share the nodal point $i$ (Arkkio & Sundaria, 2018).

After meshing, the magnetic vector potential is generated over each element by shape function leading to

$$\boldsymbol{A}(x, y) = \sum_{i=1}^{n} \mathbf{a}_i N_i(x, y) \tag{33}$$

where $N_i$ is the global shape function which has a non-zero value at node $i$ depicted in Figure 14, $n$ is the total number of nodes and $\mathbf{a}_i$ is the nodal value at nodal point $i$. Moreover, the time dependence of the magnetic vector potential $\boldsymbol{A}$ in dynamic field problems requires time discretization, which can be accomplished using the Crank-Nicolson time-stepping method as described in Section 3.5. Maxwell equation is satisfied inside the problem domain as shown in Figure 15 but it is also essential to know the magnetic vector potential in the boundary of the problem domain. Thus, the necessary boundary conditions that need to satisfy is described in the next section.

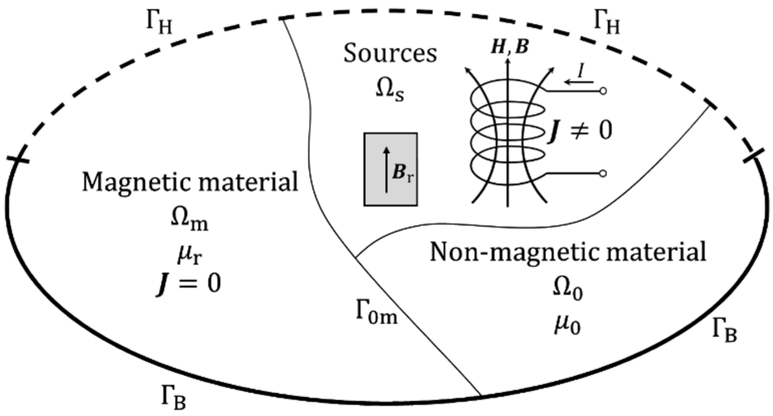


Figure 15: Problem domain with boundary conditions (Farzam Far, 2019).

### 3.1.3 Boundary Conditions

The magnetic vector potential $\boldsymbol{A}$ must be known in the boundary region of the problem domain for the field calculation (Arkkio, 1987). In electrical machines, the boundary region can be the borders of the outer surface or interfaces between different materials inside the machine. The most common boundary conditions for 2D machine analysis are Dirichlet, Neumann and (Anti) periodic boundary conditions.

In the Dirichlet boundary condition, the vector potential $\boldsymbol{A}$ is constant, and the field is parallel to the boundary. When this boundary condition is applied, i.e., the outer surface of the machine, no flux passes through the boundary.

In the homogenous Neumman boundary condition, the field is perpendicular to the boundary, i.e., $\nu \frac{\partial \boldsymbol{A}}{\partial n} = 0$.

Typically, in an electrical machine, the same geometry repeats itself after one or two pole pitches. The (Anti) periodic boundary condition is used for modelling the symmetry sector, i.e., $\boldsymbol{A}_1 = \pm \boldsymbol{A}_2$.

### 3.1.4 Solving Non-linearity

The ferromagnetic material parts often introduce non-linearity in the electrical machines. The magnetic saturation and hysteresis characteristics of iron material offer intense challenges for the flux density computation. The material reluctivity $\nu$ present in Equation 30 depends on the square of the flux density; hence, it introduces non-linearity. However, Equation 30 should be linearised that can be achieved through the iteration method. In 2D FEM, the non-linearity is usually tackled by using Newton-Raphson iterative scheme where the nodal value $\boldsymbol{a}$ is revised at each step $k$ of iterations (Luomi, 1993) as

$$\boldsymbol{a}^k = \boldsymbol{a}^{k-1} + \Delta \boldsymbol{a}^k = \boldsymbol{a}^{k-1} - \boldsymbol{J}^{-1}\mathbf{r}(\boldsymbol{a}^{k-1}) \tag{34}$$

where $\boldsymbol{J}$ represents the Jacobian matrix and the entry in Equation 34 as

$$\boldsymbol{J}\Delta \boldsymbol{a}^k = -\mathbf{r}(\boldsymbol{a}^{k-1}) \tag{35}$$

The Jacobian matrix $\boldsymbol{J}$ is updated at each step $k$, based on the nodal values at previous step ($\boldsymbol{a}^{k-1}$). Finally, the non-linear problem is solved into consecutive linear problems.

### 3.1.5 Iron Loss Implementation Practice in Finite Element Method

The magnetic fields in an electrical machine depend on the time; therefore, the time dependence of the magnetic fields need to be solved step by step. Bouillault and Razek (1983) showed an approach to solve the time dependency of the magnetic fields through time-stepping methods in the solid rotor induction machine. The voltage equations of electrical machines are not independent rather than coupled with the field equations. If the source of the field is taken from the stator winding current such as earlier publications, e.g., (Andresen & Müller, 1983), then the solution can be obtained by solving the voltage equations and field equations through the separate iterations. However, if the machine is fed from the voltage supply or the source of the field is taken from the voltage supply, then the most efficient method is to solve the voltage equations and field equations in the same Finite Element (FE) solution within the same iteration loop. Thus, the coupling of voltage and field equations is essential to compute the current of the winding accurately as well as for the correct computation of other quantities such as torque and losses (Belahcen et al., 2016).

The coupled voltage equations and field equations in the same FE solution were solved by Brandl et al. (1975) to find out the steady-state characteristics of the synchronous machine. Arkkio (1987) also explained the coupled voltage equations and the field equations of an induction machine in the same iteration loop. E. Deng and Demerdash (1996) developed a time-stepping coupled finite element state space (CFE-SS) model for synchronous generator using the natural time domain ABC flux linkages reference frame to predict the steady-state characteristics of the generator. As the field equations are time-dependent in such approaches, thus, the resulting magnetic field also depends on time.

Knight et al. (2009) developed a computationally effective analytical approach from a few magnetostatic Finite Element Analysis (FFA) solutions to computing the flux density in large synchronous machines. Knight et al. (2009) applied his model to derive the stator core losses assuming the uniform flux in the back iron between teeth. Hafner et al. (2010) have attempted another time effective analytical method to calculate the static electromagnetic field in Permanent Magnet Synchronous Machine (PMSM) by conformal mapping in the frequency domain. However, the above attempts have been made from taking FEA solutions as input data and developed model outside of FEA or as an alternative method of FEA.

Belahcen et al. (2016) developed a systematic approach for coupling the static field equations and space vector model within the same Finite Element (FE) solution. At first, the model has performed on Permanent Magnet Synchronous Machine (PMSM), and later on Bearing less Synchronous Reluctance Machine (BSRM), the method has given accurate results with the measurement and time-stepping finite element analysis and significantly reduced the computational time. The possibility of iron loss computation from the developed static field solution opens a new scope of research,

and a proper estimation of iron loss can significantly reduce the computational time, and substitute the time consuming transient analysis.
To calculate iron loss from this dynamic solution, the time dependence of the magnetic field needs to solve through the time-stepping simulation for each time step. The most common practice of iron loss computation is to obtain the flux density distribution from time-stepping FE simulation and calculate the iron loss in the post-processing stage using the obtained flux density distribution (F. Deng & Demerdash, 1998; Hudak et al., 2004). However, such approaches require a substantial amount of computation time (Belahcen et al., 2016).

Another method is to include the iron loss in FE formulations; however, such approaches are not conventional, and not many published works are readily available to understand the effect of iron loss on the FE solution. A comprehensive study of iron loss inclusion in the FE solution was performed by E. Dlala, Belahcen, and Arkkio (2010) in an induction machine. The outcome of their research work was that the total iron loss decreased 15% after including in the FE solution.

With the notion of minimizing the computation time, a few attempts (Fouad et al., 1981; Schifer & Lipo, 1989; Al-Din et al., 1997) have been made to obtain the time dependence of the flux density from several static simulations, hence, compute the stator iron loss in the synchronous machine from the harmonic components of the flux density waveform by means of Fourier transformation. In such approaches, the time variation of the nodal values is introduced by solving a number of static simulations where the rotor position is varying with respect to stator at one slot pitch interval. It is clarified that such approaches can reduce the computational cost compared to the time-stepping simulation but the requirements of the number of static simulations, i.e., field solutions may still need a substantial amount of computation time. The difference may be more visible when the proposed method can compute the iron loss from a single static simulation.

## 3.2 Introduction to FCSMEK

A Finite Element solver tool based on magnetic vector potential is required to calculate the iron loss from a static field solution. FCSMEK is a FORTRAN programming language-based software developed by the electro-magnetics research group at Aalto University for 2D Finite Element analysis of radial flux machine based on magnetic vector potential. FCSMEK has a collection of routines for analysing the synchronous and asynchronous machines. Some basic routines for analysing the synchronous machine are shown in Figure 16.

MESH is a preprocessing routine for discretizing the geometry of a synchronous machine. The program generates a two-dimensional finite element mesh for the cross-section of the machine, and deduce the smallest symmetry sector. The mesh can be formed with first, second, or third-order isoparametric triangular elements.

SYDC is the FE analysis program to obtain the initial state for time-stepping simulation from the static FE solution. In this routine, the characteristics of the synchronous machine are computed based on the dc field analysis. The static FE solution is achieved through solving the circuit equations of the stator winding based

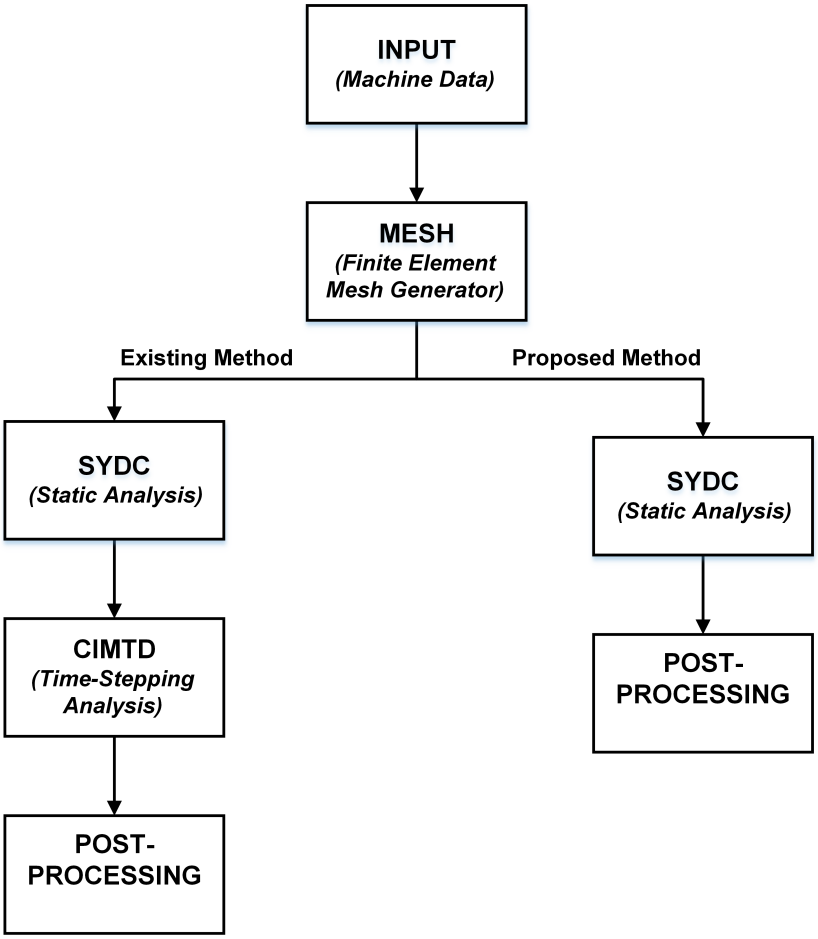


Figure 16: FCSMEK routines for synchronous machine.

on the two-axis model, and the field equations. The non-linearity of the system is solved using the Newton-Raphson iteration method.

CIMTD is the FE analysis program for time-stepping simulation of the synchronous machine. The operating characteristics of the synchronous machine are obtained by solving the field equations and the circuit equations for each time step using the Crank-Nicholson time-stepping method. The rotor motion is taken into account in this routine by changing the air gap mesh. The non-linearity of the iron is solved using the Newton-Raphson iteration method.

Currently, the iron loss is computed through time-stepping simulation using CIMTD routine in the post-processing stage. However, the proposed method can compute the iron loss in advance using the SYDC routine in the post-processing stage. Moreover, several post-processing routines such as cimpiir, and cimplot, etc. are used for plotting the solutions.

## 3.3 Static Field Solution

Static analysis is one of the preferable methods for analysing the synchronous machine as it allows to analyse the machine from a single static simulation with relatively good

accuracy. As a result, the simulation time is reduced significantly and profitable to a wide range of applications. The solution can be achieved by solving a standard static equation through Finite Element approach and merged with the two-axis space vector model of a synchronous machine. Thus, a standard static Equation 26 demonstrated in Section 3.1 is recalled in this section.

$$\nabla \times \boldsymbol{H} = \boldsymbol{J} \tag{36}$$

where $\boldsymbol{H}$ is the magnetic field strength, and $\boldsymbol{J}$ is the total current density in the material. Introducing the magnetic vector potential $\boldsymbol{A}$, and the material reluctivity $\nu = \frac{1}{\mu}$ instead of material permeability $\mu$ transform Equation 36 as

$$\nabla \times (\nu \nabla \times \boldsymbol{A}) = \boldsymbol{J} \tag{37}$$

The ferromagnetic materials are often used in electrical machines, which are subjected to a strong non-linearity. Therefore, the material reluctivity $\nu$ also depends on a non-linear function of magnetic vector potential $\boldsymbol{A}$ in Equation 37. In a material, the movement of free current-carrying charges is mainly formed the current density $\boldsymbol{J}$. However, some other bound charges that can also contribute to the current density $\boldsymbol{J}$. In magnetic materials, the movement of a magnetic dipole moment introduces the magnetization $\boldsymbol{M}$ current and forms the magnetization current density $\boldsymbol{J_M}$. Thus, the total current density $\boldsymbol{J}$ can be formed as a combination of main current density $\boldsymbol{J}$ and the magnetization current density $\boldsymbol{J_M}$, and Equation 37 can be rewritten as

$$\nabla \times (\nu \nabla \times \boldsymbol{A}) = \boldsymbol{J} + \boldsymbol{J_M} \tag{38}$$

The entry of magnetization current density as $\boldsymbol{J_M} = \nabla \times \boldsymbol{M}$ transform Equation 38 as follows

$$\nabla \times (\nu \nabla \times \boldsymbol{A}) = \boldsymbol{J} + \nabla \times \boldsymbol{M} \tag{39}$$

The assumption of the uniform current distribution is essential to compute the current density for any wound machine windings. The static solution is achieved through a standard Finite Element Method by space discretization of Equation 39, discretizing the nodal values of the magnetic vector potential in each element by introducing weight function with the shape functions and handling the iron non-linearity using the Newton-Raphson iteration scheme, which transforms Equation 39 to a linear algebraic equation:

$$\boldsymbol{S a} = \boldsymbol{F} \tag{40}$$

where $\boldsymbol{S}$ is the stiffness matrix, $\boldsymbol{a}$ is the magnetic vector potential of the nodal values, and $\boldsymbol{F}$ is the source term constitute by the supply current density $\boldsymbol{J}$ and the magnetization current density $\boldsymbol{J_M}$.

The entry of stiffness matrix $\boldsymbol{S}$ in the integral form can be written as

$$\boldsymbol{S}_{ij} = \int \nu \nabla N_i . \nabla N_j dS \qquad \text{where} \quad i, j = 1.....n \tag{41}$$

In case of homogeneous Neumann boundary condition $\frac{\partial A}{\partial n} = 0$, the integral form of the source term $\boldsymbol{F}$ can be written as

$$\boldsymbol{F}_i = \int N_i J dS \qquad \text{where} \quad i = 1.....n \tag{42}$$

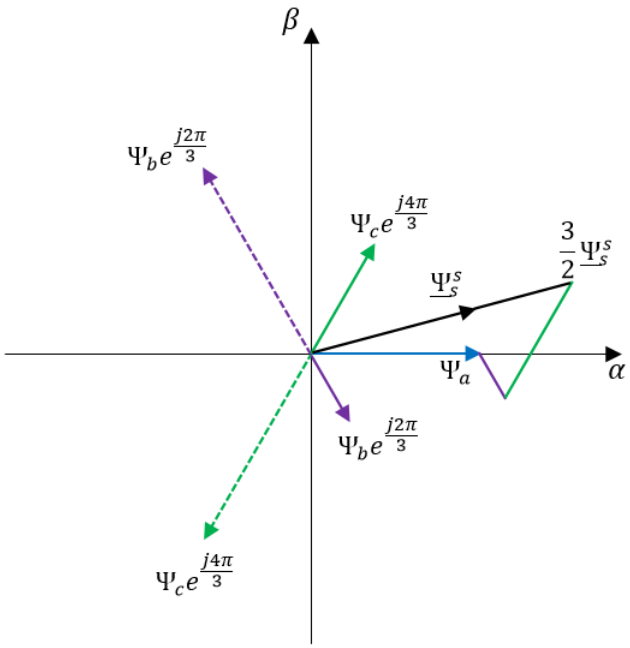


Figure 17: Space vector representation of the stator flux linkages.

In case of inhomogeneous Neumann boundary condition $\frac{\partial A}{\partial n} = g$, due to the boundary integral, one additional term can be added to the integral form of the source term $\boldsymbol{F}$, which transform Equation 42 as

$$\boldsymbol{F}_i = \int N_i J dS + \int_\Gamma N_i \nu g d\Gamma \tag{43}$$

where $\nu$ is the reluctivity of material. Now, the nodal values of magnetic vector potential $\boldsymbol{a}$ can be directly solved from the matrix Equation 40. The fast computation and fewer parameter requirements of the space vector model make it a preferable choice for the analytical analysis of electrical machines, precisely the synchronous machine. Thus, the calculation of flux linkage can be achieved through a space vector model where the three-phase flux linkages can be transformed into an equivalent two-phase system in the stationary $\alpha\beta$ frame which is illustrated in Figure 17.

These axes $\alpha$ and $\beta$ are perpendicular to each other and can be considered as the real and imaginary part of the two-axis system, which allows a complex representation of the space vector model. The transformation of three-phase to two-phase can be done by using Clark's transformation, also known as $\alpha\beta$ transformation.

$$\underline{\boldsymbol{\Psi}}_s^s(t) = \Psi_\alpha(t) + j\,\Psi_\beta(t) = \frac{2}{3} V^k \left( \Psi_\mathrm{a}(t) e^0 + \Psi_\mathrm{b}(t) e^{\frac{j2\pi}{3}} + \Psi_\mathrm{c}(t) e^{\frac{j4\pi}{3}} \right) \tag{44}$$

where the underscore presents the complex quantity, the subscript and superscript $s$ are used to indicate that the space vector is formed with the stator quantities and expressed in the stator reference coordinates $\alpha\beta$, respectively. The contribution of flux linkages can be outfitted from their particular directions which is indicated

by the corresponding unit vector (1,$j2\pi/3$, $j4\pi/3$), then combined all together and scaled with the space vector scaling constant $V^k$. The scaling constant can be formed as a matrix for each phase quantities where superscript $k$ denotes the phase number ($a$, $b$ or $c$), respectively. The same approach can be implied to transform the other three-phase stator quantities such as current and voltage where the space vector model rotates with the same angular frequency of the stator quantities, i.e., usually the fundamental frequency $\omega$ (Harnefors et al., 2015).

In a magneto-static solution, the induced current or voltage is neglected, and the computed fluxes are independent of time, i.e., static.

Belahcen et al. (2016) showed a systematic approach to compute the stator flux linkages from the obtained static FE solution and coupling with the space vector voltage equation of a synchronous machine. According to Belahcen et al. (2016), the calculation of flux linkage can be achieved by forming $V_i^k$ from the static FE solution. The space vector scaling constant $V_i^k$ for each phase can be formed from the position of the elements in each phase indicated by introducing a flag $\beta^k$ and the shape functions $N_i$ of $i^{th}$ nodes and integrated over the problem domain as follows

$$V_i^k = \frac{Wl \int\limits_{\boldsymbol{\Omega}} \boldsymbol{\beta}^k N_i d\boldsymbol{\Omega}}{\frac{1}{2} \int\limits_{\boldsymbol{\Omega}} \mid \boldsymbol{\beta}^k \mid d\boldsymbol{\Omega}} \tag{45}$$

where $W$ stands for the number of turns in the stator coils, $l$ is the effective length of the machine, $k$ is the phase number ($a$, $b$ or $c$) and $\beta^k$ is a flag that indicates the positions of the elements in coil side. The flag $\beta^k$=0 shows no elements in a coil, $\beta^k$=1 elements in the positive side of the coil and $\beta^k$=-1 elements in the negative side of the coil of phase $k$. Finally, the flux linkages for each phase can be obtained by forming the matrix or vector $\boldsymbol{V}^k$ and multiplying with the magnetic vector potential $\boldsymbol{A}$ from the computed static FE solution in Equation 40 as follows

$$\begin{aligned} \Psi_{\mathrm{a}} &= \boldsymbol{V}^{\mathrm{aT}} \boldsymbol{A} e^{0} \\ \Psi_{\mathrm{b}} &= \boldsymbol{V}^{\mathrm{bT}} \boldsymbol{A} e^{\frac{j2\pi}{3}} \\ \Psi_{\mathrm{c}} &= \boldsymbol{V}^{\mathrm{cT}} \boldsymbol{A} e^{\frac{j4\pi}{3}} \end{aligned} \tag{46}$$

The resultant flux linkage can be computed as a sum of three stator phases ( $\Psi_{\mathrm{a}}$, $\Psi_{\mathrm{b}}$ and $\Psi_{\mathrm{c}}$) flux linkage as follows

$$\boldsymbol{\Psi} = \frac{2}{3}((\boldsymbol{V}^{\mathrm{aT}} \boldsymbol{A})e^{0} + (\boldsymbol{V}^{\mathrm{bT}} \boldsymbol{A})e^{\frac{j2\pi}{3}} + (\boldsymbol{V}^{\mathrm{cT}} \boldsymbol{A})e^{\frac{j4\pi}{3}}) \tag{47}$$

where superscript T denotes, the matrix or vector transposition and $j$ is the imaginary unit vector indicates the direction of the flux linkages. The formed matrix or vector $\boldsymbol{V}^k$ is used to evaluate the source term constitutes from the supply current in Equation 40 by scaling inversely of the machine length. However, the contribution to the source term $\boldsymbol{F}$ in Equation 40 from the magnetizing current generates by the magnet is handled individually with a standard procedure.

When the machine is fed from the current source, the field equations can be solved simply and directly by assuming the uniform current distribution in the

windings. However, the non-uniform current distribution due to the skin effect and the proximity effect is neglected in this case. Therefore, the approximate solution can be achieved without coupling the field and the circuit equation. On the other hand, the situation is different, when the machine is fed from a voltage source as the computation of current depends on the field equation and the circuit equation. Thus, the coupling of the field equation and the circuit equation is essential for the correct computation of the current and other quantities such as torque or iron losses if the machine is supplied from the voltage source.

The space vector equivalent circuit of a synchronous machine in stator coordinates is illustrated in Figure 18.

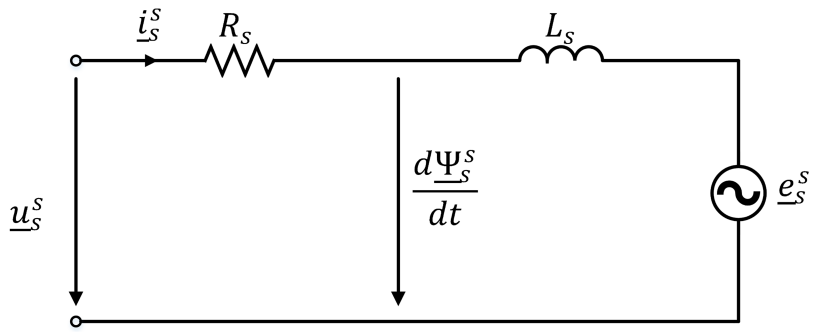


Figure 18: Space vector equivalent circuit of a synchronous machine.

In the stator reference frame, the space vector voltage equation of a synchronous machine can be written as

$$\underline{\boldsymbol{u}}_s^s = \underline{\boldsymbol{i}}_s^s R_s + \frac{\partial \underline{\boldsymbol{\Psi}}_s^s}{\partial t} \tag{48}$$

where $R_s$ is the stator resistance, $\boldsymbol{u}_s$, $\boldsymbol{i}_s$, and $\boldsymbol{\Psi}_s$ denotes the stator voltage, current, and flux linkages, respectively, where the underscore indicates that these are the complex variables. The subscript and superscript $s$ refers that these are the stator variables and expressed in the stator reference coordinate. In general, the complex variables in Equation 48 can be expressed in component form by projecting the vector in $\alpha\beta$ complex plan. However, the Finite Element Method (FE) generates the output natively in $(x, y)$ coordinates; thus, the complex variables in Equation 48 can also be presented as $x$ and $y$ component in case of a static FE solution as follows

$$\begin{aligned} \underline{\boldsymbol{u}}_s^s &= u_x + j u_y \\ \underline{\boldsymbol{i}}_s^s &= i_x + j i_y \\ \underline{\boldsymbol{\Psi}}_s^s &= \Psi_x + j\,\Psi_y \end{aligned} \tag{49}$$

Besides, the flux distribution is assumed to be sinusoidal time variation, and any additional flux linkages from the end winding can be represented by an end winding inductance $L_{ew}$. Introducing the end winding inductance $L_{ew}$ in Equation 48 and expressing the stator voltage in $x$ and $y$ components lead to:

$$\begin{aligned} u_x &= i_x R_s - \omega L_{ew} i_y - \omega\,\Psi_y \\ u_y &= i_y R_s + \omega L_{ew} i_x + \omega\,\Psi_x \end{aligned} \tag{50}$$

where $\omega$ stands for the flux pulsating angular frequency for static simulation in steady-state and also referred to as fundamental supply frequency. In the Finite Element approach, the flux can be directly computed from Equation 47 and for the current fed machine the voltage can be calculated from the Equation 50 using the calculated flux linkages. However, if the machine is fed from a voltage source, then the flux Equation 47 and the voltage Equation 50 needs to be solved within the same FE solution to determine the current. The coupling of static flux and space vector equation can be achieved by inserting the flux Equation 47 in the space vector voltage Equation 50, then the static FE solution Equation 40 and the space vector Equation 50 are transformed into a single equation:

$$\begin{bmatrix} \boldsymbol{S} & -\frac{\boldsymbol{V}}{l} \\ \omega\, \boldsymbol{V}^{\mathrm{T}} & \boldsymbol{Z} \end{bmatrix} \begin{bmatrix} \boldsymbol{A} \\ \boldsymbol{i} \end{bmatrix} = \begin{bmatrix} \boldsymbol{F}_{pm} \\ \boldsymbol{u} \end{bmatrix} \tag{51}$$

where $\boldsymbol{Z}$ is the $2 \times 2$ matrix that contains the stator resistance and the end winding inductance appears from the Equation 50, and the matrix $\boldsymbol{V}$ is now constructed by the projections of $\boldsymbol{V}^k$ from the Equation 45 over the $(x, y)$ plane. Now, Equation 51 turns into a systematic approach for obtaining the nodal values of magnetic vector potential $\boldsymbol{a}$ in case of a voltage fed machine. It is noticeable that such coupling approach is only possible if the flux distribution is assumed to be sinusoidal variation with time. The static simulation can provide relatively good accuracy, i.e., close to the steady-state within a very short simulation time and substitute the time-stepping method for many tasks.

## 3.4 Time Dependence of Flux Density in Static Analysis

The existence of the harmonic components in the electrical machine affects the flux density waveform and influence to depend on time. However, the obtained flux density $\boldsymbol{B}$ values from a static field solution is independent of time, i.e., static. Thus, the time dependence of the static flux density waveform needs to be introduced in the iron loss computation. In FCSMEK, the stator FE mesh is constructed by multiplying the slot pitch mesh. Thus, the number of elements in one slot pitch mesh is repeated to the next slot pitches, and elements from one slot pitch to another has the same position and size. Therefore, the space variation of the static flux density waveform over one period can be achieved by selecting the elements at one slot pitch interval. It can be noted that the elements in stator yoke can be chosen even at half of the slot pitch to complete the one period of flux density waveform. However, the situation is different for the stator teeth where the elements can be selected after one slot pitch due to the existence of stator slots. In actual iron loss computation, the flux density waveform over one period is created by varying one slot pitch both for the stator yoke and teeth. The time dependence of the flux density waveform can be achieved by assuming that the flux density waveform is moving with the fundamental angular frequency $\omega$ and time $t$. Therefore, at any instant of angular distance, $\theta$ and time $t$, the displacement of the moving flux density with initial position $\theta_o$ can be determined as $\theta = \theta_o + \omega t$. With respect to the initial position $\theta_o$ and time $t = 0$,

the displacement of the flux density waveform can be written as

$$\boldsymbol{B}(\theta, r, t) = \boldsymbol{R}\boldsymbol{B}(\theta - \omega t, r, 0) \tag{52}$$

where $\theta$ is the angular position from the rotor midpoint to the node, $r$ is the radial distance from the rotor midpoint to the node, and $\boldsymbol{R}$ is the rotation matrix. The entry of the rotation matrix $\boldsymbol{R}$ in Equation 52 can be expressed as

$$\boldsymbol{R} = \begin{bmatrix} \cos\theta & -\sin\theta \\ \sin\theta & \cos\theta \end{bmatrix} \tag{53}$$

It can be noted that the radial distance $r$ from the rotor midpoint in Equation 52 is satisfied automatically as the elements are taken in the same radial distance. Now, the solution of flux density waveforms from elements to elements is independent of time with respect to the initial position $\theta_o$ and time $t_o$. The discretize time step can be used to introduce the time dependence through indexing the node numbers where total discretize time steps should be equal to the number of slot pitches. The nodal positions of next slot pitches mesh moves to the initial slot pitch mesh position successively at each discretize time step. It is possible as the angular distance, i.e., slot pitch of any particular element from one slot pitch mesh to another is proportional to the time which can be seen in Equation 63. It is worth noticing that, such an approach can be only applicable where the repetitive sequence of the slot mesh is found. Therefore, a complete cycle of flux density waveform can be created element by element just rotation over one slot pitch. The time dependence of the nodal values $\boldsymbol{a}$ and the solution procedure in case of dynamic field solution is described in the following section.

## 3.5 Dynamic Field Solution

The solution of the magneto-static problem is achieved by assuming sinusoidal time variation of the source quantities which relax the time dependence of the magnetic field as described in Section 3.3. Moreover, the magnetic vector potential $\boldsymbol{A}$ is computed as a single component vector potential in magneto-static case. However, in practice, the magnetic core in the electrical machine are experienced to a non-sinusoidal field distribution even if the sinusoidal variation of the source is assumed due to the presence of harmonic components. Thus, the magnetic field depends on the time, as shown in Equations 22, and 26. The time dependence magnetic field introduces the time-varying eddy current in the system. Therefore, the magnetic vector potential in the magneto-static Equation 31 turns into a time-dependent equation:

$$\nabla.(v\nabla\boldsymbol{A}) + \sigma\frac{\partial\boldsymbol{A}}{\partial t} = -\boldsymbol{J} \tag{54}$$

where $\sigma$ is the conductivity of the material. Equation 54 can be solved by discretizing in space, and using a Finite Element scheme where the nodal values of magnetic vector potential $\boldsymbol{A}$ in each element are approximated using the Galerkin's residual

method and the shape functions of the nodes and turns into a simple linear algebraic equation:

$$\boldsymbol{S}\boldsymbol{a} + \boldsymbol{T}\dot{\boldsymbol{a}} = \boldsymbol{F} \tag{55}$$

Where the magnetic vector potential $\dot{\boldsymbol{a}}$ depends on the time, and the derivative of $\dot{\boldsymbol{a}}$ can be written as

$$\dot{\boldsymbol{a}} = \frac{d\boldsymbol{a}}{dt} \tag{56}$$

The entries of the stiffness matrix $\boldsymbol{S}$ and the source term $\boldsymbol{F}$ in matrix Equation 55 is described in Section 3.3 where the entries of the boundary term $\boldsymbol{T}$ can be determined as

$$\boldsymbol{T}_{ij} = \int_{\Omega} \sigma N_i N_j d\Omega \qquad i, j = 1, ..., n \tag{57}$$

It can be noted that $\boldsymbol{T}_{ij}$ is the boundary integral at the material boundary and the $i, j$ are nodes active in material boundary and $N_i, N_j$ are the corresponding shape functions of these active nodes. To evaluate the time dependency of the magnetic field, the nodal values of the magnetic vector potential $\boldsymbol{a}$ needs to be solved at each time step. The magnetic vector potential at each time step can be approximated by using the Crank-Nicolson time-stepping method where $k$ and $k+1$ determine the time step:

$$\boldsymbol{a}^{k+1} = \boldsymbol{a}^{k} + \frac{1}{2}[\frac{\partial \boldsymbol{a}}{\partial t} \mid^{k+1} + \frac{\partial \boldsymbol{a}}{\partial t} \mid^{k}]\Delta t \tag{58}$$

If the true time dependency of the field equations is needed in the non-linear system, the field equations must be solved step by step method evaluating the variations of the field in short time intervals $\Delta t$. The rotor rotates in each short time interval $\Delta t$ with an angle related to the rotor angular velocity. The actual rotor motion is accomplished by modifying the air gap mesh in each step concerning the angular speed of the machine. Circuit equations and field equations are coupled to couple the magnetic vector potentials, voltages, and currents in stator and rotor. The non-linearity of the system equations is solved using the Newton-Rapson iteration method in the same iteration loop for rapid convergence and short time solution (Arkkio, 1987).

## 3.6 Numerical Integration

The numerical integration is needed to solve the stiffness matrix Equation 41, source term Equation 42 and compute the flux density values in each element from the nodal values of magnetic vector potential $\boldsymbol{A}$. Thus, an integration method can be chosen for faster computation which can provide better accuracy with a minimum number of integration points. The Gaussian quadrature method is recognized for the requirements of least number integration points; therefore, this method is used to approximate the solution of numerical integration. The integration points, coordinates and the related weight functions are selected for the polynomial passing through the function, so that, it can be appropriately integrated.

In FEM, the numerical approximation of the function $f$ can be achieved as a summation of integration points over the triangular element and the multiplication of the coordinates and the weight function of each integration points. In this thesis, the second-order triangular element having six nodes is used; thus, the quadratic polynomial shape function is chosen. Three integration points are recommended and chosen for each quadratic triangular element. It can be noted that increasing the integration points does not necessarily raise the solution accuracy. In two dimensional case, the solution of the numerical integration can be achieved by performing the following integration formula successively

$$\int_{-1}^{1}\int_{-1}^{1} f(u,v)dudv = \sum_{j=1}^{m}\sum_{i=1}^{m} w_i w_j f(u_i, v_j) \tag{59}$$

where $m$ is the number of integration points, $u_i$ and $v_j$ refers to the coordinates and the $w_i$, $w_j$ represents the weight functions of the integration point $i$ and $j$, respectively. It can be noted that the integration of the function $f$ is defined in the local coordinate $(u, v)$. Thus, the nodal values of magnetic vector potential $\boldsymbol{a}$ in the integration points of each iron element is calculated in the actual coordinates $(u, v)$. The coordinate transformation from local coordinates $(u, v)$ to the global coordinate $(x, y)$ is done multiplying by the determinant $\mid J(u,v) \mid$ of the Jacobian matrix

$$\int_{\Omega} f(x,y)d\Omega = \int_{-1}^{1}\int_{-1}^{1} f(u,v) \mid J(u,v) \mid dudv = \sum_{j=1}^{m}\sum_{i=1}^{m} w_i w_j f(u_i, v_j) \mid J(u_i, v_j) \mid \tag{60}$$

where the entry of the determinant$\mid J(u,v) \mid$ of the Jacobian matrix is obtained by

$$\mid J(u,v) \mid = \begin{bmatrix} \frac{\partial x}{\partial u} & \frac{\partial y}{\partial u} \\ \frac{\partial x}{\partial v} & \frac{\partial y}{\partial v} \end{bmatrix} = \frac{\partial x}{\partial u}\frac{\partial y}{\partial v} - \frac{\partial y}{\partial u}\frac{\partial x}{\partial v} = 2\Delta \tag{61}$$

The determinant of the Jacobian matrix $\mid J(u,v) \mid$ is twice the surface area $\Delta$ of the triangular element. The Fourier components of the flux density values $\boldsymbol{B}_x$, and $\boldsymbol{B}_y$ of each integration points are computed from the partial derivative of the nodal values of magnetic vector potential $\boldsymbol{a}$ with respect to $x$-$y$ coordinates as shown in Equations 67, and 68 and multiplied by the Fourier coefficients of the nodal values $\boldsymbol{a}$. It can be noted that the obtained flux density components $\boldsymbol{B}_x$ and $\boldsymbol{B}_y$ have consisted with the cosine and sine terms as the Fourier coefficients are complex-valued; hence, the magnitude of the flux density values $\boldsymbol{B}$ is computed.

## 3.7 Iron Loss Computation from a Static Field Solution

The iron loss computation process from a static field solution is started with meshing the machine geometry using the MESH program in FCSMEK. FCSMEK has an option to mesh the geometry using the linear, quadratic or cubic polynomials. In this thesis, the meshing is done by using the quadratic polynomials. The criteria of meshing in the Finite Element method is described in Section 3.1.2. The index

numbers are assigned to each element of the slot pitch mesh. Similarly, the nodes of each element have also their own index numbers. The slot pitch mesh consisted of different materials; therefore, the material index number and boundary node are assigned to the corresponding element, and the boundary condition is applied to periodic ones. The machine geometry and the material indices are stored in the *cim.data* file, which is taken as an input for running the MESH program. When the meshing is completed, the related information about the FE mesh such as element numbers, node numbers, material indices and coordinates of the nodes are stored in the *cim.fedat* file. After that, the static FE analysis program SYDC is started to run where the output of the MESH program is taken as an input. The computed nodal values of magnetic vector potential $\boldsymbol{a}$ are static and stored in the *cim.fedat* file along with the Finite Element (FE) mesh information. A complete cycle of flux density waveform for element to element in the stator core can be achieved varying the angular position by one slot pitch from a single static simulation over two pole pitches. The slot pitch of the preferred machine can be calculated as

$$\theta_s = \frac{2\pi}{Q_s} = 0.0698 \quad (radian) \tag{62}$$

where $Q_s$ denotes the total number of stator slots, and the selected machine has a total of 90 stator slots. In actual implementation, the time dependence of the nodal values of magnetic vector potential $\boldsymbol{a}$ is introduced and used to compute the flux density values later. The time step for the time dependence is computed as follows

$$\Delta t = \frac{\Delta\theta_s p}{\omega} = 6.6667 \times 10^{-4} s \tag{63}$$

where $p$ denotes the number of pole pairs which is three for this particular machine, $\theta_s$ is the slot pitch, and $\omega$ is the supply angular frequency.

### 3.7.1 Computation Algorithm

The computation began with taking the elements and nodes belongs to one slot pitch mesh from where the repetitive sequence is started. FORTRAN programming language is used for computation as the FCSMEK is developed in FORTRAN environment. An array is formed containing all the element numbers belongs to the iron elements using the material indices for one slot pitch mesh. If the element number is known, the algorithm can search and find out the nodes and corresponding nodal values of the magnetic vector potential $\boldsymbol{a}$ belong to that particular element. To emulate with the time step, the sequence of index number from elements to elements or nodes to nodes is needed at each slot pitch. The time discretization of nodal values is done through indexing the node numbers where the position of nodal points of one slot pitch mesh moves to the initial slot pitch mesh position continuously in each time step. The solution region provides half-cycle of the magnetic vector potential $\boldsymbol{a}$ waveform , consequently, the flux density $\boldsymbol{B}$ waveform. Another half-cycle waveform is achieved by mirroring the existing solution region. A problem was identified during the computation as the elements in the first slot pitch is not equal as the other slot

pitch meshes, i.e., if the elements are taken from the beginning of the mesh. However, the actual iron loss calculation required an equal number of elements in every slot pitch mesh. So that, after one slot pitch distance the same size element can be found in other slot pitch mesh, which is required to form the elements to elements flux density waveform over one period. Any asymmetrical slot pitch mesh can be given the erroneous result; thus, the calculation is continued without taking this slot pitch mesh. The elements of the initial slot pitch are assumed from the next slot pitch mesh, i.e., second slot pitch. Thus, a total of 29 slot pitch meshes are considered for two-pole pitches instead of 30 slot pitch meshes. The flux density waveform for a complete cycle is required to discretize time steps equivalent to the total number of slot pitches, i.e., 30 slot pitches for this particular machine in two-pole pitches. A loop is performed equal to the discretize time steps to introduce the time dependence of the nodal values. The time step between the elements in the last slot pitch of the solution region and the first slot pitch of the mirroring region is kept twice of the others due to avoid one slot pitch mesh in between them and fulfil the complete cycle.

The Fourier coefficients of the obtained magnetic vector potential values as a function of time $\boldsymbol{a}(t)$ is computed over one period. The numerical approximation is required to achieve the solution of Fourier coefficients. Due to simplicity and relatively good accuracy, the Trapezoidal method is used to approximate numerical integration. In the Trapezoidal method, the numerical integration over one interval period is approximated by dividing the integration area into trapezoids which turns into the simple computation. The Trapezoidal method works in two different ways for the even and uneven spacing of the points. For uneven step size, the numerical integration with $N+1$ non-uniform spaced points can be approximated by the following method:

$$\int_0^T \boldsymbol{a}(t)dt \approx \frac{1}{2}\sum_{n=1}^{N}(t_{n+1}-t_n)[\boldsymbol{a}(t_n)+\boldsymbol{a}(t_{n+1})] \tag{64}$$

where $(t_{n+1}-t_n)$ determines the spacing between each successive pair of points. It can be noted that the approximation accuracy of the Trapezoidal method depends on the partition number $N$. As $N$ becomes larger, i.e., partition interval length $\Delta t_n$ becomes smaller, the error of the Trapezoidal method is reduced by $(1/N^2)$.

The Nyquist-Shannon sampling theorem works perfectly for samples that are evenly spaced in time, and no information is lost from the signal. It is mentioned already that the obtained magnetic vector potential $\boldsymbol{A}$ waveform are non-uniformly spaced in time. The signal from the unevenly spaced samples can be reconstructed as accurately as possible if the average sampling rate follows the Nyquist rule, but the signal might lose one or two samples. According to the Nyquist theorem, the suitable number of harmonic components considered from a sampled waveform can be determined as

$$n = \frac{T_s}{2dt} = \frac{0.01s}{2 \times 6.6667 \times 10^{-}4s} \approx 7 \tag{65}$$

where $n$ denotes the number of harmonic components, $T_s$ is the sampling time period and $dt$ is the time step. Due to the non-uniform sampling step size, the lower harmonic components, i.e., up to $5^{th}$ harmonic components, are chosen in the loss computation. However, the $6^{th}$ harmonic component is not included as all the even harmonic components are zero due to the symmetrical waveform of the flux density. The effect of including the $7^{th}$ harmonic components in signal reconstruction from the sampled signal is shown later. The accuracy of iron loss computation largely depends on the accurate prediction of the flux density values. The iron loss is computed from the peak flux density values at each harmonic frequency components for one interval period. In FEM, the flux density can be computed from the divergence of nodal values of the magnetic vector potential $\boldsymbol{a}$ as shown in Equation 29. In the 2D analysis, the flux density can be determined only in the $x$-$y$ plane and does not depend on the $z$ axis. The magnetic flux density lies in the $x$-$y$ plane as

$$\boldsymbol{B} = iB_x + jB_y \tag{66}$$

where $B_x$ is the flux density values in the $x$-direction and $B_y$ is the flux density values in the $y$-direction. According to the Equation 29, the flux density $B_x$ and $B_y$ can be calculated from the partial derivation of magnetic vector potential values $\boldsymbol{A}$ with respect to the $x$-$y$ coordinates as follows

$$B_x = \frac{\partial \boldsymbol{A}}{\partial y} \tag{67}$$

$$B_y = -\frac{\partial \boldsymbol{A}}{\partial x} \tag{68}$$

The requirements of numerical integration for iron loss calculation and the flux density computation at each integration points of the iron elements are described in Section 3.6. The hysteresis and eddy current losses are computed from the obtained flux density values at each harmonic components and integrating over the volume of the machine by using Equations 16, and 17, respectively. The total iron loss is calculated as a sum of the hysteresis and eddy current loss components. It can be noted that the excess loss components are included in the eddy current loss.

## 3.8 Iron Loss Computation from a Dynamic Field Solution

In FCSMEK, the iron loss is calculated from the dynamic field solution in CIMTD routine. The simulation is started with the same input parameters given for the static analysis. The FE analysis information computed from the static field solution and written on *cim.fedat* file is taken as an initial stage of the time-stepping simulation, which assists in reaching the steady-state condition within a few simulation periods. In a dynamic solution, the rotor rotates in each time step, and the flux density profile is varied depending on the rotor position. Therefore, the time dependence of flux density distribution is taken into account in the dynamic loss calculation method. In FCSMEK, the procedure of assigning the element and node numbers and the corresponding material index numbers are already discussed in Section 3.7. To

compute the iron loss in CIMTD, a loop is used to call all the elements that belong to the iron material based on their material index number. A separate loop is used to obtain the nodal values of magnetic vector potential $\boldsymbol{a}$ at each node of iron elements. The simulation is run for a few periods in order to obtain steady-state characteristics. However, the Fourier analysis of the nodal values of the magnetic vector potential $\boldsymbol{a}$ is started during the last period. The Fourier coefficients of the nodal values are computed at each time step. The numerical integration associated with Fourier coefficients are solved, and the sampling is done according to the Nyquist rule. The procedure of flux density computation at each integration points and the Fourier decomposition of the flux density waveform from the Fourier coefficients of the nodal values $\boldsymbol{a}$ is explained in Section 3.6.

Finally, the average iron loss is computed from the Fourier decomposition of flux density values over one period and integrating over the volume of the machine using the same loss Equations 16, and 17 in the post-processing stage. It is worth noticing that, the total iron loss is computed in the time-stepping method as a contribution of the stator core loss and the rotor core loss. In static loss computation, only the stator core loss is calculated as the rotor has the DC magnetic field. Thus, the total iron loss is segregated into the stator, and rotor iron loss and only the stator core loss is taken into consideration in the time-stepping method for a fair comparison.

## 3.9 Chapter Summary

A set of electromagnetic equations and the solution process using the 2D Finite Element Method is discussed in Section 3.1. A basic introduction of the FEM solver software FCSMEK for simulating the synchronous machine is given in Section 3.2. The strategy of two-dimensional static field computation in FEM and the iron loss calculation techniques from this field solution are described in Section 3.7. Section 3.8 deals with the dynamic field computation method and the procedure of iron loss computation from this solution. The outcomes and findings of the conductive thesis are presented in the following Chapter.

# 4 Results and Discussion

This chapter is dealing with the application, analysis and comparison of different parameters involved with the iron loss calculation and the computation results using the proposed method and the time-stepping method. Section 4.1 introduces the model application in a synchronous machine, machine specifications, basic machine parameters required for the simulation, and some parameters obtained from the simulation for both methods in FCSMEK. Section 4.2 presents the comparison of some obtained results associated with the iron loss computation and the total stator iron loss computed from the static field solution and the dynamic field solution.

## 4.1 Model Application in Synchronous Machine

The developed model is applied to a salient pole synchronous machine, which consists of 90 stator slots and six-rotor poles. The machine has a double layer distributed stator winding. The machine has the field winding stated in the rotor pole to produce enough constant flux required for the magnetization. Moreover, the machine contains damper windings which are mounted on the rotor pole body. The application of the damper winding is to assist on the synchronous machine starting mechanism, preventing the hunting effect due to the sudden load change. Furthermore, the damping bar minimizes the harmonics of the air gap flux density during the transient state. The conductivity of the stator core material was kept to 0 $S/m$. The initial material conductivity of stator windings and the damper windings was set to $58.1 \times 10^6$ $S/m$ at ambient temperature, i.e., $20^oC$ and adjustable to the user-defined temperature during the simulation. The cross-section of the chosen machine is depicted in Figure 19.

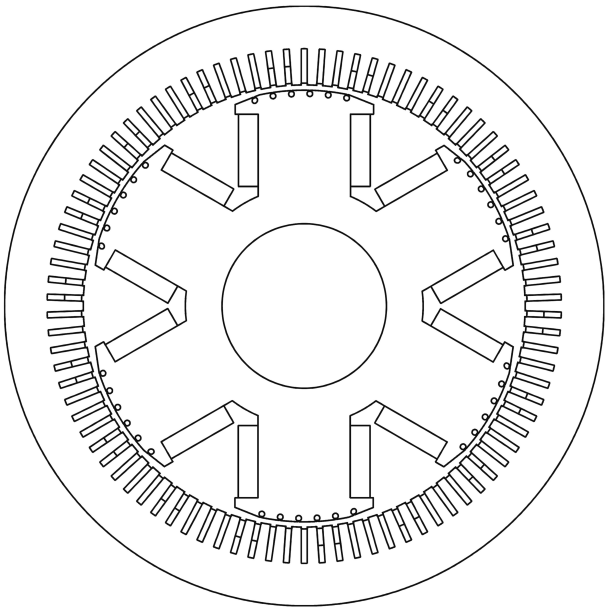

Figure 19: Cross-section of the salient pole synchronous machine.

A 2D FE mesh of the selected machine was generated through the MESH program in FCSMEK. Most commonly, the first order, second order or third order triangular element is used in 2D FEM analysis. In this thesis, the second-order triangular element having six nodes has been chosen by trading off between the computation time and accuracy. The mesh of the entire machine is illustrated in Figure 20, which is produced by multiplying the mesh of the smallest symmetry sector. The FE mesh of the smallest symmetry section is shown in Figure 21, which is used in the simulation. The mesh consists of a total of 2026 elements and 4113 nodes in the solution region. Besides that, each stator slot pitch has a total number of 54 elements among them 30 elements in the iron core, 18 elements in the air and six elements in the stator winding. A changeable air-gap mesh is used to take the rotor motion into account. The information about the elements and nodes of the studied synchronous machine is listed in Table 5.

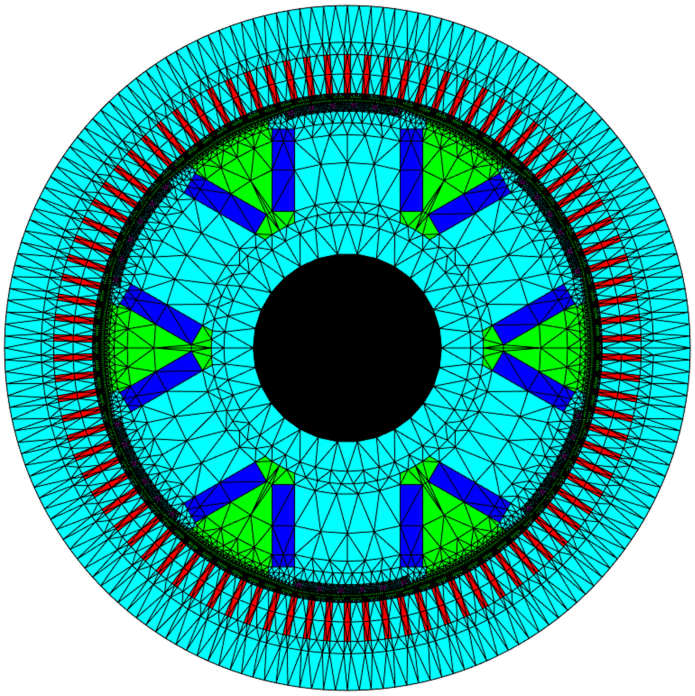

Figure 20: Finite element mesh of the salient pole synchronous machine.

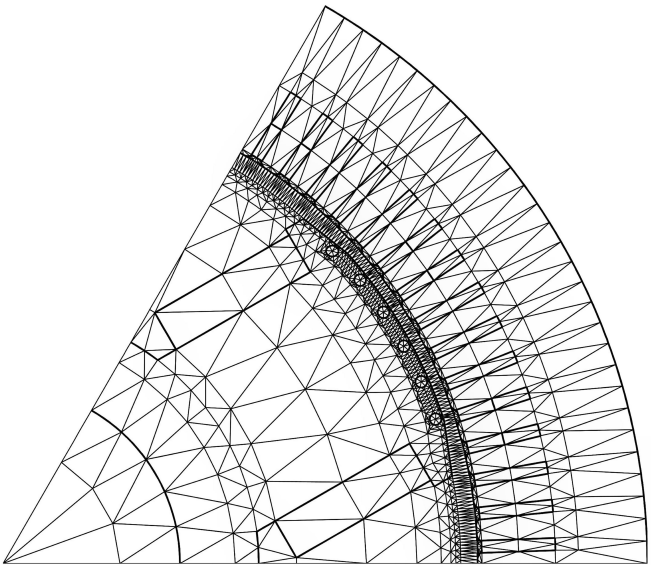

Figure 21: Finite element mesh of the smallest symmetry section.

Table 5: Mesh results.

| **Parameter** | **Number** |
|---|---|
| Order of triangular element | 2 |
| Nodes per triangular element | 6 |
| Number of elements | 2026 |
| Number of nodes | 4113 |
| Elements in each stator slot pitch | 54 |
| Elements in iron core per stator slot pitch | 30 |
| Elements in air per stator slot pitch | 18 |
| Elements in winding per stator slot pitch | 6 |

The operating characteristics and the solution of static FE analysis were obtained by simulating the synchronous machine using the SYDC routine. To run the SYDC program, some parameters such as supply source, the connection of the stator and rotor windings, temperature of the stator and rotor, terminal voltage or current, rotor angle and the field winding voltage or current are required from the user side. The selected machine has a three-phase, star connection with a supply frequency of 50 Hz. The machine was supplied from a voltage source, and the current was computed by coupling the field equations and the circuit equations within the same FE solution as described in Section 3.3. The machine was simulated at a specific operating point using the input parameters, which are tabulated in Table 6. The rotor field winding voltage and the rotor angle required for this operating point was computed through an algorithm developed by Electromechanics group at Aalto University. However, if the machine is fed from the current source, then the rotor field current and the

rotor angle need to be searched for the desired operating condition. The machine parameters obtained using the SYDC routine are illustrated in Table 6.

After that, the time-stepping simulation was continued with the same parameters used in the SYDC routine. The simulation was carried out for 300 steps per period and four periods were studied to obtain the steady-state operating characteristics and the solution of dynamic FE analysis using the CIMTD routine. The short step size was used for better accuracy, which may increase the computation time slightly; thus, the user needs to compromise between the accuracy and the computation cost. The time was discretized into short time interval using the Crank-Nicholson time-stepping method. The field and the circuit equations were solved for each successive time intervals. The rotor was rotated at a constant speed, and the actual rotor motion was achieved by changing the FE mesh in the air-gap. The non-linearity of the system equations was solved by the Newton-Raphson iteration method. The operating parameters acquired using the CIMTD routine is tabulated in Table 7.

Table 6: Parameters using SYDC routine.

| **Parameters** | **Data** |
|---|---|
| Supply frequency [Hz] | 50 |
| Terminal voltage [V] | 3150 |
| Terminal current [A] | 2274 |
| Rotation speed [RPM] | 1000 |
| Rotor angle [Elec.Deg.] | 31.9 |
| Apparent power [MVA] | 12.410 |
| Active power [MW] | 12.407 |
| Reactive power[kVAR] | -258.7 |
| Shaft power [MW] | 12.6 |
| Air-gap torque [kNm] | 121.2 |
| Power factor [Capacitive] | 0.9998 |
| Stator winding temperature [°C] | 50 |
| Rotor winding temperature [°C] | 50 |
| Rotor voltage [V] | 58 |
| Rotor current [A] | 371.1 |

Table 7: Parameters using CIMTD routine.

| **Parameters** | **Data** |
|---|---|
| Supply frequency [Hz] | 50 |
| Terminal voltage [V] | 3150 |
| Terminal current [A] | 2285 |
| Rotation speed [RPM] | 1000 |
| Shaft power [MW] | 12.42 |
| Air-gap torque [kNm] | 118.61 |
| Power factor [Capacitive] | 0.9997 |
| Stator winding temperature [°C] | 50 |
| Rotor winding temperature [°C] | 50 |

It can be seen that the operating parameters obtained from the SYDC and the CIMTD routines are in relatively good agreement. Some of the parameters such as the terminal current, air-gap torque and shaft power were computed by SYDC slightly differ than the time-stepping simulation. This is because the steady-state parameters are obtained in CIMTD while the parameters calculated in SYDC at the initial state of analysis based on the two-axis model by assuming the steady-state condition; therefore, the computation may overestimate these parameters slightly.

## 4.2 Iron Loss Comparison

The flux contour lines and the flux density distribution both for the static analysis and dynamic analysis of the smallest symmetry section are shown in Figures 22, and Figure 23. It can be seen that there is no difference in the flux density distribution; thus, the exact computation of flux density is expected for both methods. In stator core, the flux density distribution is higher in the teeth than the yoke where the fluxes are penetrating to the air gap. The highest flux density distribution is observed in the rotor pole near pole face where the fluxes are transferring from the stator as the rotor field drags the stator field.

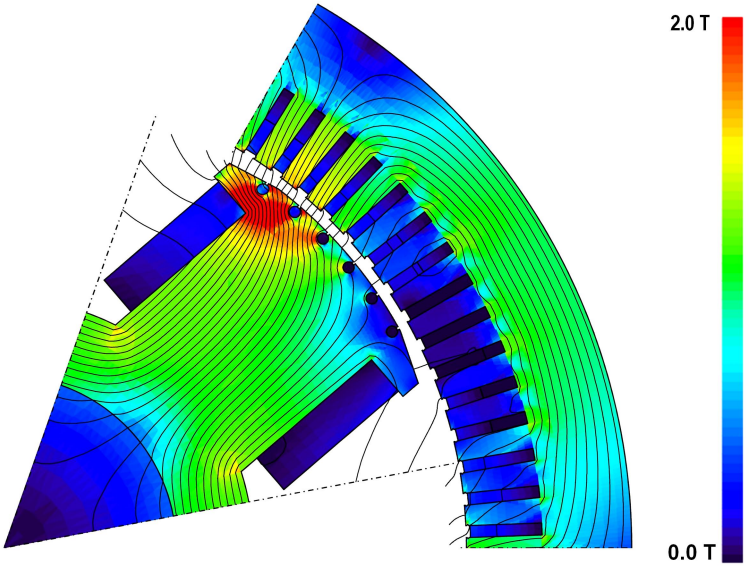


Figure 22: Flux density distribution of the smallest symmetry section in SYDC.

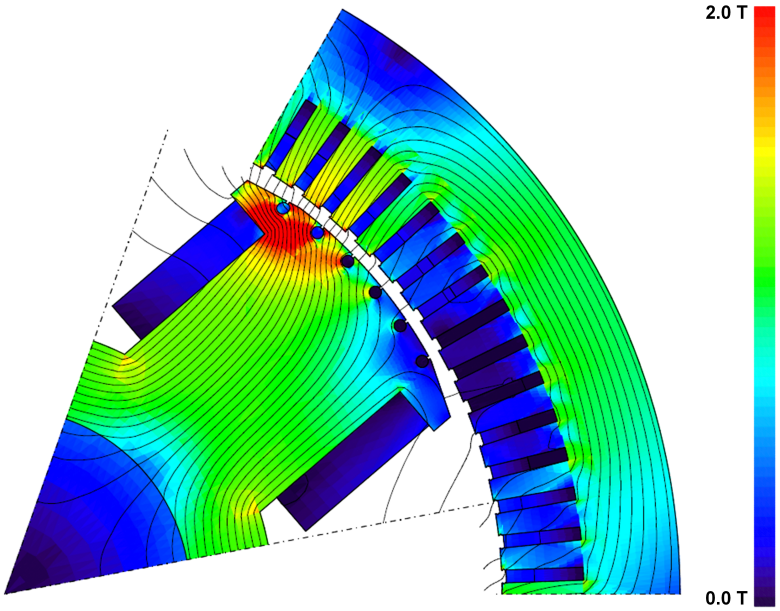


Figure 23: Flux density distribution of the smallest symmetry section in CIMTD.

In the case of SYDC, the process of elements selection in stator yoke at each slot pitch interval is depicted in Figure 24. It can be seen that the number of stator slots and the number of points in flux density waveform is equal, which is depicted in Figure 25.

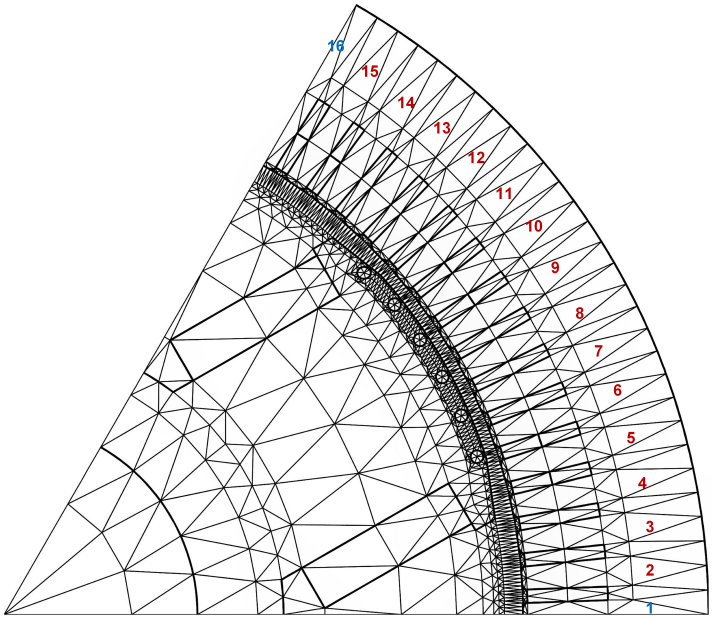


Figure 24: Elements selection for the flux density waveform formation over one pole pitch in SYDC.

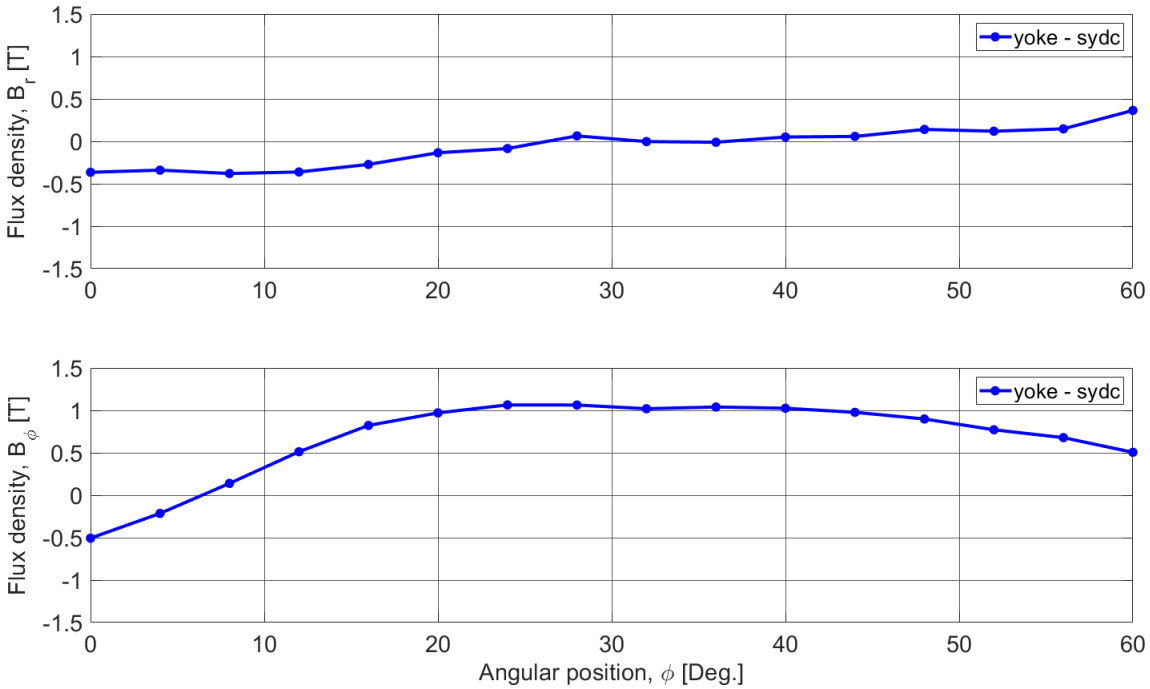


Figure 25: Flux density values at the selected elements in stator yoke in SYDC: (above) radial components; (below) tangential components.

Similarly, the flux density waveform in the stator teeth was formed by choosing

the elements at one slot pitch interval. In such a way, elements to elements flux density waveform can be constructed at each slot pitch interval over two pole pitches to calculate the average iron loss from a closed cycle of the flux density waveforms. It is worth noticing in Figure 24 that the same size of the element in each stator slot pitch meshes from number 2 to 15, i.e., represents full slot pitch was found at a distance of one slot pitch interval. On the other hand, the elements in position 1 and 16 represents half of the slot pitch, and the size of these elements are different compared to other slot pitches mesh. Therefore, the total number of elements in this slot pitch is not equal compared to the other slot pitches mesh. However, the same number of elements in each slot pitch mesh is required when the elements to elements flux density waveform need to be formed in the actual iron loss computation; thus, this slot pitch was avoided. It can be noted that the flux density waveform was formed by specified an observation point at one element, i.e., number 1, and varying by one slot pitch from number 1 to 16 in Figure 25. Such variation over one pole pitch provides the half cycle of the flux density waveform. Therefore, a complete cycle of flux density waveform is obtained in SYDC by varying over two pole pitches, as shown in Figure 28. As one observation point was specified in each element; therefore, no elements were missed, and the flux density points are evenly spaced in Figure 28 even though the elements in number 1 and 16 are different compared to other selected elements in Figure 24. However, the recommended integration points in case of quadratic triangular elements and the corresponding flux density values were considered in actual loss calculation which is described in Section 3.6.

Before computing the flux density values for a complete cycle, the magnetic vector potential $\boldsymbol{A}$ was studied first for both methods as the flux density was calculated from the partial derivative of $\boldsymbol{A}$ which is described in Section 3.7.1. The magnetic vector potential was computed by selecting a particular observation point in the stator yoke and another one in the stator teeth. The selection of these specific points was made by defining their coordinates. The coordinates were defined in $(r, \theta)$ coordinate where $r$ is the radial distance and $\theta$ is the angular distance from the rotor midpoint to the node. The coordinate was transformed to $(x, y)$ coordinate as the FEM gives the output of the magnetic vector potential $\boldsymbol{A}$ in $(x, y)$ coordinate, which is described in Section 3.1.2. An algorithm was developed to search the element in which the defined observation point existed. The specified $(x, y)$ coordinate associated with that point was normalised with the local coordinates $(u, v)$ and the magnetic vector potential of the defined coordinate are computed and transferred to the global coordinate $(x, y)$ by the determinant of the Jacobian matrix. The coordinate transformation using the determinant of the Jacobian matrix is described in Section 3.6.

In SYDC, the coordinate of the observation point was defined one in stator yoke, and another one in stator teeth. It can be noted that the radial distance $r$ remains constant for all the points were taken in stator yoke, and only the angular distance $\theta$ was verified according to half of the slot pitch over one period. Similarly, the radial distance $r$ was the same for stator teeth as well; however, the angular distance $\theta$ was varied one slot pitch in order to avoid the stator slot exist between two successive slot pitches, and the vector potential $\boldsymbol{A}$ of each point was computed over one period. Thus, the magnetic vector potential in the case of stator yoke is contained twice the

number of points than the stator teeth in one period, which can be seen in Figure 26, consequently the flux density waveforms in Figures 28, and 29. It can be noted that the elements in stator yoke were selected at half slot pitch interval for representation purpose. However, the elements in stator yoke were selected at one slot pitch interval in actual iron loss computation.

In the time-stepping simulation, one particular observation point was specified in the stator yoke and another one in the stator teeth by defining their corresponding coordinates $(r, \theta)$. The profile of the magnetic vector potential values $\boldsymbol{A}$ at these observation points were changed at each time step. A complete set of the magnetic vector potential $\boldsymbol{A}$ values were obtained in the stator yoke and teeth for one periodic interval. In the time-stepping method, the vector potential values were appeared corresponding to their time step. Thus, the magnetic vector potential $\boldsymbol{A}$ values are plotted corresponding to their time step in Figure 27. In SYDC, the time variation of the magnetic vector potential $\boldsymbol{A}$ waveform is shown in Figure 27 where each time step was computed according to Equation 63.

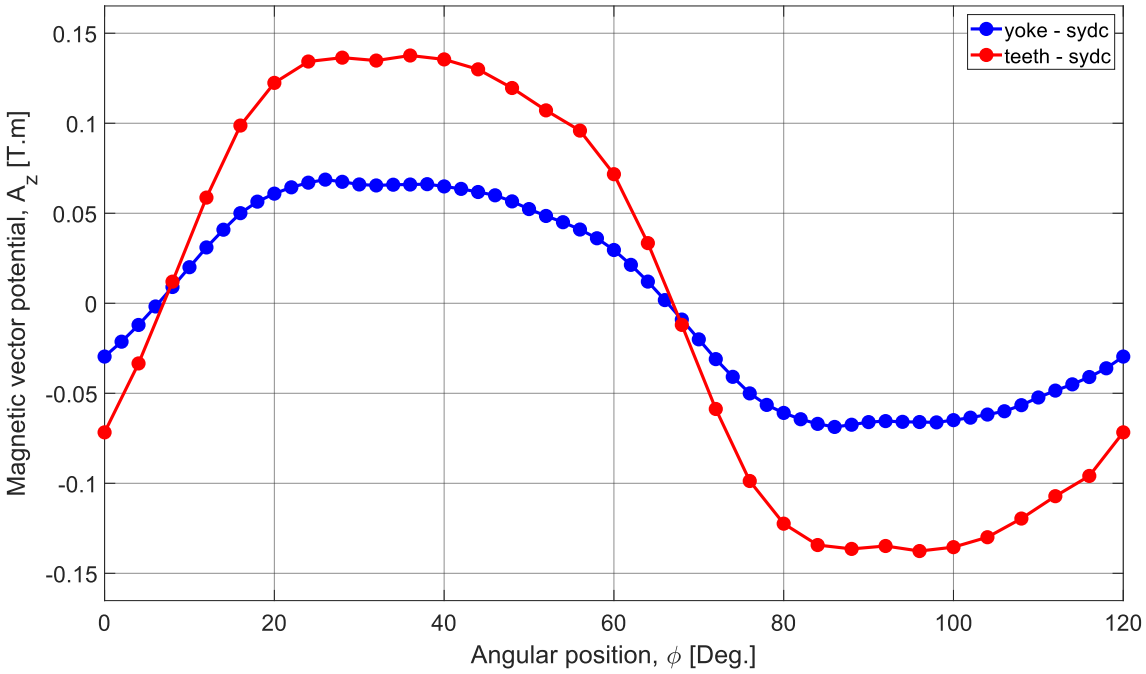


Figure 26: Magnetic vector potential in SYDC.

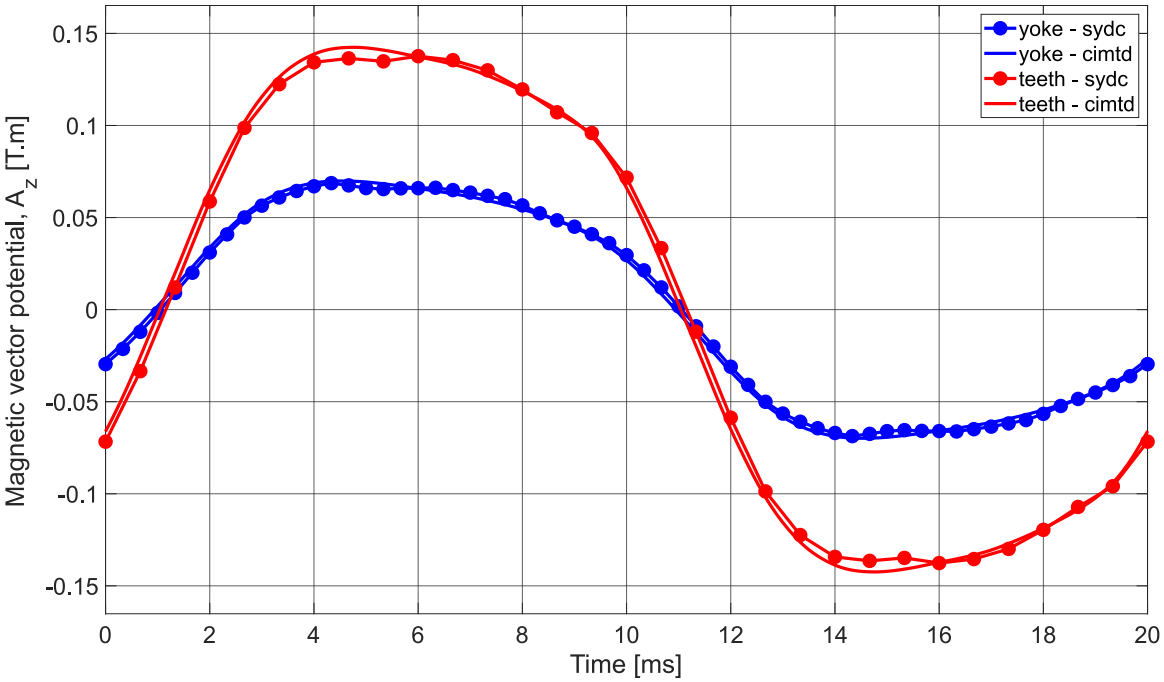


Figure 27: Magnetic vector potential comparison SYDC and CIMTD.

The magnetic vector potential waveform for both methods have a relatively good agreement. Thus, it is expected that the computed flux density values from these magnetic vector potential values should be matched for both methods. However, the magnetic vector potential waveform in case of static simulation looks a little bit more distorted due to the less number of points in the waveform. It can be noticed that the obtained magnetic vector potential waveform is not perfectly sinusoidal due to the effect of the space harmonic components.

In FEM, the flux density $\boldsymbol{B}$ values are computed natively in the $x$-$y$ coordinates; thus, the actual iron loss was calculated from the flux density $B_x$ and $B_y$ values. In practice, the flux density $\boldsymbol{B}$ is solved by assuming the two-dimensional approximation where the flux density lies only in $(x, y)$ plane in Cartesian coordinates or $(r, \phi)$ plane in cylindrical coordinates and does not depend on the $z$-axis. The radial $B_r$ and the tangential $B_\phi$ components of the flux density values in stator yoke and teeth over one period are presented in Figures 28, and 29 for better understanding purpose. The coordinate transformation from the Cartesian coordinates $(x, y)$ to the cylindrical coordinates was done according to Equation 69.

$$\begin{bmatrix} B_\phi \\ B_r \end{bmatrix} = \begin{bmatrix} \cos\phi & -\sin\phi \\ \sin\phi & \cos\phi \end{bmatrix} \begin{bmatrix} B_x \\ B_y \end{bmatrix} \tag{69}$$

In the case of SYDC, the space distribution of the flux density waveform in stator yoke and teeth over one period is illustrated in Figure 28.

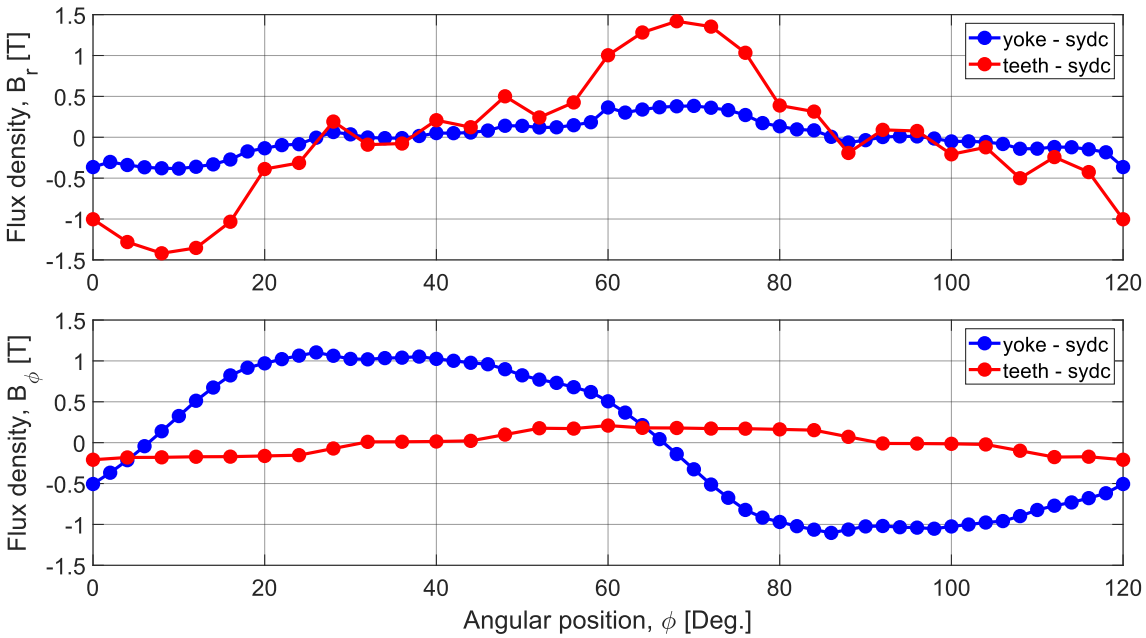


Figure 28: Magnetic flux density in SYDC: (above) radial components; (below) tangential components.

The time variation of the flux density waveforms in static analysis is shown in Figure 29, where each time step was computed according to Equation 63. It can be noted that the obtained flux density waveform in Figure 29 in the time-stepping method is naturally in the time domain.

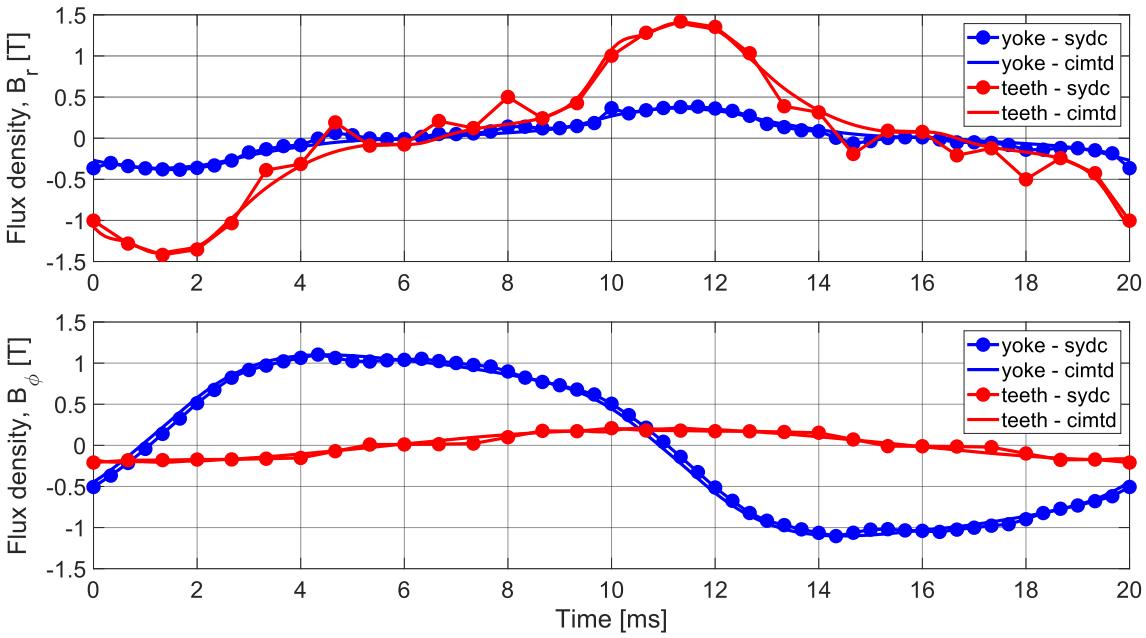


Figure 29: Magnetic flux density comparison SYDC and CIMTD: (above) radial components; (below) tangential components.

It can be seen that the radial components of the flux density $B_r$ are higher in the stator teeth. At the same time, the tangential components $B_\phi$ are more elevated in the stator yoke, which can also be seen from the flux density distribution in Figures 22, and 23. The non-sinusoidal flux density distribution is noticeable due to the spatial harmonic components present in the waveform. However, the flux density waveform in stator teeth is looking more distorted due to the higher harmonic components associated with the teeth area.

The Fourier transformation was performed to analyse the harmonic components presented in the flux density waveform in Figure 29. The Fourier analysis was studied using a MATLAB program. The magnitude of flux density $\boldsymbol{B}$ at each harmonic components was computed, and presented in Figures 30, and 31 from the Fourier components of the radial $B_r$ and tangential $B_\phi$ flux density waveform as

$$\mid B_n \mid = \sqrt{B_{rn}^2 + B_{\phi n}^2} \tag{70}$$

where $n$ is the number of harmonic components. A significant amount of higher harmonic components are appeared in the stator teeth compared to the yoke in both methods. In the case of SYDC, the maximum fifth harmonic components are presented in Figure 30 as the total stator iron loss was computed considering up to $5^{th}$ harmonic components. In the case of CIMTD, the harmonics components are shown up to $25^{th}$ in Figure 31, and all the harmonic components were taken into account for the iron loss calculation.

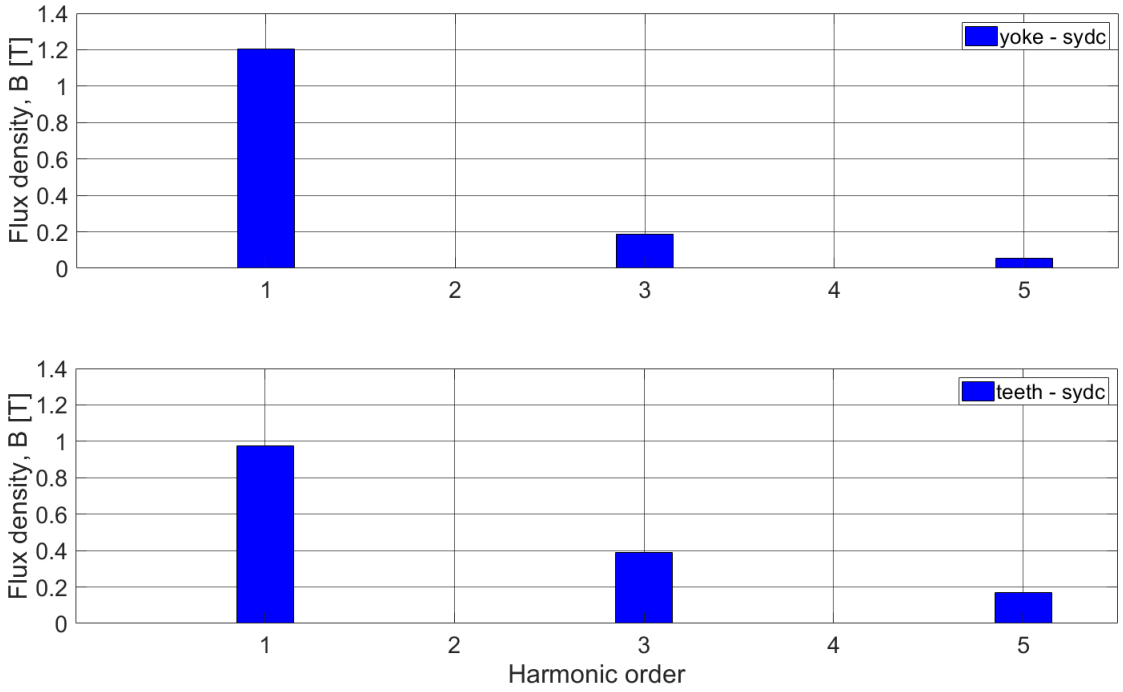


Figure 30: Magnitude of the flux density harmonic components in SYDC.

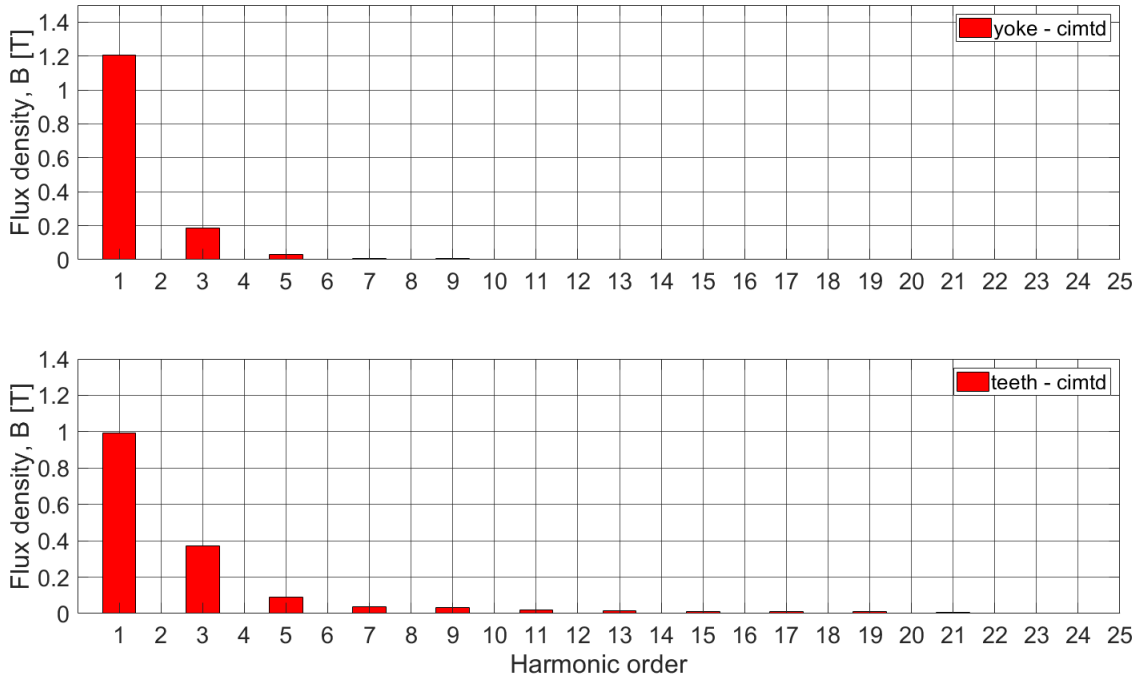


Figure 31: Magnitude of the flux density harmonic components in CIMTD.

It can be seen that the contribution of fundamental harmonic components is more and gradually decreasing with increasing the harmonic orders. It can be noticed that no even harmonic components are presented in both SYDC in Figure 30, and CIMTD in Figure 31 as they cancel out each other because of the symmetrical flux density waveform. In the actual loss computation, the Fourier coefficients were determined from the nodal values and used later to calculate the harmonics of the flux density, which is described in Sections 3.6, and 3.7.1. It can be seen that the flux density per harmonic components has an almost similar magnitude for both methods in Figures 30, and 31. The reason behind this as the flux density waveform in Figure 29 studied for the Fourier analysis through MATLAB program has uniformly spaced samples in case of the SYDC. On the other hand, the flux density waveform was not evenly spaced due to avoid the one slot pitch mesh in the actual loss computation in SYDC. It needs to be clarified that the flux density waveform showed in Figure 29 and also in the actual loss computation, the samples were evenly spaced in case of the CIMTD. It is evident that the Fourier analysis provides a more accurate result for the evenly-spaced samples; thus, the Fourier analysis of the flux density waveform is presented in Figures 30, and 31 has almost similar results in both methods.

Hysteresis and eddy current loss up to fifth harmonic components in SYDC is illustrated in Figure 32 (above), and up to seventh harmonic components in Figure 32 (below). Figure 33 represents the hysteresis and eddy current loss at each harmonic components in CIMTD.

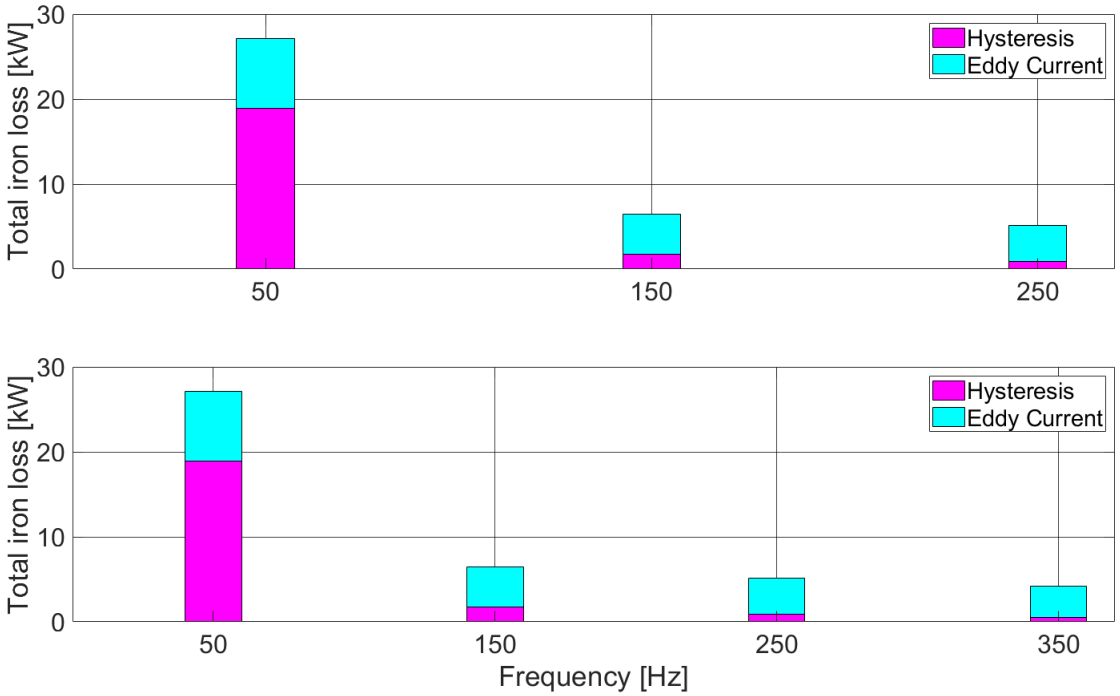


Figure 32: Total stator iron loss per harmonic components in SYDC: (above) up to $5^{th}$ harmonic components; (below) including $7^{th}$ harmonic component.

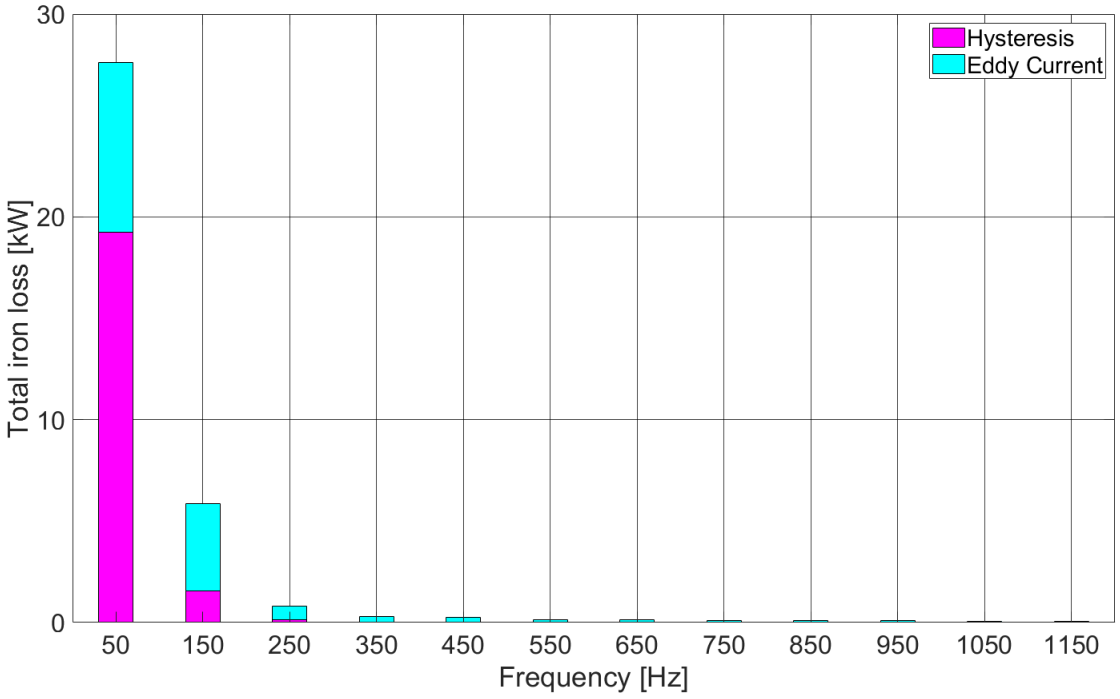


Figure 33: Total stator iron loss per harmonic components in CIMTD.

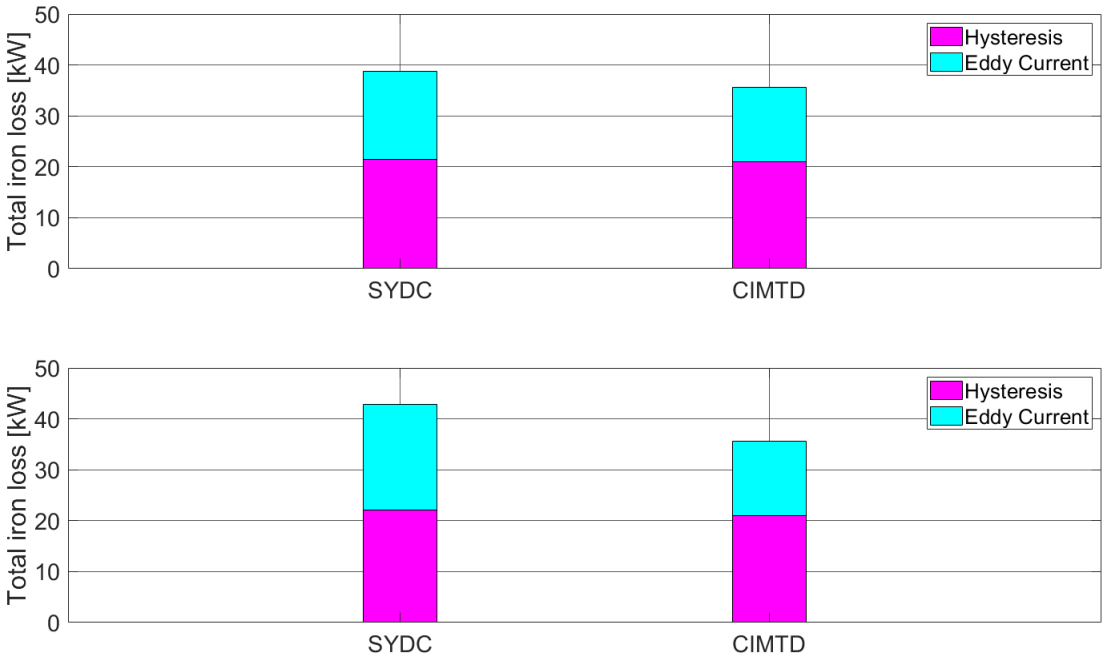


Figure 34: Total stator iron loss comparison SYDC and CIMTD: (above) up to $5^{th}$ harmonics in SYDC; (below) including $7^{th}$ harmonic in SYDC.

In can be seen that the hysteresis loss is dominating in the fundamental frequency harmonic component. However, the eddy current loss becomes more dominating at higher-order harmonic frequency components as the eddy current loss is proportional to the square of the harmonic frequency components. The contribution of hysteresis loss is more in total stator core loss as the eddy current loss is reduced due to the lamination and small thickness of the stator core sheets.

The total stator iron loss as a contribution of hysteresis and eddy current loss is shown in Figure 34. It can be noted that the iron loss is computed in SYDC by taking the lower harmonic components, i.e., up to $5^{th}$ harmonics components as depicted in Figure 34 (above) due to the non uniformly spaced samples. The reason for non-uniform step size and its effect on sampling is described in Section 3.7.1. The proposed method has a relatively good agreement with the existing method. According to Equation 71, the loss difference between these two methods is found 8.94%.

$$\begin{aligned} \text{Total loss difference (\%), D} &= \left| \frac{\text{Loss(SYDC)-Loss(CIMTD)}}{\text{Loss (CIMTD)}} \right| \times 100\% \\ &= 8.94\% \end{aligned} \tag{71}$$

It can be seen that the proposed model is slightly overestimating the losses, especially the losses in the fifth harmonic component compared to the CIMTD. The reason behind the overestimation probably due to the fact that the accuracy of the Fourier

coefficients calculation might drop because of the unevenly spaced samples. Moreover, less number of points were taken into account over one period might degrade the overall Fourier analysis performance as it provides a more accurate result when the number of samples is increased. Furthermore, the trapezoidal method used for numerical approximation might provide some errors such as discretization and truncation, which may also affect the result. The impact of including the $7^{th}$ harmonic components in the loss calculation in SYDC is depicted in Figure 34 (below).

It can be seen that the total stator iron loss is increased significantly after adding the $7^{th}$ harmonic components. According to Equation 71, the total loss difference between the proposed and existing method is reached to 20.73%.

The investigation of including the maximum number of harmonic components in the loss computation was carried out by reconstructing the sampled waveform of a nodal value of the magnetic vector potential **a** as shown in Figure 35. The magnetic

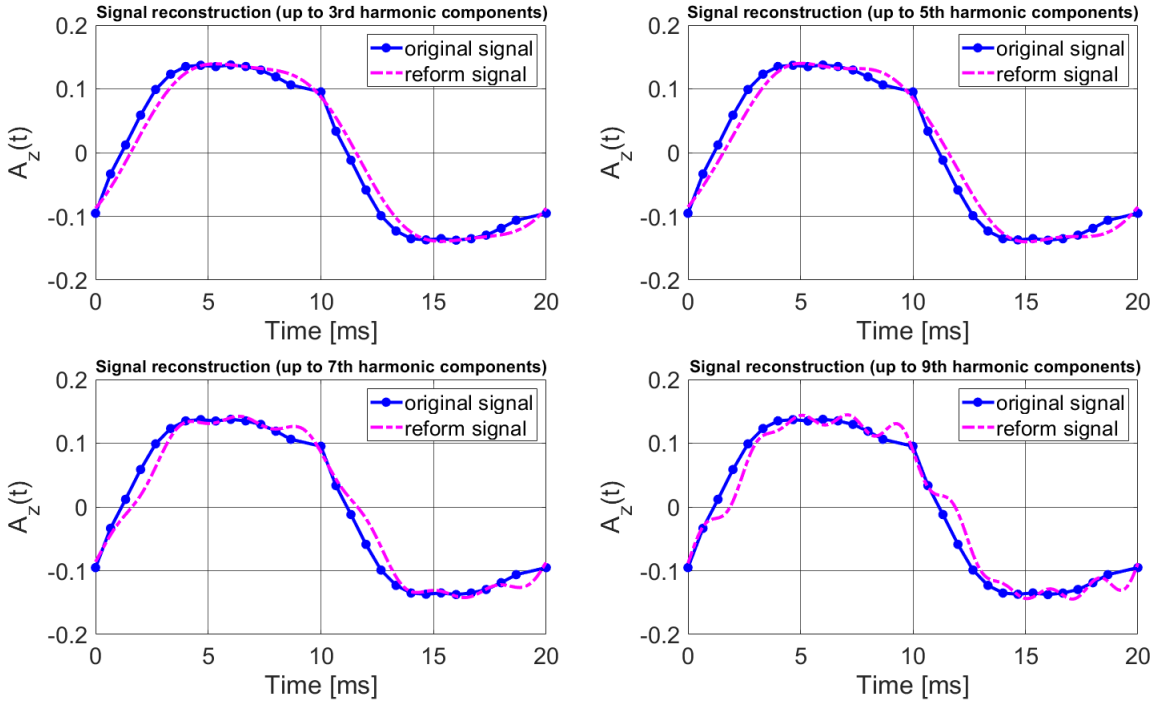


Figure 35: Magnetic vector potential $A_z$ signal reconstruction from Fourier series at different harmonics order.

vector potential waveform was formed by selecting the nodal value at a specific node number in stator tooth and varying by one slot with the node index number over one period. It can be noticed in Figure 35 that, the signal reformation up to $5^{th}$ harmonic components provides relatively good accuracy. However, a significant distortion of the reformed signal is noticeable when the signal is composed of $7^{th}$ or higher harmonic components due to non-uniform step size.

In the transient analysis, the induced current in the damper windings of the separately excited synchronous machine is solved with the field and circuit equations.

One of the applications of damper windings is to improve the flux density waveform by reducing the harmonic components. It can be noted that the damper windings does not have any impact on the static analysis as the induced current in the rotor bars are not taken into account. Thus, the effect of damper windings on flux density harmonic reduction; consequently, the iron loss minimization was studied for time-stepping simulation. The conductivity of the damper windings was set close to zero so that no current can induce in the bars. It was found that the inactivity of the damper windings significantly increases the rotor iron loss, particularly rotor eddy current loss, but there is no such effect noticed in stator iron loss for time-stepping simulation.

The iron loss computation from the static field solution is much faster than the time-stepping simulation. The computation cost of a single static simulation was 332 ms and integrating the iron loss model additionally cost 180 ms; thus, the total computational time was 512 ms. On the other hand, the time-stepping simulation required 35.07 s for the same machine. The computation time was calculated by running the FCSMEK through MATLAB program and using a stopwatch timer function, and the elapsed time was recorded. It can be noted that the computation time for one static stimulation is higher than the expectation which should be equivalent to the one-step simulation, i.e., 116.9 ms of the time-stepping method. The high computation time in case of static simulation due to a large number of iterations are required to convergence as there is no initial solution. On the other hand, a few iterations are needed for time-stepping simulation as each step starts from the solution of the previous one. It can be noted that the time for one iteration is virtually the same with the same number of elements and nodes. The loss calculation program was demanding high computation time as reading the elements and nodes form a separate file requires more time.

# 5 Conclusion

In this thesis, an iron loss computation technique has been developed from a time-efficient static analysis using the Finite Element Method. A computational algorithm was developed in FORTRAN programming language in SYDC routine incorporation with the in-house FEM solver software FCSMEK. A loss calculation comparison was carried out between the developed method and the conventional time-stepping method. The iron loss was computed only in stator core for both methods as the voltage equations, and the field equations are solved assuming the steady-state condition in case of static analysis. The iron loss was calculated from the Fourier decomposition of the magnetic flux density waveform over one period in the post-processing stage. A complete cycle of flux density waveform was formed elements by elements varying by one slot pitch up to one period from a single static simulation. As a result, the flux density waveform should contain an equal number of points as many as the stator slot pitch has over two pole pitches. The time dependence of the nodal values of the magnetic vector potential was introduced to perform the Fourier transformation. The time dependence of nodal values was achieved by using the discretized time step equivalent to the number of stator slot pitch over two pole pitches. The static field solution was obtained by moving the nodes of each slot pitch mesh successively into the initial slot pitch position, i.e., where time is zero at each time step.

The magnetic vector potential was studied in stator yoke and teeth for both methods and found relatively good agreement. The tangential and radial components of the flux density waveform in stator yoke and teeth over one period was computed and found that the flux density waveforms were similar for both cases. The Fourier analysis of the obtained flux density waveform was performed and found that the harmonics in stator teeth were higher compared to the yoke. No even harmonic components were presented in the flux density waveform in both methods because of the symmetrical flux density waveform. The proposed method computes the iron loss with a fair accuracy compared to the time-stepping method. The loss difference between these two methods was observed at 8.94%. It was noticed that the hysteresis loss dominates the eddy current loss at the fundamental frequency component where the eddy current was dominating at higher frequency components. Besides that, the contribution of hysteresis loss was higher in total iron loss computation compared to the eddy current loss for both methods. Due to uneven step size, the inferior rank of the harmonics components, i.e., up to $5^{th}$ harmonic components were taken into account for the loss computation in case of static field solution. The effect of including the $7^{th}$ or higher harmonics components was investigated by reconstructing the magnetic vector potential waveform from the sampled signal. It was noticed that the inclusion of $7^{th}$ or higher harmonics components notably distorted the reformed waveform; thus, the loss computed considering the $5^{th}$ harmonic components should be compared with the loss computation from a dynamic field solution. The inclusion of $7^{th}$ harmonics significantly increases the stator iron loss, and the loss difference reached to 20.73%.

The impact of damper windings on harmonic reduction was studied for time-

stepping simulation. The study showed that the damper windings significantly reduce the rotor eddy current loss, but there is no notable effect on stator iron loss. It can be noted that the same iron loss model was used to compute the iron loss for both methods. The iron loss computation from a static field solution is computationally highly efficient. It can be easily noticeable as the loss computation from a single static stimulation required 512 ms, whereas 35.07 s is needed for the time-stepping simulation.

However, some limitations were faced during the iron loss computation from a static field solution that can be tackled in future. The stator mesh can be reconstructed so that each slot pitch mesh will be identical, which eventually provides the uniform step size among the samples. As a result, no information will be missed from the sampled signal and all the harmonic components can be taken into account for iron loss computation. Besides that, an idea can be developed to reduce the step size less than one slot pitch, so that, the number of points over one interval of the flux density waveform will increase which may improve the accuracy of the Fourier coefficients calculation. It can be done mainly for stator teeth as taking more points for stator yoke was already depicted in this thesis. Furthermore, a more efficient numerical integration method rather than the Trapezoidal method can be used for better numerical approximation. Moreover, the developed iron loss computation method can be applied to other synchronous machines as well.

# References


Agarwal, P. D. (1959). Eddy-current losses in solid and laminated iron. *Transactions of the American institute of electrical engineers, Part I: Communication and Electronics*, *78*(2), 169–181.

Alatawneh, N., & Pillay, P. (2014). The minor hysteresis loop under rotating magnetic fields in machine laminations. *IEEE Transactions on Industry Applications*, *50*(4), 2544–2553.

Albach, M., Durbaum, T., & Brockmeyer, A. (1996). Calculating core losses in transformers for arbitrary magnetizing currents a comparison of different approaches. In *Pesc record. 27th annual ieee power electronics specialists conference* (Vol. 2, pp. 1463–1468).

Al-Din, M., Kader, A., & Al-Samarai, J. (1997). A new method to compute eddy current losses by the finite elements method. In *Ias'97. conference record of the 1997 ieee industry applications conference thirty-second ias annual meeting* (Vol. 1, pp. 3–9).

Ali, K., Atallah, K., & Howe, D. (1997). Prediction of mechanical stress effects on the iron loss in electrical machines. *Journal of applied physics*, *81*(8), 4119–4121.

Andresen, E., & Müller, W. (1983). Berechnung der anlaufdaten von asynchron-käfigläufermotoren verschiedener stabformen mit der methode der finiten differenzen. *Archiv für Elektrotechnik*, *66*(3), 179–185.

Arkkio, A. (1987). *Analysis of induction motors based on the numerical solution of the magnetic field and circuit equations* [PhD thesis]. Helsinki University of Technology, Finland.

Arkkio, A., & Niemenmaa, A. (1992). Estimation of losses in cage induction motors using finite element techniques. In *Ieee international conference of electrical machines* (pp. 317–321).

Arkkio, A., & Sundaria, R. (2018). *Numerical methods in electromechanics.* (lecture slide)

Aston, K., & Rao, M. K. (1941). Pole-face losses due to open slots. *Journal of the Institution of Electrical Engineers-Part II: Power Engineering*, *88*(3), 223–240.

Atallah, K., & Howe, D. (1993). Calculation of the rotational power loss in electrical steel laminations from measured h and b. *IEEE Transactions on Magnetics*, *29*(6), 3547–3549.

Baily, F. G. (1896). Xviii. the hysteresis of iron and steel in a rotating magnetic field. *Philosophical Transactions of the Royal Society of London. Series A, Containing Papers of a Mathematical or Physical Character*(187), 715–746.

Bastos, J. P. A., & Sadowski, N. (2003). *Electromagnetic modeling by finite element methods*. CRC press.

Belahcen, A., & Arkkio, A. (2008). Comprehensive dynamic loss model of electrical steel applied to fe simulation of electrical machines. *IEEE Transactions on Magnetics*, *44*(6), 886–889.

Belahcen, A., Mukherjee, V., Far, M. F., Rasilo, P., & Hinkkanen, M. (2016).

Coupled field and space-vector equations of bearingless synchronous reluctance machine. In *2016 xxii international conference on electrical machines (icem)* (pp. 2581–2587).

Belahcen, A., Rasilo, P., & Arkkio, A. (2014). Segregation of iron losses from rotational field measurements and application to electrical machine. *IEEE Transactions on magnetics*, *50*(2), 893–896.

Belkasim, M. A. (2008). *Identification of loss models from measurements of the magnetic properties of electrical steel sheets* (Master's thesis). Helsinki University of Technology, Finland.

Bergqvist, A. (1996). A simple vector generalization of the jiles-atherton model of hysteresis. *IEEE Transactions on Magnetics*, *32*(5), 4213–4215.

Bernard, Y., Mendes, E., & Bouillault, F. (2002). Dynamic hysteresis modeling based on preisach model. *IEEE Transactions on Magnetics*, *38*(2), 885–888.

Bertotti, G. (1985). Physical interpretation of eddy current losses in ferromagnetic materials. i. theoretical considerations. *Journal of applied Physics*, *57*(6), 2110–2117.

Bertotti, G. (1988). General properties of power losses in soft ferromagnetic materials. *IEEE Transactions on magnetics*, *24*(1), 621–630.

Bertotti, G. (1992). Dynamic generalization of the scalar preisach model of hysteresis. *IEEE Transactions on Magnetics*, *28*(5), 2599–2601.

Bertotti, G. (1998). *Hysteresis in magnetism: for physicists, materials scientists, and engineers*. Academic press.

Bertotti, G., Fiorillo, F., & Soardo, G. (1988). The prediction of power losses in soft magnetic materials. *Le Journal de Physique Colloques*, *49*(C8), C8–1915.

Bikram Shah, S. (2013). *Finite element modeling of losses due to inter-laminar short-circuit currents in electrical machines* (Master's thesis). Aalto University, Finland.

Boon, C., & Robey, J. (1968). Effect of domain-wall motion on power loss in grain-oriented silicon-iron sheet. In *Proceedings of the institution of electrical engineers* (Vol. 115, pp. 1535–1540).

Bottauscio, O., Chiampi, M., & Chiarabaglio, D. (2000a). Advanced model of laminated magnetic cores for two-dimensional field analysis. *IEEE Transactions on Magnetics*, *36*(3), 561–573.

Bottauscio, O., Chiampi, M., & Chiarabaglio, D. (2000b). Magnetic flux distribution and losses in narrow ferromagnetic strips. *Journal of magnetism and magnetic materials*, *215*, 46–48.

Bouillault, F., & Razek, A. (1983). Numerical calculation of eddy currents in mobil electromagnetic systems. *Proc. UPEC, Guildford*.

Brailsford, F. (1948). Investigation of the eddy-current anomaly in electrical sheet steels. *Journal of the Institution of Electrical Engineers-Part II: Power Engineering*, *95*(43), 38–48.

Brainard, F. (1913). Notes on stray losses in synchronous machines. *Proceedings of the American Institute of Electrical Engineers*, *32*(2), 548–551.

Brandl, P., et al. (1975). Simulation du turbo-alternateur en regime de charge stationnaire.

Brown, C. (1891). Reasons for the use of three-phase current in the lauffen-frankfurt transmission. *Electrical world*, 346.

Chen, P., Wang, A., Zhao, C., He, A., Wang, G., Chang, C., ... Liu, C.-T. (2017). Development of soft magnetic amorphous alloys with distinctly high fe content. *SCIENCE CHINA Physics, Mechanics & Astronomy*, *60*(10), 106111.

Chwastek, K., Szczyglowski, J., & Najgebauer, M. (2006). A direct search algorithm for estimation of jiles–atherton hysteresis model parameters. *Materials Science and Engineering: B*, *131*(1-3), 22–26.

Clough, R. W. (1960). The finite element method in plane stress analysis. In *Proceedings of 2nd asce conference on electronic computation, pittsburgh pa., sept. 8 and 9, 1960.*

Demerdash, N., & Gillott, D. (1974). A new approach for determination of eddy current and flux penetration in nonlinear ferromagnetic materials. *IEEE Transactions on Magnetics*, *10*(3), 682–685.

Deng, E., & Demerdash, N. (1996). A coupled finite-element state-space approach for synchronous generators. i. model development. *IEEE Transactions on Aerospace and electronic systems*, *32*(2), 775–784.

Deng, F., & Demerdash, N. A. (1998). Comprehensive salient-pole synchronous machine parametric design analysis using time-step finite element-state space modeling techniques. *IEEE transactions on energy conversion*, *13*(3), 221–229.

Dlala, E., Belahcen, A., & Arkkio, A. (2008). Efficient magnetodynamic lamination model for two-dimensional field simulation of rotating electrical machines. *Journal of Magnetism and Magnetic Materials*, *320*(20), e1006–e1010.

Dlala, E., Belahcen, A., & Arkkio, A. (2010). On the importance of incorporating iron losses in the magnetic field solution of electrical machines. *IEEE Transactions on Magnetics*, *46*(8), 3101–3104.

Dlala, E., Belahcen, A., Pippuri, J., & Arkkio, A. (2010). Interdependence of hysteresis and eddy-current losses in laminated magnetic cores of electrical machines. *IEEE Transactions on Magnetics*, *46*(2), 306–309.

Dlala, E. A. (2008). *Magnetodynamic vector hysteresis models for steel laminations of rotating electrical machines* [PhD thesis]. Helsinki University of Technology, Finland.

Dular, P., Gyselinck, J., Henrotte, F., Legros, W., & Melkebeek, J. (1998). Modeling of eddy currents in steel laminations using complementary 3d finite element formulations with enforced magnetic fluxes. In *Proceedings of the 4th international workshop on electric and magnetic fields* (pp. 177–182).

Dupré, L., & Melkebeek, J. (2003). Electromagnetic hysteresis modelling: from material science to finite element analysis of devices. *International Compumag Society Newsletter*, *10*(3), 4–15.

Dupré, L. R., Gyselinck, J. J., & Melkebeek, J. A. (1998). Complementary finite element methods in 2d magnetics taking into account a vector preisach model. *IEEE transactions on magnetics*, *34*(5), 3048–3051.

Enokizono, M., & Sievert, J. (1989). Magnetic field and loss analysis in an apparatus for the determination of rotational loss. *Physica Scripta*, *39*(3), 356.

Enokizono, M., Suzuki, T., & Sievert, J. (1991). Measurement of iron loss using

rotational magnetic loss measurement apparatus. *IEEE translation journal on magnetics in Japan*, *6*(6), 508–514.

Everett, D. H. (1955). A general approach to hysteresis. part 4. an alternative formulation of the domain model. *Transactions of the Faraday Society*, *51*, 1551–1557.

Faiz, J., & Sharifian, M. (1994). Core losses estimation in a multiple teeth per stator pole switched reluctance motor. *IEEE Transactions on Magnetics*, *30*(2), 189–195.

Farzam Far, M. (2019). *Model order reduction for simulation and control of synchronous machines* [PhD thesis]. Aalto University, Finland.

Fiorillo, F., & Novikov, A. (1990). An improved approach to power losses in magnetic laminations under nonsinusoidal induction waveform. *IEEE Transactions on Magnetics*, *26*(5), 2904–2910.

Fiorillo, F., & Rietto, A. (1993). Rotational versus alternating hysteresis losses in nonoriented soft magnetic laminations. *Journal of applied physics*, *73*(10), 6615–6617.

Fouad, F. A., Nehl, T., & Demerdash, N. (1981). Magnetic field modeling of permanent magnet type electronically operated synchronous machines using finite elements. *IEEE Transactions on Power Apparatus and Systems*(9), 4125–4135.

Gray, A. (1926). *Electrical machine design*. McGraw-Hill Book.

Guo, Y., Zhu, J. G., Zhong, J., Lu, H., & Jin, J. X. (2008). Measurement and modeling of rotational core losses of soft magnetic materials used in electrical machines: A review. *IEEE Transactions on Magnetics*, *44*(2), 279–291.

Gyselinck, J., Vandevelde, L., Melkebeek, J., Dular, P., Henrotte, F., & Legros, W. (1999). Calculation of eddy currents and associated losses in electrical steel laminations. *IEEE Transactions on Magnetics*, *35*(3), 1191–1194.

Hafner, M., Franck, D., & Hameyer, K. (2010). Static electromagnetic field computation by conformal mapping in permanent magnet synchronous machines. *IEEE Transactions on Magnetics*, *46*(8), 3105–3108.

Handgruber, P., Stermecki, A., Biro, O., Belahcen, A., & Dlala, E. (2012). 3-d eddy current analysis in steel laminations of electrical machines as a contribution for improved iron loss modeling. In *2012 xxth international conference on electrical machines* (pp. 16–22).

Harnefors, L., Hinkkanen, M., Wallmark, O., & Yepes, A. (2015). *Control of voltage-source converters and variable-speed drives, ser.* manuscript.

Hu, J., Luo, Y., Liu, M., & Liu, X. (2008). Analysis of the iron loss of line start permanent magnet synchronous motor using time-stepping finite element method. In *2008 international conference on electrical machines and systems* (pp. 3237–3240).

Hubert, A., & Schäfer, R. (2008). *Magnetic domains: the analysis of magnetic microstructures*. Springer Science & Business Media.

Hudak, P., Hrabovcova, V., Rafajdus, P., & Mihok, J. (2004). Core loss analysis of the reluctance synchronous motor with barrier rotors. *Journal of Electrical Engineering*, *55*(9-10), 273–276.

Hughes, A. (2006). *Electric motors and drives: fundamentals, types and applications* (Third ed.). Newnes, Elsevier.

Islam, M. J. (2010). *Finite-element analysis of eddy currents in the form-wound multi-conductor windings of electrical machines* [PhD thesis]. Aalto University, Finland.

Jiles, D. (1993). Frequency dependence of hysteresis curves in'non-conducting'magnetic materials. *IEEE Transactions on Magnetics*, *29*(6), 3490–3492.

Jiles, D. (2015). *Introduction to magnetism and magnetic materials*. CRC press.

Jiles, D., & Atherton, D. (1983). Ferromagnetic hysteresis. *IEEE Transactions on Magnetics*, *19*(5), 2183–2185.

Jiles, D. C. (1994). Modelling the effects of eddy current losses on frequency dependent hysteresis in electrically conducting media. *IEEE transactions on Magnetics*, *30*(6), 4326–4328.

Jiles, D. C., & Atherton, D. L. (1984). Theory of ferromagnetic hysteresis. *Journal of applied physics*, *55*(6), 2115–2120.

Jordan, H. (1924). Die ferromagnetischen konstanten für schwache wechselfelder. *Elektr. Nach. Techn*, *1*(8).

Kampen, D., Owzareck, M., Beyer, S., Parspour, N., & Schmitt, S. (2012). Analytical core loss models for electrical steel in power electronic applications. In *2012 13th international conference on optimization of electrical and electronic equipment (optim)* (pp. 109–117).

Karmaker, H. (1992). Stray losses in large synchronous machines. *IEEE transactions on energy conversion*, *7*(1), 148–153.

Knight, A. M., Troitskaia, S., Stranges, N., & Merkhouf, A. (2009). Analysis of large synchronous machines with axial skew, part 1: flux density and open-circuit voltage harmonics. *IET electric power applications*, *3*(5), 389–397.

Kochmann, T. (1996). Relationship between rotational and alternating losses in electrical steel sheets. *Journal of magnetism and magnetic materials*, *160*, 145–146.

Krasnosel'skii, M. A., & Pokrovskii, A. V. (2012). *Systems with hysteresis*. Springer Science & Business Media.

Krings, A. (2014). *Iron losses in electrical machines-influence of material properties, manufacturing processes, and inverter operation* (Unpublished doctoral dissertation). KTH Royal Institute of Technology.

Krings, A., & Soulard, J. (2010). Overview and comparison of iron loss models for electrical machines. *Journal of Electrical Engineering*, *10*(3), 162–169.

Labridis, D., & Dokopoulos, P. (1989). Calculation of eddy current losses in nonlinear ferromagnetic materials. *IEEE Transactions on Magnetics*, *25*(3), 2665–2669.

Leissa, A. W. (2005). The historical bases of the rayleigh and ritz methods. *Journal of Sound and Vibration*, *287*(4-5), 961–978.

Leonardi, F., Matsuo, T., & Lipo, T. (1996). Iron loss calculation for synchronous reluctance machines. In *Proceedings of international conference on power electronics, drives and energy systems for industrial growth* (Vol. 1, pp. 307–

312).

Luomi, J. (1993). Finite element methods for electrical machines. *Goteborg: Chalmers University of Technology, Department of Electrical Machine and Power electronics*.

Matlab. (2006). *Trapizoidal method.* Retrieved from https://se.mathworks.com/help/matlab/ref/trapz.html#bua4lsr

Matsuo, T., & Lipo, T. A. (1994). Rotor design optimization of synchronous reluctance machine. *IEEE Transactions on Energy Conversion*, *9*(2), 359–365.

Mayergoyz, I. (1986). Mathematical models of hysteresis. *IEEE Transactions on magnetics*, *22*(5), 603–608.

Mayergoyz, I., & Serpico, C. (1999). Nonlinear diffusion of electromagnetic fields and excess eddy current losses. *Journal of applied physics*, *85*(8), 4910–4912.

Moses, A. (1992). Importance of rotational losses in rotating machines and transformers. *Journal of Materials Engineering and Performance*, *1*(2), 235–244.

Moses, A., & Shirkoohi, G. (1985). Measurement of power loss in nonorientated electrical steels under distorted flux conditions. In *Proceedings of smm7 conference.*

Nakata, T., Ishihara, Y., & Nakano, M. (1970). Iron losses of silicon steel core produced by distorted flux. *Electrical Engineering in Japan*, *90*(1-2), 10.

Neidhofer, G. (1992). The evolution of the synchronous machine. *Engineering Science and Education Journal*, *1*(5), 239–248.

Overshott, K., Preece, I., & Thompson, J. (1968). Magnetic properties of grain-oriented silicon iron. part 2: Basic experiments on the nature of the anomalous loss using an individual grain. In *Proceedings of the institution of electrical engineers* (Vol. 115, pp. 1840–1845).

Pippuri, J. (2010). *Finite element analysis of eddy current losses in steel laminations of inverter-fed electrical machines* [PhD thesis]. Aalto University, Finland.

Pippuri, J., Belahcen, A., Dlala, E., & Arkkio, A. (2010). Inclusion of eddy currents in laminations in two-dimensional finite element analysis. *IEEE Transactions on Magnetics*, *46*(8), 2915–2918.

Preisach, F. (1935). Über die magnetische nachwirkung. *Zeitschrift für physik*, *94*(5-6), 277–302.

Pry, R., & Bean, C. (1958). Calculation of the energy loss in magnetic sheet materials using a domain model. *Journal of Applied Physics*, *29*(3), 532–533.

Pyrhonen, J., Jokinen, T., & Hrabovcova, V. (2013). *Design of rotating electrical machines.* John Wiley & Sons.

Rajamäki, J. (2019). *Analysis of loss components in a synchronous generator under non-ideal operating conditions* (Master's thesis). Aalto University, Finland.

Rasilo, P. (2012). *Finite-element modeling and calorimetric measurement of core losses in frequency-converter-supplied synchronous machines* [PhD thesis]. Aalto University, Finland.

Richardson, P. (1945). Stray losses in synchronous electrical machinery. *Journal of the Institution of Electrical Engineers-Part II: Power Engineering*, *92*(28),

291–301.

Rupanagunta, P., Hsu, J. S., & Weldon, W. F. (1991). Determination of iron core losses under influence of third-harmonic flux component. *IEEE Transactions on Magnetics*, *27*(2), 768–777.

Saari, J. (1998). *Thermal analysis of high-speed induction machines* [PhD thesis]. Helsinki University of Technology, Finland.

Sadarangani, C. (2006). *Electrical machines: Design and analysis of induction and permanent magnet motors*. Division of Electrical Machines and Power Electronics, School of Electrical ....

Saitz, J. (2001). Magnetic field analysis of induction motors combining preisach hysteresis modeling and finite element techniques. *IEEE transactions on magnetics*, *37*(5), 3693–3697.

Schifer, R., & Lipo, T. (1989). Core loss in buried magnet permanent magnet synchronous motors. *IEEE Transactions on Energy Conversion*, *4*(2), 279–284.

Schuisky, W. (1960). *Design of electrical machines (berechnung elektrischer maschinen)*. springer.

Sen, P. C. (2007). *Principles of electric machines and power electronics*. John Wiley & Sons.

Serpico, C., Visone, C., Mayergoyz, I., Basso, V., & Miano, G. (2000). Eddy current losses in ferromagnetic laminations. *Journal of Applied Physics*, *87*(9), 6923–6925.

Shilling, J., & Houze, G. (1974). Magnetic properties and domain structure in grain-oriented 3% si-fe. *IEEE Transactions on Magnetics*, *10*(2), 195–223.

Sievert, J., Ahlers, H., Birkfeld, M., Cornut, B., Fiorillo, F., Hempel, K., ... others (1996). European intercomparison of measurements of rotational power loss in electrical sheet steel. *Journal of Magnetism and Magnetic Materials*, *160*, 115–118.

Silvester, P. (1969). High-order polynomial triangular finite elements for potential problems. *International Journal of Engineering Science*, *7*(8), 849–861.

SKF. (1994). *General catalogue* (Catalogue 4000/IV E ed.).

Soroush, H., Rahmati, A., Moghbelli, H., Vahedi, A., & Niasar, A. H. (2009). Study on the hunting in high speed hysteresis motors due to the rotor hysteresis material. In *Ieee eurocon 2009* (pp. 677–681).

Soualmi, A., Dubas, F., Depernet, D., Randria, A., & Espanet, C. (2012). Study of copper losses in the stator windings and pm eddy-current losses for pm synchronous machines taking into account influence of pwm harmonics. In *2012 15th international conference on electrical machines and systems (icems)* (pp. 1–5).

Steinmetz, C. P. (1892). On the law of hysteresis. *Transactions of the American Institute of Electrical Engineers*, *9*(1), 1–64.

Sun, J., Haller, T., & Kramer, J. (1971). Observations of magnetic losses in a single crystal of a ferromagnetic conductor. *Journal of Applied Physics*, *42*(4), 1789–1791.

Sun, J., & Kramer, J. (1977). A microscopic analysis of eddy current losses in

ferromagnetic conductors. *IEEE Transactions on Magnetics*, *13*(5), 1524–1526.

Takahashi, N., Miyabara, S.-H., & Fujiwara, K. (1999). Problems in practical finite element analysis using preisach hysteresis model. *IEEE transactions on magnetics*, *35*(3), 1243–1246.

Vrancik, J. E. (1968). Prediction of windage power loss in alternators. *Nasa technical note*.

Williams, H., Shockley, W., & Kittel, C. (1950). Studies of the propagation velocity of a ferromagnetic domain boundary. *Physical Review*, *80*(6), 1090.

Winchester, R. (1955). Stray losses in the armature end iron of large turbine generators [includes discussion]. *Transactions of the American Institute of Electrical Engineers. Part III: Power Apparatus and Systems*, *74*(3), 381–391.

Winslow, A. M. (1964). *Numerical calculation of static magnetic fields in an irregular triangle mesh* (Tech. Rep.). California. Univ., Livermore. Lawrence Radiation Lab.

Yamazaki, K. (2003). Torque and efficiency calculation of an interior permanent magnet motor considering harmonic iron losses of both the stator and rotor. *IEEE Transactions on Magnetics*, *39*(3), 1460–1463.

Yamazaki, K., & Fukushima, N. (2010). Iron-loss modeling for rotating machines: Comparison between bertotti's three-term expression and 3-d eddy-current analysis. *IEEE Transactions on Magnetics*, *46*(8), 3121–3124.

Yamazaki, K., & Watari, S. (2004). Comparison of methods to calculate iron losses caused by harmonic fields in rotating machines. In *Progress in electromagnetic research symposium* (pp. 329–332).

Zhu, J. G., & Ramsden, V. S. (1998). Improved formulations for rotational core losses in rotating electrical machines. *IEEE Transactions on Magnetics*, *34*(4), 2234–2242.

*Trapezoidal Rule*

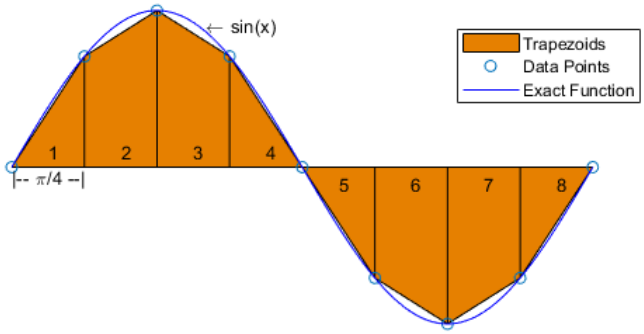


Figure 36: Trapezoidal integration for an evenly spaced sine function (Matlab, 2006).

*Gaussian Quadrature Rule*

Table 8: Integration formulas for triangular elements.

| $n$ | $m$ | $\zeta_i$ | $w_i$ |
|---|---|---|---|
| 1 | 1 | $\frac{1}{3}, \frac{1}{3}, \frac{1}{3}$ | 1 |
| 3 | 2 | $\frac{1}{2}, \frac{1}{2}, 0$ | $\frac{1}{3}$ |
| | | $0, \frac{1}{2}, \frac{1}{2}$ | $\frac{1}{3}$ |
| | | $\frac{1}{2}, 0, \frac{1}{2}$ | $\frac{1}{3}$ |
| 4 | 3 | $\frac{1}{3}, \frac{1}{3}, \frac{1}{3}$ | $-\frac{27}{48}$ |
| | | 0.6,0.2,0.2 | $\frac{25}{48}$ |
| | | 0.2,0.6,0.2 | $\frac{25}{48}$ |
| | | 0.2,0.2,0.6 | $\frac{25}{48}$ |

$n$= Integration points
$m$=Integration order
$\zeta_i$=Area coordinates of integration points in natural coordinate system
$w_i$=Integration weight factors